Anomalous Transport Behavior in the Vicinity of a Topological Phase Transition in $ZrTe_5$

Joshua Mutch

A dissertation

submitted in partial fulfillment of the

requirements for the degree of

Doctor of Philosophy

University of Washington

2021

Reading Committee:

Jiun-Haw Chu, Chair

Xiaodong Xu

David Cobden

Anton Andreev

Program Authorized to Offer Degree:

Department of Physics

University of Washington

Abstract

Anomalous Transport Behavior in the Vicinity of a Topological Phase Transition in $ZrTe_5$

Joshua Mutch

Chair of the Supervisory Committee:
Jiun-Haw Chu
Department of Physics

Understanding the impact of topology on electrical transport properties is currently an area of intense research, motivated by the potential application of engineering materials with physical properties that are protected by the underlying topology. Often, it is difficult to distinguish the root mechanism for measured transport phenomenon. To inspect if topology is responsible for measured phenomena, it is desirable to have a tuning parameter to switch on and off the topological nature of the material. Typically, this is done by chemical doping or thermal lattice expansion. However, chemical doping requires intensive work and can additionally change other factors of the material beyond the topology, and thermal lattice expansion prohibits studying both topological phases at low temperatures.

In this work, I show that in-situ strain can be used to control the topological phase of $ZrTe_5$. This strain can be easily controlled at temperatures ranging from 2K to room temperature and in magnetic fields, providing an ideal tuning parameter. Additionally, I uncover anomalous transport behavior such as an anomalous Hall effect and the magic angle effect in ultra-pure, high mobility $ZrTe_5$ crystals. Such unique behavior originates in $ZrTe_5$ due to its simplistic band structure, where electronic transport is dominated by highly mobile, topologically nontrivial bands at the Γ point. Because of this simplistic band structure and easily accessible tuning parameter, this work establishes ZrTe5 as a paradigm for further electronic transport studies, where strain can be used as a tool to further understand the importance of topology as it relates to these anomalous behaviors.

TABLE OF CONTENTS

LIST OF FIGURES

LIST OF TABLES

ACKNOWLEDGEMENTS

My six years at the University of Washington have been a great positive experience, and I am indebted to many people for making that happen. First, I am thankful for my advisor, Jiun-Haw, for making this all possible. Your passion, excitement, and intuition for science are inspiring. After five years of being in your group I can say that interactions with you always left me encouraged and excited for research; never did I feel put down or discouraged. Your style of leading by pushing curiosity and encouraging exploration has led me to complete several projects, and at every step I felt excited for the next discovery. I'd also like to thank my committee members, Anton, Stephen, David, Jihui, and Xiaodong.

My group members also deserve a sincere thanks. Joshua ("Shua") Sanchez I owe thanks for convincing me to join Jiun-Haw's group. The early days of setting up the lab were especially fun, when every day felt like Christmas opening new equipment inside an empty lab. Your charisma made the windowless basement much more fun. Paul Malinowski and Qianni Jiang were also a joy to have join the lab, I appreciate both of your passion for condensed matter physics and the camaraderie over the years. As the lab grew bigger with the additions of Zhong, Yue, Zhaoyu Elliot, and Xuetao, I can say that there is not a single person who I did not enjoy working with. There is also a long list of undergraduates I should thank – Tianyi, Preston, Tiema, Ryan, Winnie, Dan, Ilham, Aaron, Anna, Sanae, and Joss are some of the ones I worked with directly on projects. Their intelligent questions made me realize the many gaps of knowledge I had that I needed to fill.

Outside of the immediate research group, I have many friends within the program to thank for making my time in Seattle so enjoyable. My first-year office mates Jenni and Eris made surviving the first year possible, and I appreciate their lasting friendship and the tradition of breakfast burritos we intermittently kept out. I also appreciate Maria and Isaac for their lasting friendship over the years. Dianqi and Kevin, thanks for the good times we had on the basketball court, attempting to keep some semblance of exercise alive during graduate school. Shervin, Elliot, and Andy, I enjoyed the time we spent resurrecting the Career Development Organization for two years, if only to watch it crumble during Covid-19. (At least we got to see some really great careers come as a result – if they ever read this, they will get that joke). My roommates and colleagues Jake Busche and Raphael Cervantes I especially appreciate the adventures we've had over the years and the commiseration of surviving the first year of graduate school together.

Finally, I’d like to thank my wife, Lillian, for her support over the years. Marrying you has forever changed my life for the better. You uprooted your life to follow me to Seattle, and for that I’m extremely grateful. You’ve encouraged and supported my every life decision and have filled my life with joy. I’m constantly amazed at how lucky I am to have you in my life – your genuine sincerity and love for everyone inspires me to be a more caring and sincere person.

DEDICATION

To my wife, parents, and sisters.

CHAPTER 1 - INTRODUCTION

MOTIVATION

Before 1982, phase transitions in condensed matter systems were categorized by their symmetry breaking (*1*). However, another type of phase transition has been shown to exist that breaks no obvious symmetries, but rather something called a topological invariant changes from one phase to the next. This idea of a topological phase transition was refined by Thouless and Haldane in the early 1980s to show how states of matter can be defined by their topological invariant, and in 1982 it was shown that the quantum Hall state is a topological state of matter (*2*).

The dependence on material properties to the topology of the material band structure is a relatively young field that has attracted much recent attention, culminating in the 2016 Nobel Prize in physics. Beyond the scientific motivation of studying topology for the sake of understanding how things work, there is perhaps potential for applications using topological materials. When properties of a material are topologically protected, they are robust and cannot easily be destroyed by introducing impurity defects. This guaranteed existence of certain material properties makes topological materials desirable from an engineering perspective. An example of a potential application would be a topological transistor, where topologically protected surface states can be turned off and on by controlling the topological phase of the system (*3*).

BERRY CURVATURE

Berry's phase and Berry's curvature are important quantities when considering the topology of materials. The important consideration is that Berry's phase is *geometric*. That is, the Berry phase depends solely on the path a particle takes through parameter space without any dependence on the speed taken along the path. This reliance on geometry alone enables topological effects to become prominent.

To review the basic concepts of Berry's phase, we consider a system in the n^{th} eigenstate that depends on a set of time-evolving parameters $\boldsymbol{R}$. The state at time t can be written as

$$|\Psi(\mathrm{t})\rangle = e^{i\gamma_n(t)} \exp\left(-\frac{i}{\hbar}\int_0^t dt'\epsilon_n(R(t')\right)\ |n\big(R(t)\big)\rangle.$$

The second time-dependent phase factor is the dynamical phase of the system. Inserting this wavefunction into the time-dependent Schrodinger equation yields the following value for the Berry phase γ_n:

$$\gamma_n = \int_C d\vec{R} \cdot A_n(\vec{R}),$$

where $A_n(\vec{R})$ is known as the Berry connection, and given by

$$A_n(\vec{R}) = i\langle n(\vec{R})| \frac{\partial}{\partial \vec{R}} |n(\vec{R})\rangle.$$

The Berry connection is not gauge invariant. Because of this, for a long time it was thought that a sufficient gauge could always be chosen such that the Berry phase γ_n is always cancelled out. Only in 1984 did Berry realize that when the time dependent parameters R complete a cyclic evolution back to their starting value ($\vec{R}(t = t') = \vec{R}(t = 0)$), then a gauge transformation cannot remove γ_n. The Berry phase can be written as:

$$\gamma_n = \oint d\vec{R} \cdot A_n(\vec{R})$$

where $\vec{R}$ evolves along a closed path back to its starting value. Written in the form above, the geometric nature of the Berry phase is highlighted. The Berry phase only depends on the geometric path taken through parameter space, with no dependence on the speed taken along the path.

It is desirable to express the Berry phase in terms of a gauge invariant quantity rather than the gauge-dependent Berry connection. We can define the Berry curvature as the curl of the Berry connection, $\Omega_n(\vec{R}) = \vec{\nabla}_R \times \vec{A}_n(\vec{R})$, and employ Stokes' theorem to write

$$\gamma_n = \int_S d\vec{S} \cdot \vec{\Omega}_n(\vec{R})$$

The advantage of this formalism is that the Berry curvature is a gauge-invariant quantity, and we have removed explicit dependence on the gauge-dependent Berry connection.

TOPOLOGY IN CONDENSED MATTER

Since geometry and topology are related on a fundamental level, we can gain insight into what topology is by examining the topology of surfaces. It starts with the famous Gauss and Charles Bonnet formula, which describes the total curvature of an object:

$$\frac{1}{2\pi} \int_S K dA = 2(1 - g).$$

Here, *K* is the local curvature of the surface, and the integral is taken over an entire surface S. *g* is the number of handles or “holes” in the surface, dictating the topology of the surface. For example, a topologically trivial surface would be a sphere, with $g=0$. A torus would have *g*=1, and a pretzel with three holes would have *g*=3. The Gauss-Bonnet integral yields a somewhat striking quantization, as it is not immediately obvious that the left-hand side of the integral would yield quantized results depending on the surface topology.

The relation to condensed matter physics comes when we examine the geometry of eigenstates in k-space rather than the geometry of real-space surfaces. When applied to condensed matter physics, a formula similar to the Gauss-Bonnet formula often appears:

$$\int_S \vec{\Omega}(\vec{k})\, dA = 2\pi n.$$

Here, the local curvature K is replaced with the Berry curvature $\vec{\Omega}(\vec{k})$ and the integral is taken over crystal momentum space rather than real space (*4*), and the resulting integer *n* is called the Chern number. This topological viewpoint is important because physical properties such as the conductivity can depend on this Chern number. When this occurs, we would say that the conductivity of the system is dictated by its topology and cannot be changed without an intrinsic change of the fundamental topology and is therefore topologically protected. This is called topological protection because it protects the conductivity and/or other properties from impurities, since small perturbations do not change the topology of the system. Although this robust quantization makes topological materials exciting, there are difficult challenges to overcome before potential applications since many topological states so far have only been realized in low temperature and high magnetic field regimes.

QUANTUM HALL STATE

THE 2D, INTEGER QUANTUM HALL EFFECT

The 2D quantum Hall state is an example of a topological state of matter, but before reviewing how the quantum Hall state relates to topology, I will first review the fundamentals of what the quantum Hall effect and Hall effect are. The Hall effect is a transverse resistance measured in a crystal in the presence of a magnetic field originating from the Lorentz force. At high temperatures in a noninteracting 2D electron gas, the Hall resistance is usually linear with magnetic field, consistent with Boltzmann transport theory. At low temperatures and high magnetic fields, quantum effects become increasingly important and the quantum Hall effect (QHE) manifests. First measured by Klaus von Klitzing is 1980 while studying the hall conductivity of an electron gas at very low temperatures (*5*), the quantum Hall effect is the quantization of the Hall conductivity in integer multiples of e^2/h, as shown in Figure 1-1. Simultaneous to the Hall conductivity being quantized at these integer values, the longitudinal conductivity drops to zero except for brief intervals corresponding to when the Hall conductance switches integer values. These two features of quantized Hall conductance and zero longitudinal conductance are the trademarks of the quantum Hall state.

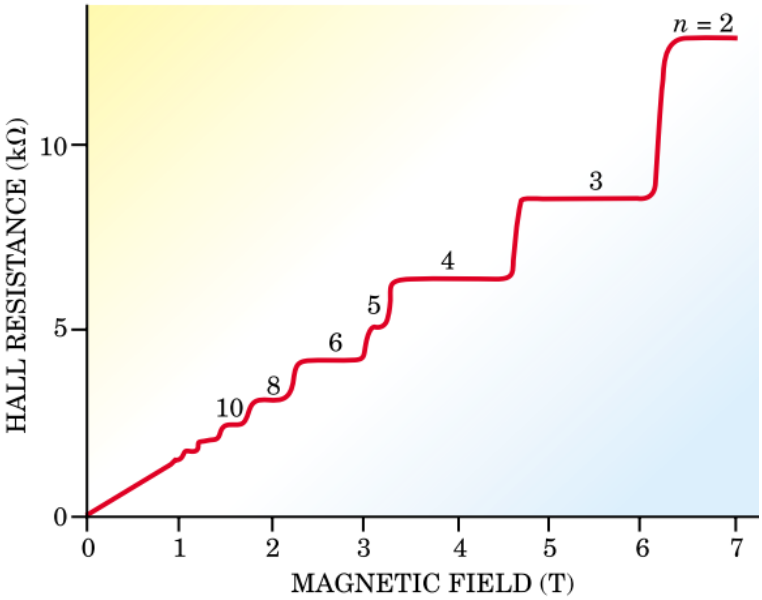

Figure 1-1: The quantum Hall effect. The Hall resistance displays a series of plateaus as a function of magnetic field. Taken from (*6*)

We can understand the QHE by examining the classical Hall effect and adding in appropriate quantum mechanical modifications. In the classical Hall effect, the Hall resistance of a 2D system is given by

$$R_{xy} = \frac{1}{ne}$$

where n is the number of electrons in the system. In high magnetic fields, the electrons form Landau level states, with each Landau level having a density of states n_ϕ states. It can be shown that the density of states of each Landau level is given by $n_\phi = \frac{B}{\phi_0}$, where ϕ_0 is the magnetic flux quantum, $\phi_0 = h/e$. We can express the total density of states n in terms of the Landau level density of states n_ϕ by introducing a filling factor ν, allowing us to write $n = \nu n_\phi$. Here, the filling factor ν pertains to the number of filled Landau levels, e.g., if one Landau level is filled $\nu = 1$, if two Landau levels are filled $\nu = 2$, etc. We can now write

$$R_{xy} = \frac{1}{\nu n_\phi e}$$

It might seem like we have arrived at a quantized Hall resistance already – R_{xy} is simply proportional to the number of filled Landau levels of the system. However, there is a concerning question: why does the filling factor ν get trapped at constant, integer values? If the system is clean, then as soon as one Landau level is filled, the Fermi energy should jump to the next Landau level, and we should never encounter regions of constant ν.

The answer is that impurities play a vital role in pinning the filling factor. Impurities create localized states with energies in between Landau level energies. Thus, when one Landau level is completely filled, the Fermi energy does not immediately jump to the next Landau level, but jumps through a series of available, localized impurity levels. As the Fermi energy enters these impurity levels, the filling factor of the delocalized Landau levels remains constant, and the Hall resistance is perfectly quantized. The result is quite surprising: while the pristine periodicity of the crystal is necessary for the formation of Landau levels that forms the basis of the quantum Hall effect, but the perfect quantization is only observable due to impurities creating plateaus.

THE TOPOLOGY OF THE QUANTUM HALL EFFECT

The relationship between the quantum Hall state and topology was established in the early 1980s when it was shown that the Hall conductivity can be written as an integral of the Berry curvature over the Brillouin zone (*2*, *7*). Explicitly, the hall conductivity in a 2D system can be written as:

$$\sigma_{xy} = \frac{e^2}{\hbar} \int_{BZ} \frac{d^2k}{(2\pi)^2} \Omega_{k_x k_y}$$

Here, $\Omega_{k_x k_y}$ is the Berry curvature. The topological invariance comes from the fact that the Berry curvature integrated over the Brillouin zone is a topological invariant that is quantized to an integer known as the Chern number. Denoting the Chern number as n, the Hall conductivity can be expressed as $\sigma_{xy} = n\frac{e^2}{h}$. The topological invariance of the Chern number and therefore the Hall conductivity stems from the fact that the Berry curvature is a geometric property, e.g., the Berry phase accumulated from the Berry curvature depends only on the path taken through phase space and does not depend on the length of time it takes to traverse this path. This is consistent with why the Berry phase is sometimes referred to as the geometric phase, and the geometric nature of the Berry curvature is intricately related to topological effects.

EDGE STATES IN THE QUANTUM HALL STATE

So far, we have discussed two fundamental properties of the quantum Hall state: quantized Hall conductivity and zero longitudinal conductivity. There is a final key feature of the quantum Hall state: the guaranteed existence of edge states. A simple explanation of this feature would be to consider the real-space motion of 2D electrons with an out of plane magnetic field. The electrons in the 2D bulk can be well-described by localized cyclotron motion. However, the at the edge of the sample, the cyclotron motion hits the edge of the sample. If the electron is specularly reflected, the resulting motion along the edge is a skipping orbit, as shown in Figure 1-2, left. The result is that the edge states of the 2D sample are filled with 1D motion, where electrons can only propagate in one direction.

In 1981 Halperin showed that the existence of these edge states is always guaranteed (*8*). The existence of these edge states and their connection to Landau levels can be reasoned from a spatial analysis of the bulk states. Electrons that would attempt to leave the bulk and enter the surrounding vacuum would encounter an energy barrier that keeps them confined to the bulk. At the edge of the sample, there is a bending of the Landau levels that creates this potential barrier, see Figure 1-2, right. Because of this effect, no matter where the Fermi energy lies, it always intersects an allowable energy state at the edge of the sample, and edge states are guaranteed to exist.

The guaranteed existence of edge states at the edge of a quantum Hall sample is a profound concept of topological physics. In building the framework of the modern-day theory of topology in condensed matter physics, Hasan and Kane emphasized the importance of these edge states, showing that these edge states correspond to a closing of the energy gap that must happen between the boundary of two regions with non-trivial and trivial topology (*9*). Hasan and Kane further pointed out that the interplay between topology and gapless states has appeared in many contexts in physics, including 1D field theory (*10*, *11*).

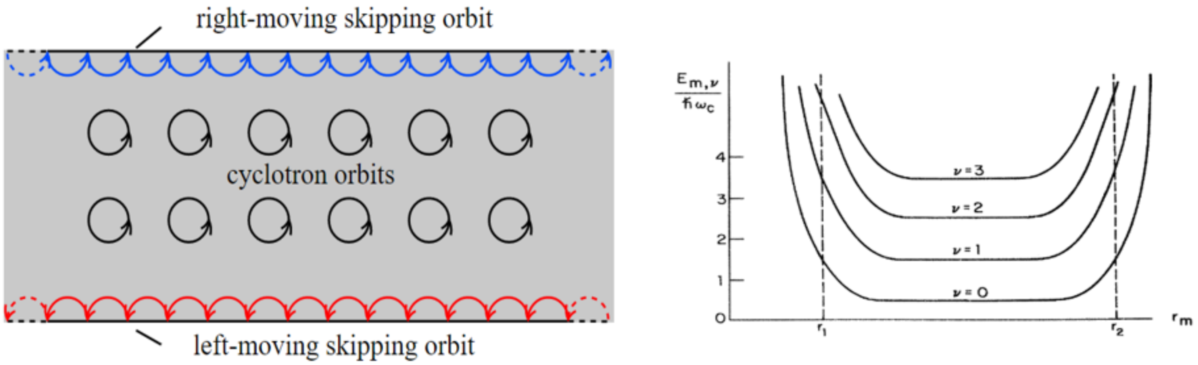

Figure 1-2: Quantum Hall edge states. Left: Electron motion with an out of plane magnetic field. In the bulk, electrons form cyclotron orbits. Along the edge, these orbits skip along the surfaces, resulting in one-way motion along the edge. Right: Landau level energy levels as a function of spatial parameter r. r_1 and r_2 correspond to the edge of the sample. The left image is referenced from (*12*), the right image is referenced from (*8*).

2D QUANTUM SPIN HALL STATE

The quantized edge conduction of the quantum Hall state is extremely resistant to scattering. This dissipationless conduction along the 1D edge channels has the potential for circuitry applications. Of course, the low temperatures and high magnetic fields associated with the quantum Hall state make applications nearly infeasible. While the low-temperature requirement remains a difficult hurdle to overcome from an application standpoint, the high magnetic field requirement can be overcome by the existence of a new topological state: the quantum spin Hall (QSH) state, which hosts similar edge conductance without the requirement of a magnetic field

The QSH state circumvents the requirement of a magnetic field through strong spin orbit coupling (SOC), where a charge carrier’s momentum is locked into a fixed relationship with its spin. Unlike the quantum Hall state with one 1D conduction channel per edge, the QSH state has two conduction channels per edge, one spin up and one spin down, as shown in Figure 1-3. First predicted in 2005 (*13*), the QSH state was experimentally confirmed in mercury telluride quantum wells in 2007 (*14*, *15*).

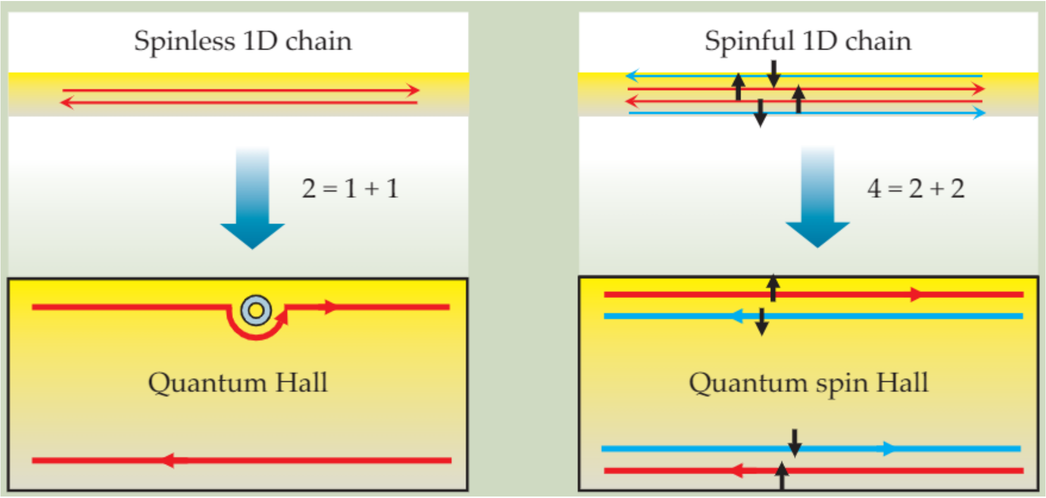

Figure 1-3: Edge states of the quantum Hall state (left) and the quantum spin Hall state (right). In the quantum Hall state, each edge has one conduction channel, for a total of two conduction channels. In the quantum spin Hall right, edge each has two conduction channels, one spin up and one spin down, for a total of four conduction channels. Image taken from (*16*)

In the QSH state, backscattering of edge states from non-magnetic impurities is forbidden by the laws of quantum mechanics. To see, this, consider an electron propagating along the edge that encounters an impurity. To backscatter off of this impurity, the electron will need to reverse its direction by either turning around in a clockwise or counter-clockwise fashion. These two options will rotate the electron spin by an angle of π or $-\pi$. As a result, the two different scenarios corresponding to clockwise or counter-clockwise reflection with have spins that have been rotated by 2π with respect to each other. A fundamental property of quantum mechanics is that if a fermionic wavefunction has its spin rotated by 2π, the rotated wavefunction will be the negative of the unrotated wavefunction. Therefore, the two reflected wavefunctions corresponding to clockwise and counter-clockwise reflection destructively interfere, and reflection from the impurity is prohibited, resulting in perfect transmission.

In the simple example of Figure 1-3, there is only one pair of left/right moving edge states (helical edge states) at each edge of the sample, and backscattering is forbidden. It can be shown that if there exist an even number of pairs of helical edge states, back scattering is no longer prohibited (*17*). This leads to defining the terminology of a Z_2 topological quantum number (*16*), which classifies if there is an even or odd number of helical edge states and whether the system is a QSH insulator.

3D TOPOLOGICAL INSULATORS, DIRAC & WEYL SEMIMETALS

The existence of topologically protected edge states in a 2D system creates the question of whether there is an allegory in 3D with topologically protected surface states. In the simplest case, 2D QSH insulators could be stacked one on top of each other, and the resulting 3D structure might have surface states that directly correspond to the stacked edge states. It turns out, this particular 3D state is one of three possibilities, and is called a “weak” topological insulator (WTI). A second possibility is called the “strong” topological insulator (STI) phase. In this phase, the final 3D state has conducting edge states not only corresponding to the original edge states, but all surfaces of the crystal have topologically protected surface states. Finally, the third possibility is that the 3D state is trivial, with no topologically protected surface states even if it’s built by stacking non-trivial 2D states.

Fu & Kane developed a very simple algorithm to predict whether a 3D system is a STI, WTI, or trivial insulator that works for crystal systems that are inversion symmetric (*17*). This algorithm calculates four Z_2 invariants, one primary (v_0) and three secondary (v_i). The primary invariant v_0 is calculated as:

$$(-1)^{v_0} = \prod_{i=1}^{8} \delta_i$$

Here, δ_i can easily be computed from the parity of each occupied energy state, and the pi-sum is over the eight time reversal invariant momenta (TRIM) points in the Brillouin zone. The secondary indices v_i are given by the same formula, but the pi-sum is over a single plane (four points) rather than all eight points.

The topological invariants are usually represented in the form v_0; (v_1 v_2 v_3) – eg, 0;000 would represent all invariants are trivial, and 1;(111) would represent all invariants are non-trivial. The primary topological index v_0 is 1 if the system is in the STI state with surface states on all surfaces, whereas $v_0 = 0$ implies a trivial insulating state if all the secondary indices are zero as well. $v_0 = 0$ but at least one non-zero secondary index would imply a WTI state, with the non-zero secondary indices determining which surface has protected states, see Figure 1-4 for more information.

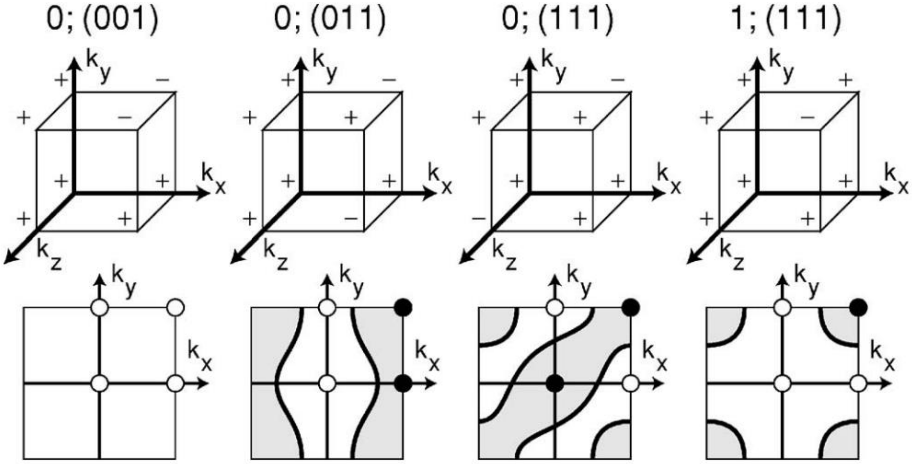

Figure 1-4: 3D Topological invariants. The left three columns have a trivial primary index but at least one non-trivial secondary index, and are WTIs. The far right is a STI. Taken from (*18*).

Since the topological indices depend on the parity of the filled eigenvalues, the only way for a topological index to change would be for a single (or odd number) of filled bands to change parity. This can only be done through band inversion – the process of the conduction and valance bands hybridizing and changing parity. In the band inversion process, the energy gap (E_G) between the valence and conduction bands becomes smaller and smaller until E_G=0 and there is no longer a bandgap in the system. Near this gapless state the energy dispersion is analogous to the Dirac dispersion for relativistic particles, $E = \sqrt{m^2c^4 + p^2c^2}$. In the condensed matter analogy, the speed of light c is replaced with the maximum velocity in the crystal v, and the mass term m is replaced with half of the energy gap, E_G/2. This analogy frequently leads to the E_G being called the massive term in the dispersion, and the final dispersion can be written as $E = \sqrt{E_g^2 + \hbar^2k^2v^2}$. At the “zero mass” state of E_G=0 the energy dispersion is linear in crystal momentum $\hbar k$, and is called the Dirac semimetal state. For the “massive” states E_G>0 the system can be either a trivial insulator, a STI, or a WTI.

If we consider a tuning parameter that is capable of closing and re-opening E_G, then the Dirac semimetal state corresponding to E_G=0 occurs at a singular value of this tuning parameter for materials with inversion symmetry (*19*). This Dirac semimetal state is always at least four-fold degenerate with Kramer’s degeneracy. In materials without inversion symmetry, however, a gapless state can be realized for a finite range of this tuning parameter. For non-inversion symmetric materials this gapless state can lift the Kramer’s degeneracy from the linear Dirac bands and create two sets of linear bands separated in momentum space that are no longer degenerate. In the example of a degenerate Dirac band centered at the Γ point, the breaking of inversion symmetry would create two, non-degenerate bands, each offset from the Γ point and centered at different points in momentum space.

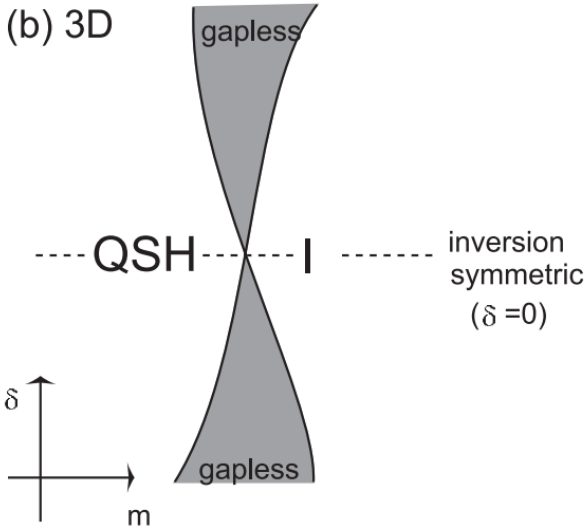

Figure 1-5: General phase diagram for 3D topological materials. The x axis is a tuning parameter that does not break inversion symmetry, but can close and reopen the bandgap. The y axis is a tuning parameter that breaks inversion symmetry

CHAPTER 2 - ZRTE$_5$: A TOPOLOGICALLY CRITICAL MATERIAL

ZrTe$_5$ is an orthorhombic single crystal that hosts a spectrum of unique and interesting properties. Originally capturing attention in the 1980s due to its unique resistivity dependence on temperature, it has been the focus of recent attention due to a 2014 prediction (*20*) that monolayer ZrTe$_5$ should be a quantum spin Hall insulator. Additionally, the 3D form of ZrTe$_5$ is predicted to be close to a topological phase transition between strong and weak insulating phases. Since 2014, electrical transport properties have been studied intensively and several novel behaviors have been reported. This work will focus on the following transport phenomena that I have explored during my Ph.D. work:

1. Chapter 4 will discuss a non-monotonic resistivity dependence on strain, suggesting strain can be used to tune the topological phase.
2. Chapter 5 will discuss an anomalous Hall effect in extremely low field, indicating large Zeeman splitting and spin-polarized transport.
3. Chapter 6 will discuss sharp dips in the magnetoresistance when the magnetic field is rotated perpendicular to the a axis, reminiscent of Lebed's magic angles and suggestive of a 3D Hofstadter butterfly

This richness of anomalous behavior in ZrTe$_5$ can be attributed to several factors. First, as has been noted, ZrTe$_5$ is "topologically critical" – it sits near the boundary of a topological phase transition between a strong and weak topological insulator (STI and WTI), with a Dirac semimetal phase at the boundary. This topological nature is accentuated in electrical transport because only the topologically non-trivial bands near the Γ point are close to the Fermi energy, with little to no interference from trivial bands which are all far away from E_F. Additionally, the topological criticality is further accentuated in ultra-pure crystal with few impurities, where E_F can be tuned to the Dirac nodal point or charge neutrality point. All novel behaviors in the list above are enhanced as E_F is tuned this charge neutrality point.

In addition to the topological criticality, ZrTe$_5$ also resides at the boundary between quasi-1D, quasi-2D, and 3D. The crystal structure is composed of tightly bound chains of ZrTe$_3$, suggesting quasi-1D behavior. However, the in-plane chain-to-chain binding is much stronger than the out of plane coupling, suggesting that ZrTe$_5$ may be more well described by a quasi-2D model rather than quasi-1D. This hierarchy of binding energies ($t_x > t_y > t_z$) is potentially responsible for at least one of the novel behaviors, the Lebed magic angle effect.

Finally, another key property of $ZrTe_5$ is its remarkably high mobility and mean free path. Figure 2-1 shows the mobility of $ZrTe_5$ approaches remarkably high values of $10^6 cm^2 \cdot V^{-1}s^{-1}$ as the carrier density decreases to values as low as $10^{15} cm^{-3}$. This extremely high carrier density rivals that of similar 3D Dirac semimetal Cd_3As_2 and Weyl semimetal TaAs (*21*, *22*). The mean-free path of ZrTe5 has been reported to be 320 nm or 583 nm for crystals with mobilities of 41,000 and 85,000 $cm^2 \cdot V^{-1}s^{-1}$ (*23*, *24*), as calculated by Liftshitz-Kosevich theory from analysis of quantum oscillations. Since the quantum oscillations of $ZrTe_5$ become immeasurable at extremely low carrier densities when the mobility is highest, it is difficult to exactly calculate the mean-free path associated with the extremely high mobilities of $10^6 cm^2 \cdot V^{-1}s^{-1}$. Given the extremely long mean free paths associated with previously reported $ZrTe_5$ crystals, it is reasonable to assume these mean free paths represent a lower bound for the extremely high mobility crystals grown in this work.

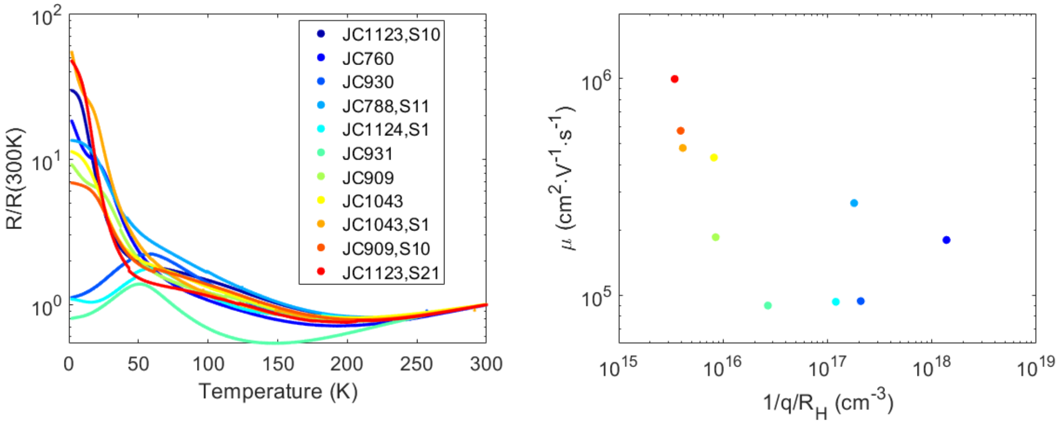

Figure 2-1: Effect of doping of resistivity and mobility. Left: resistivity dependence on temperature for flux-grown ZrTe5. Right: mobility dependence on carrier density. All measurements were performed on crystals grown in the Chu lab. For details related to the growth conditions and transport properties of these growths, see Table 3-1.

It is worth noting that $ZrTe_5$ displays at least three more striking transport properties that this work will not discuss in detail but are mentioned here for the sake of completeness. These properties are magnetoresistance oscillations that are periodic in log(B) rather than traditional Shubnikov de Haas oscillations that are periodic in 1/B, a 3D quantum Hall effect (*25*), and negative longitudinal magnetoresistance (*20*). Probing these properties with a perturbation such as strain and understanding their relationship to the topological phases of $ZrTe_5$ would be an interesting area of future work.

OVERVIEW OF ZRTE$_5$

$ZrTe_5$ is an orthorhombic layered structure in the *Cmcm* space group, shown in Figure 2-2. $ZrTe_5$ is inversion symmetric, but the inversion center is not located at the origin but rather (1/4, 1/4, 1/4). A key reason that electrical transport displays such rich behavior is that there is only one set of bands close to the Fermi energy E_F, as shown by Weng, Dai, and Fang (*20*) in their DFT calculations and supported by ARPES measurements. This set of bands is located at the Γ point and predicted to be largely composed of a basis of p_y orbitals of the dimer tellurium atoms, and whether these bands invert determines the topological phase. If inverted, the topological indices of the system are (1; 001), indicating a strong topological insulator with surface states on all surfaces. If not inverted, the topological indices are (0; 001) indicating a weak topological insulator with surface states only on the surfaces normal to the *c* axis. The topological phase is extremely sensitive to the lattice parameters of the crystal. In reference (*20*), the WTI phase was calculated if the DFT relaxed lattice parameters were used, while the STI phase was calculated if the experimental lattice parameters were used.

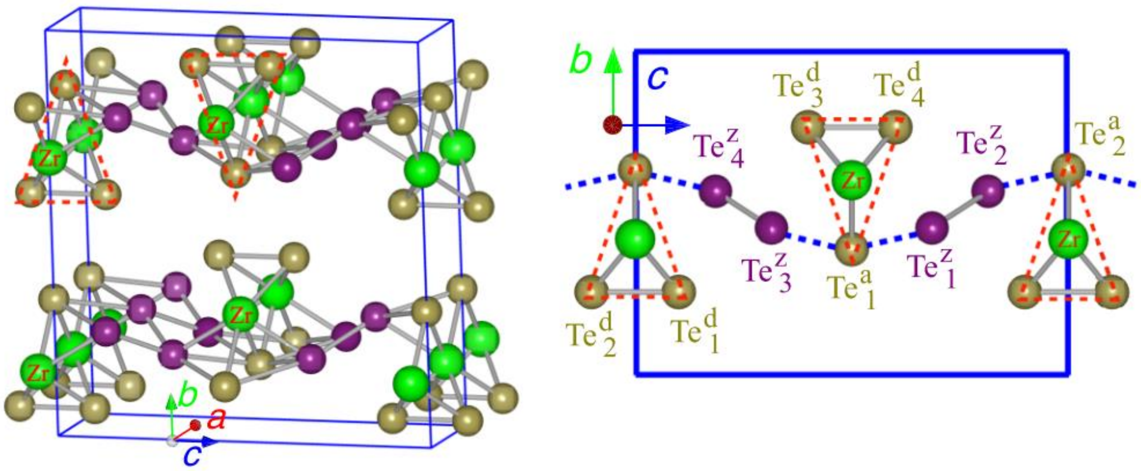

Figure 2-2: The crystal structure of $ZrTe_5$. Chains of $ZrTe_3$ extend along the *a* lattice direction. The $ZrTe_3$ chains are composed of one apical and two dimer tellurium atoms, denoted Te^a and Te^d. These chains are coupled in-plane in the *c* lattice direction by a zigzag chain of tellurium atoms, denoted Te^z. The planes stack in the out-of-plane *b* lattice direction. Figure taken from Ref. (*20*)

The band structure of $ZrTe_5$, calculated from both the DFT relaxed lattice parameters as well as the experimental lattice parameters, is shown in Figure 2-3. Aside from the topologically non-trivial bands at the Γ point, very little interference from other bands close to E_F is present. The closest interference is between the Y and M points for which an *n*-type band approach the same energy level as the bottom of the conduction band at the Γ point, but this is still a higher energy than the Γ point band.

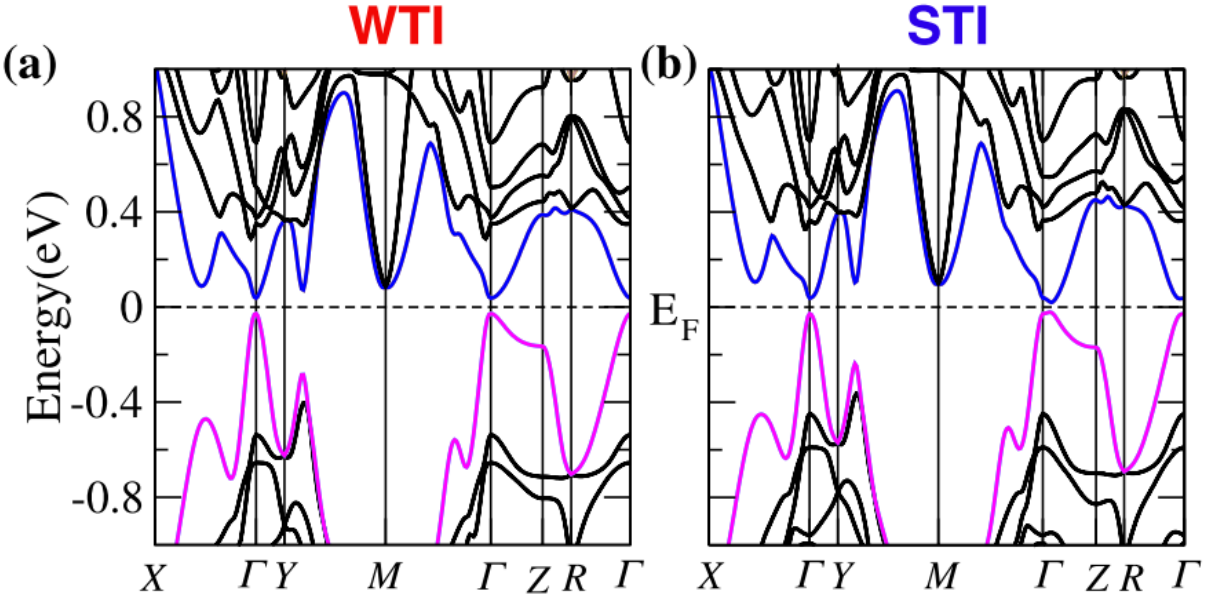

Figure 2-3: Bulk band structure of $ZrTe_5$. In panel (a), DFT-optimized lattice parameters are used in the calculation, and the system is found to be in the WTI state. In panel (b), experimental lattice parameters are used, and the system is found to be in the STI state. Figure taken from Ref. (*26*).

Novel transport properties associated with the topological non-trivial bands at the Γ point become more prominent if E_F can be tuned to the charge neutrality point. If the system is in the DSM phase, tuning E_F to the charge neutrality point may yield interesting transport effects associated with the Dirac nodal point. Alternatively, if the system is in the WTI or STI phase, tuning E_F to the charge neutrality point may allow for the observation of surface states, which have energy levels inside the bulk gap. Experimentally, $ZrTe_5$ single crystals with extremely low carrier densities have been fabricated. However, the carrier density of $ZrTe_5$ can vary significantly from growth to growth, depending on growth technique (flux versus chemical vapor transport) and purity of the starting materials. This is evident from the wide range in transport behavior for $ZrTe_5$ reported in literature, where both the temperature dependence and magnetoresistance of $ZrTe_5$ display vastly different behavior depending on crystal purity. A quick gauge to calibrate the proximity of E_F to the charge neutrality point is to examine the resistivity temperature dependence, which displays a distinct shape. As seen in Figure 2-4, CVT-grown crystals display an anomalous peak in the resistivity – temperature relation, while flux-grown crystals display this peak resistance at base temperature. As pointed out in Ref. (*27*), this can be understood in terms of a Lifshitz transition where the Fermi level crosses the charge neutrality point at the temperature associated with the peak resistivity. In the CVT-grown crystals the crystal is *p*-type at 300K with E_F located below the charge neutrality point. As the crystal is cooled, E_F shifts to higher energies and eventually becomes *p*-type at base temperature. In the flux-grown crystals, this the peak resistivity occurring at base temperature indicates that E_F is tuned to the charge neutrality point at base temperature.

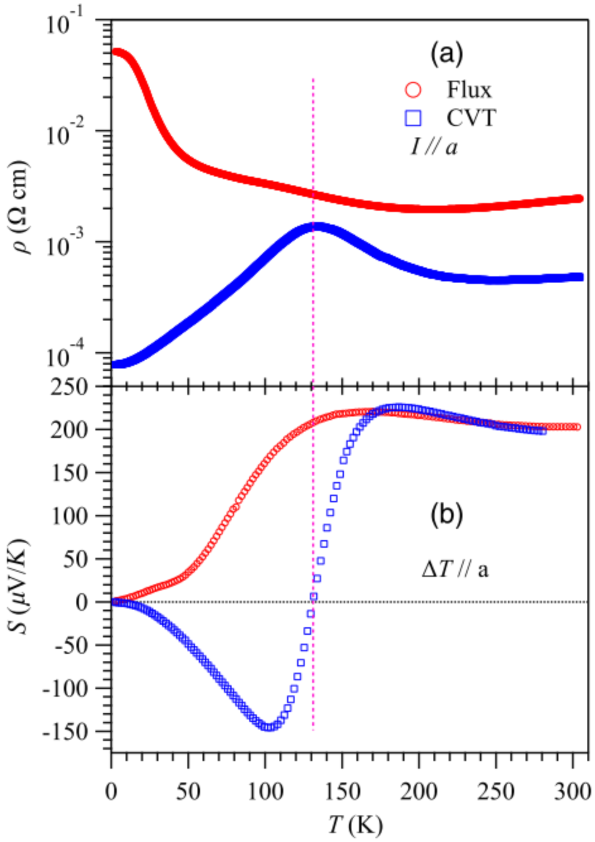

Figure 2-4: Resistivity and thermopower versus temperature for $ZrTe_5$ single crystals. The red data correspond to crystals grown by the flux method, while the blue data correspond to crystals grown by chemical vapor transport. Figure taken from Ref. (*27*)

CHAPTER 3 - GROWTH & MEASUREMENT METHODS

CRYSTAL GROWTH

$ZrTe_5$ is grown by primarily two different methods: the flux growth method and the chemical vapor transport (CVT) method. The flux growth technique is known to produce crystals much closer to the ideal 1:5 stoichiometry ratio, approximately 1:4.98, while the CVT method has more Te vacancies with a ratio of approximately 1:4.86 (*28*). Here I will review the two main growth techniques, although most of the results in this work are focused on the ultra-pure flux method.

FLUX GROWTH METHOD

For the flux growth method, zirconium and tellurium pellets are loaded into a quartz ampule, sealed under vacuum, heated to high temperature (800-900 °C) to melt the elements, cooled somewhat rapidly to the crystal formation temperature (505 °C), and then slowly cooled to 460 °C. At 460 °C the quartz ampule is taken out of the furnace and decanted – that is, spun in a centrifuge to separate the solid crystal from the liquid tellurium flux. This process is shown schematically in Figure 3-1, and well documented in literature (*29*). A separator is usually inserted in the quartz tube with the elements to allow decanting to occur – some material that will allow liquid tellurium to pass through but block the $ZrTe_5$ crystals. After decanting and cooling to room temperature, the quartz ampule is broken and single crystals of $ZrTe_5$ are extracted.

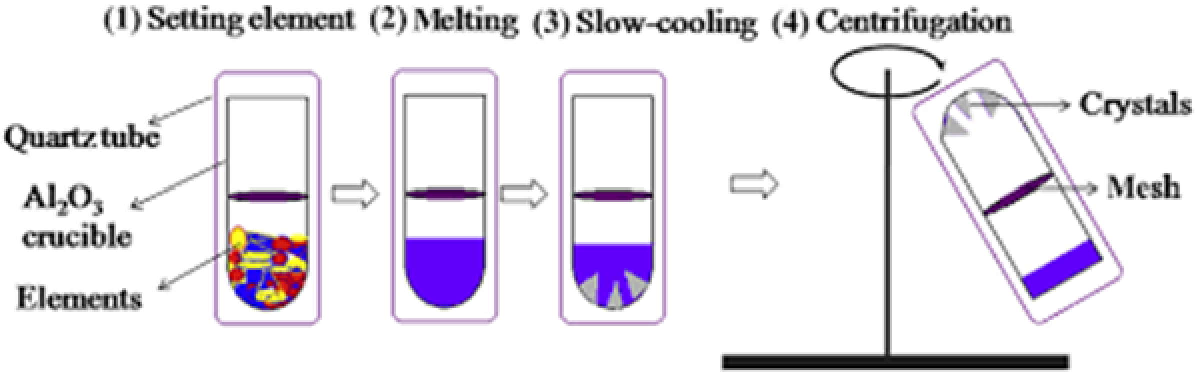

Figure 3-1: Schematic of flux-growth process. Elements are loaded into a crucible, then sealed in vacuum inside a quartz tube. The quartz tube is taken to high temperatures to melt the elements, then slowly cooled to crystallize the material. The tube is taken out of the furnace at a high temperature and decanted to separate the crystals from the melted flux. Figure referenced from (*30*)

There are several variables that can impact the quality of the fabricated crystals. Below is a list of several variables I took into consideration when growing $ZrTe_5$.

- **Purity of the starting materials.** This is perhaps the most control parameter if one wishes to fabricate ultra-pure, low carrier density crystals. I typically used 99.9999% pure tellurium shot or lumps (Alfa Aesar) for all of my flux growths. Since it is more difficult to find commercially available zirconium with as high of a purity rating as tellurium, zirconium is typically the limiting agent that determines purity. 99.95% pure pellets of zirconium are commercially available (Alfa Aesar), and growths using this Zr purity typically yield crystals of carrier density $p{\sim}10^{16}cm^{-3}$. If ultra-pure crystals are desired, I found that arc melting 99.95% pure zirconium resulted in much cleaner zirconium, yielding crystals of $p < 10^{15}cm^{-3}$.
- **Flux ratio.** The flux method works on the principle that excess tellurium is loaded into the quartz ampule, and $ZrTe_5$ crystalizes in a sea of liquid tellurium. I typically used Zr:Te flux ratios from 1:100 to 1:400 and saw little to no variation in the carrier density resulting from the flux ratio. Flux ratios around 1:50 started to yield $ZrTe_5$ mixed with $ZrTe_3$ single crystals, which were easily identifiable due to the different morphology of the crystals.
- **Furnace cycle.** The typical furnace cycle I used involved heating to 900 °C, staying at 900 °C for three days to completely melt and homogenize the mixture, then cooling to 505 °C over two days. At 505 °C crystallization begins to occur, as indicated by the binary phase diagram of Zr and Te (*31*). At 505 °C, it is important to slowly cool the furnace to allow the formation of large crystals. Typically, the furnace is cooled to 460 °C over the course of three days. It was reported (*32*) that iteratively rapidly heating back to 505 °C and slowly cooling to 445 °C results in growing larger crystals, since small crystals will be completely melted during reheating and large crystals will survive and grow larger. I did several growths with this iterative method and found that this method did enhance crystal size, both for rapid re-heating times of one hour as well as three hours. I always cooled over the course of three days for the cooling cycle. The final cooling is always to 460 °C for decanting.
- **Amount of material loaded.** $ZrTe_5$ crystals typically grow with widths (along the *c* axis) less than 100 microns. Since this dimension is crucial for Hall effect measurements, it is greatly desirable to grow larger crystals. This can be aided by the furnace cycle as

mentioned, as well as simply loading more starting material. If a Canfield crucible set is used, the amount of material able to be loaded is 3-5 grams. However, if elements are directly loaded into the quartz ampule rather than into a Canfield crucible set, 20-30 grams of material can be loaded at once. A plug of quartz wool can be used as the decanting separator rather than the Canfield filter.

- **Separator used for decanting.** For ultra-pure $ZrTe_5$ ($p < 10^{15} cm^{-3}$), it was found that elements loaded directly into the quartz glass with no Canfield crucible set resulted lower carrier densities than when the elements were loaded into a Canfield set. Presumable the alumina from the Canfield set added dopants in small concentrations to the crystals.
- **Cleanliness of the quartz ampule.** The quartz tubes were usually cleaned by sonicating DI water in the tubes for 20 minutes to knock off impurities from the side of the quartz tubes. Afterwards, isopropanol alcohol (IPA) was sonicated inside the tubes for another 20 minutes, then the tubes dried on a hot plate to evaporate any remnant water or IPA.

Below I present a table of flux ZrTe5 growths I completed during my Ph.D. studies. I limit the table to growths I performed Hall effect measurements on in order to report the effect of the growth parameters on the carrier density, as measured by the zero-field slope of the Hall resistance. I note several other transport properties, such as peak resistance temperature, mobility at 2K, R(2K)/R(300K), and 300K resistivity. The mobility is measured somewhat unconventionally as the low-field magnetoresistance quadratic coefficient, $\frac{\Delta\rho}{\rho_0} = \mu^2 B^2$, although it can also be inferred by comparing the 2K resistivity value with the Hall resistance.

	Growth Conditions				Transport Properties				
JCID #	Flux Ratio	Furnace cycle	Zr source	Canfield set?	$\rho(300K)$ $(m\Omega cm)$	$\rho(2K)$ $/\rho(300K)$	μ $(\frac{m^2}{Vs})$	$\frac{1}{qR_H}$ (cm^{-3})	T_{peak} (K)
103	1:200	1	A.A. 99.95%	no	1.35	10.3	229	3.8E+14	
111	1:200	2	A.A. 99.95%	no					
292			A.A. 99.95%		0.67	7.6	36	3.8E+14	2K
759	1:100	3	A.A. 99.95%	Yes	0.23	5.3	59	3.1E+16	2K
760	1:50	3	A.A. 99.95%	Yes	0.37	18.3	-	2.2E+15	2K
788	1:200	3	A.A. 99.95%	No	0.67	13.4	30	0.0E+00	2K
788	1:200	3	A.A. 99.95%	No	0.52	3.8	32	-1.5E+17	6K
789	1:200	3	A.A. 99.95%	No	0.51	8.8	63	5.7E+15	2K
909	1:100		A.A 99.5%	No	0.34	9.2	16	4.2E+15	2K
909	1:100		A.A 99.5%	No	0.38	6.9	71	8.7E+15	5K
928		2	A.A 99.5%	No	1.35	0.3	305	3.7E+15	19K
930	0.5:0.5:100				0.62	1.1	14	1.4E+15	59K
931	0:1:60				0.81	0.8	13	-2.0E+17	51K
947					1.54	0.3	21	2.7E+16	2K
957					0.61	1.3	21	1.2E+16	71K

974	1:200	1	Arc melted	No	1.13	21.7	201	1.7E+16	2K
1043	1:200	2	CGI Zr	No	0.21	11.3	43	2.3E+14	2K
1043	1:200	2	CGI Zr	No	0.39	54.2	60	6.1E+15	2K
1043	1:200	2	CGI Zr	No	1.01	8.6	75	3.6E+15	2K
1123	1:200	1	Arc melted	No	0.50	47.2	136	3.3E+14	2K
1123	1:200	1	Arc melted	No	1.00	22.9	252	3.1E+15	2K
1124	1:200	1		No	1.04	1.1	12	1.7E+14	59K
1328	1:200	1	Arc melted	No	0.6	15	195	1.2E+15	2K
1470	1:200	2	Arc melted	No	1.5	16.7	121	2.1E+14	2K

Table 3-1: Growth conditions and transport properties of flux grown $ZrTe_5$. If the flux ratio contains two numbers, it is the Zr:Te ratio. If three numbers, it is the Zr:Hf:Te ratio. The furnace cycles are listed in Table 3-2. The growths listed here correspond to the measurements shown in Figure 2-1.

Furnace cycle #	**Description**
1	To 900 °C in 9 hours, maintain 3 days, cool to 505 °C in 48 hours; Iterate 2 times: Cool to 440 °C in 72 hours and warm to 505 °C in 1 hour Cool to 460 °C in 72 hours, maintain and decant at 460 °C
2	To 900 °C in 9 hours, maintain 3 days, cool to 505 °C in 48 hours; Iterate 2 times: Cool to 440 °C in 72 hours and warm to 505 °C in 3 hour Cool to 460 °C in 72 hours, maintain and decant at 460 °C
3	To 900 °C in 9 hours, maintain 3 days, cool to 515 °C in 48 hours; Cool to 460 °C in 72 hours, maintain and decant at 460 °C
4	To 900 °C in 9 hours, maintain 3 days, cool to 510 °C in 48 hours; Cool to 460 °C in 72 hours, maintain and decant at 460 °C

Table 3-2: Furnace cycles used in ZrTe5 growths.

CHEMICAL VAPOR TRANSPORT METHOD

In the chemical vapor transport of $ZrTe_5$, zirconium, tellurium, and iodine are loaded into a glass ampule, usually approximately 10 inches long. The basic premise is that the ampule is loaded into a two-zone furnace and each end of the ampule is heated to a different temperature. The end of the ampule where the starting materials are loaded is referred to as the source zone of the reaction, while the other end is referred to as the growth zone, since $ZrTe_5$ single crystals will crystallize in this end. The most likely chemical equation that that occurs during the growth process is as follows (*33*):

$$ZrTe_5(s) + 2I_2(g) \leftrightarrow ZrI_4\ (g) + 5Te\ (g)$$

For the CVT growths I conducted, I followed the methodology published in Ref. (*34*). Here, Zr and Te were first baked into a precursor material by loading Zr and Te in a 1:5 ratio and heating to 500 °C. Next, the precursor $ZrTe_5$ material and iodine (about 5 mg cm^{-3} of iodine) were loaded into the source end of a quartz ampule, and the source end was heated to 520°C while the growth end was heated to 450 °C, and the temperature gradient was maintained for ten days. After the growth periodic, the ampule was taken out of the furnace, cracked open, and single crystals of $ZrTe_5$ were extracted from the growth end.

The important consideration while performing the CVT growth is that crystallization will begin when ZrI_4 gas and Te gas backwards react to form $ZrTe_5$ (s). The reaction is usually seeded by reacting with an impurity spot inside the quartz ampule. To grow large crystals, it is desirable to minimize the impurities on the inside surface of the quartz tubes, so that fewer, bigger crystals form rather than many, smaller crystals. This is accomplished by carefully cleaning the inside of the quartz tubes through sonicating with distilled water and IPA, as well as ensuring the starting precursor material is not crushed to a powder but rather a solid chunk.

BULK PREPARATION

Both the flux-growth and CVT-growth techniques produce single crystals that must be handled delicately lest they bend/break. While tweezers can be used to pluck crystals from the initial growth, handling with tweezers will damage and bend the crystals. Once a crystal has been extracted, it is best to not handle with tweezers, but rather transport by balancing on the edge of a knife blade. Crystals can be easily trimmed to size along the long (*a* lattice direction) to remove any bent portions from handling with the tweezers.

To prepare for electrical transport measurements crystals are masked after extracting, allowing only small portions of the crystal surface to be exposed to the line-of-sight gold sputterer (see Figure 3-2, top panel). The crystal is then placed in a sputtering chamber and approximately 70 nm of gold is sputtered onto the crystal. After sputtering, the mask is delicately removed with tweezers and 25-micron (or 12-micron for very small crystals) diameter gold wire is adhered with silver paint. The gold wire is adhered by dipping the wire in a puddle of silver paint, then placing the wet end of the wire on the crystal and gently removing the tweezers. This process of applying the gold wires by hand is the most difficult part of the process and requires a steady hand and practice.

To make effective hall contacts the proper choice of silver paint is very important. If the crystal is less than ~200 microns wide, as is most often the case for $ZrTe_5$, it is very difficult to place wires with industry standard DuPont Silver 4929 or 4922 paint, even if the paint is thinned with 2-Butoxyethyl-acetate. The DuPont silver paint with harden in a matter of seconds if the gold wire is dipped in a sufficiently small puddle of paint, and the paint will not effectively adhere to the crystal. Alternative silver paints such as 2-part Silver Conductive Epoxy, H20E EPO-TEK (Ted Pella) also will not work with $ZrTe_5$ since they require heat to cure and $ZrTe_5$ will degrade in heat. The silver paint with sufficiently low viscosity, long drying time, and heat-free curing that enables Hall contacts on crystals <100 microns wide is Precision Fiber Products (PFP) 9110LV 2-part epoxy mixed with ultra-fine silver flakes (Metz metallurgical #5)[1]. First, the PFP 910LV 2-part epoxy is mixed with its catalyst in a 10:3 ratio. After the epoxy is mixed, the epoxy and ultra-fine silver flakes are mixed in a 1:3.2 ratio to form a slow drying, low viscosity epoxy. The epoxy has a working window of 0.5-1 hours, and fully cures at room temperature in about 14 hours. Use of this silver paint is a crucial tool in making Hall contacts on very narrow crystals, see the bottom panel of Figure 3-2.

---

[1] Many thanks to Stan Tozer from National High Field Magnetic Lab (NHFML) for showing me this method.

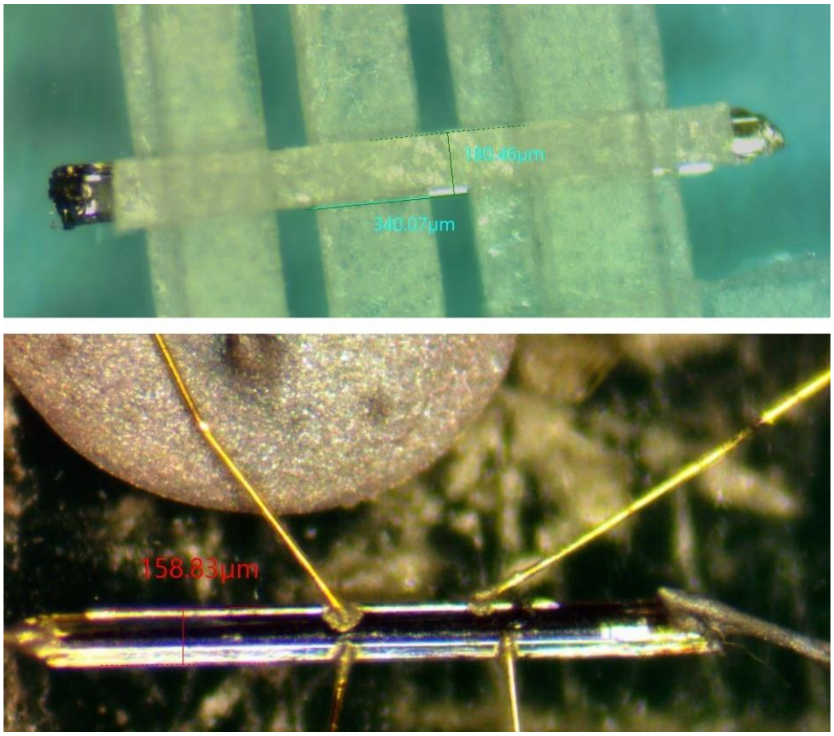

Figure 3-2: Wiring of bulk, single crystal $ZrTe_5$. In the top panel, a single crystal (approximately 170 microns wide) is masked, leaving small portions of the crystal exposed for gold sputtering. In the bottom panel, the crystal has been sputtered with gold, removed from the mask, and wires have been attached by hand to with silver paint and 25-micron diameter gold wire.

BULK STRAIN PREPARATION

To apply large amounts of strain to bulk single crystals, a home-built three-piezo apparatus was machined out of titanium, similar to other three-piezo apparatuses reported in literature (*35*). By applying positive (negative) strain to the outer two piezostacks and negative (positive) strain to the inner piezostack, a small (~0.5mm) gap can be lengthened or contracted, shown in Figure 3-3 (A). By gluing a crystal across this gap, uniaxial stress can be applied to the crystal. If wires are attached to the crystal prior to gluing to the strain apparatus, the crystal resistivity can be measured as a function of controllable stress.

Setting up the strain experiment requires precise hand-eye coordination and care to not break or bend the crystals. $ZrTe_5$ is especially prone to bending if mishandled during set up or if too much negative strain is applied during the experiment. If any bending of the crystal is present, the resistivity-strain relationship will develop a large hysteresis and will be very evident. To set up the experiment, first a single crystal is wired as described in the previous section. Next, the wires near the crystal are carefully bent upwards with tweezers to allow for the crystal to sit flush on the titanium surface. Next, drops of Stycast epoxy are applied to the titanium surface, and the $ZrTe_5$ crystal is partially submerged in these drops of epoxy [2]. Since $ZrTe_5$ oxidizes in heat, the Stycast epoxy cures at room temperature over approximately 16 hours. To fully connect the electronic wiring, 30-34 gauge copper wire is bent within close (~1 cm) proximity of the crystal and the 25 micron gold wire leads attached to the crystal. It is extremely difficult to bend the 30-34 gauge copper wire to touch the gold wire, so another set of “jumper” gold wires is usually attached to connect the copper wire to the gold wires coming off of the crystal, and adhered with silver 4929 paint. A resistive strain gauge can be glued to one of the piezo stacks and used to estimate strain delivered to the crystal.

One of the advantages of the 3-piezo method is that there is minimal thermal strain imparted to the crystal. If glued directly to the side wall of a piezo stack, the thermal strain (with zero voltage applied to the piezo stack) imparted to the crystal is large, since the piezo stacks anomalously expand with decreasing temperature. If glued across the gap in the 3-piezo apparatus, the thermal strain (again, with zero voltage applied to the piezo stacks) is much smaller, resulting from the difference in thermal contraction between the crystal and the titanium material that it is glued to. Even though the thermal strain in the three-piezo method is much smaller compared to the single-piezo method, the thermal strain can still be a significant consideration, especially if the crystal might break or bend from too much tensile or compressive strain. To mitigate this, it is useful to attempt to offset the thermal strain by adjusting the piezo voltage during cooling.

---

[2] 5 minute epoxy (5ME) can be used instead of Stycast epoxy, but the 5ME is more prone to cracking due to thermal cycling if multiple heating/cooling cycles are employed.

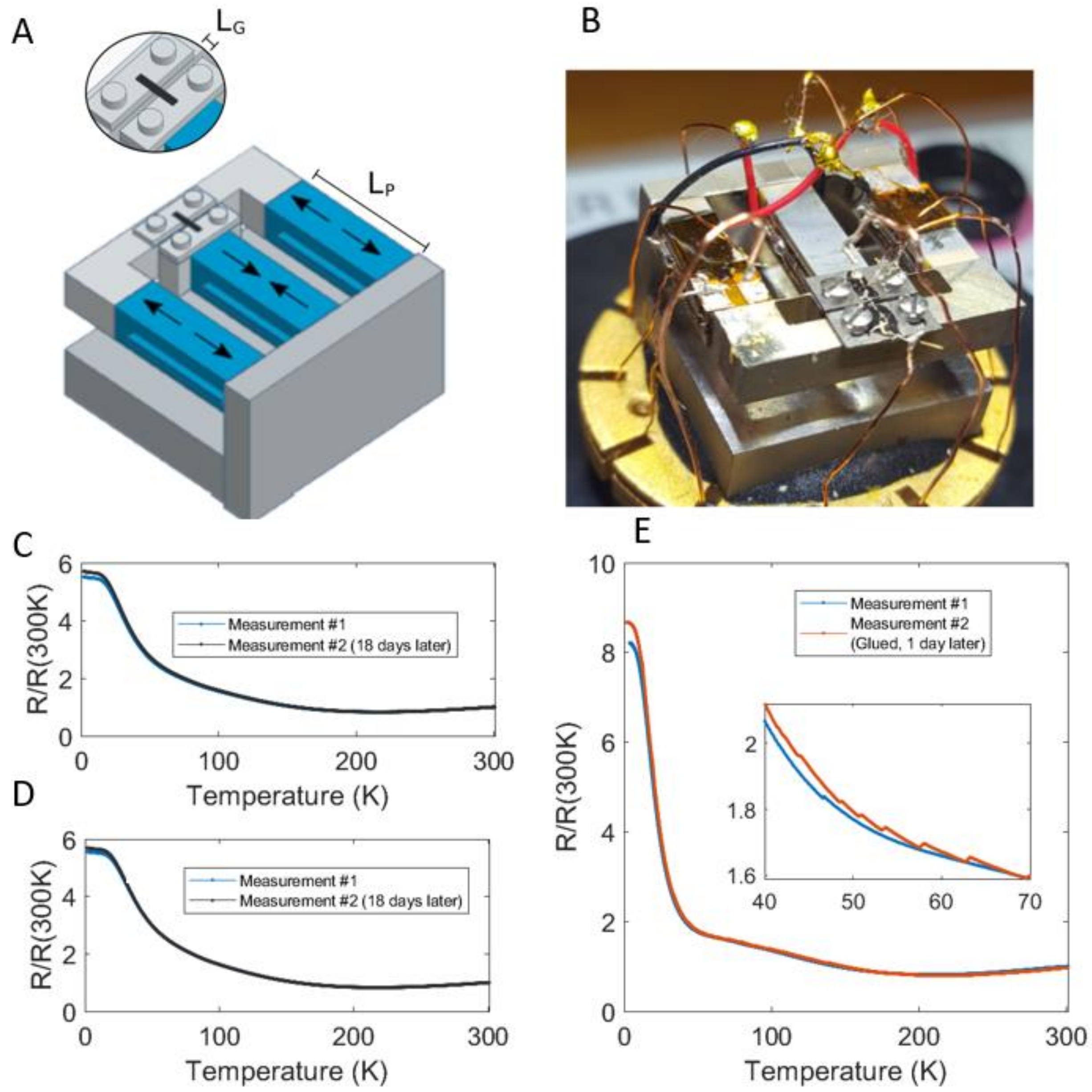

Figure 3-3: Three-piezo strain apparatus and methodology of calibrating zero-strain state. A-B, schematic and picture of the three-piezo strain apparatus. C-D, the oxidation/aging effect the hinders calibrating to the zero-strain state below ~50K. E, the resistivity of $ZrTe_5$ glued to the apparatus (red) compared to a freestanding calibration (blue). Discontinuities in the red data correspond to adjusting the piezo voltage to minimize thermal strain.

Offsetting the thermal strain by controlling the piezo stack voltage requires knowledge of the voltage corresponding to the zero-strain state of the crystal. This is difficult to accurately accomplish, but a rough calibration can be achieved by first measuring the resistivity versus temperature of the crystal prior to gluing to the strain apparatus. If the crystal is sensitive to strain (which $ZrTe_5$ is), the thermal strain while glued to the apparatus will significantly alter the resistivity compared to the freestanding dataset. By comparing the freestanding and glued resistivity curves, the voltage on the piezo stacks can be adjusted to minimize the difference between the two measurements, which places the glued crystal in a strain state close to the freestanding crystal. Figure 3-3 (E) shows the data for a glued crystal resistivity superimposed over the freestanding resistivity. Discontinuities of the resistivity in the glued state correspond to the voltage of the piezo stacks being adjusted to minimize the difference between the two curves. In practice, using the freestanding resistivity measurement to calibrate the zero-strain state of the glued crystal works well for $ZrTe_5$ down to about 30K-50K. Below these temperatures, there is typically an oxidation/aging effect that changes the resistivity of the crystals even with no applied strain (see Figure 3-3 C&D). At this point the freestanding resistivity can no longer be used as a calibration to the freestanding state. Despite this limitation, eliminating the thermal strain at temperatures above 50K proved sufficient to mitigate extremely large thermal strains that could potentially break or bend the crystal.

ESTIMATION OF BULK STRAIN TRANSMISSION

We used the *ANSYS Academic Research Mechanical 19.1* finite element analysis software to calculate the strain transmission in the primary axis and deformation in the secondary axis for all $ZrTe_5$ samples measured in

- Strain-tuned topological phase transition in ZrTe5. The model is shown in Figure 3-4. The stiffness tensor for ZrTe$_5$ was taken from a previously calculated value by the Materials Project. The sample is modelled as mounted to the strain apparatus in a puddle of epoxy. The Young's Modulus and Poisson's ratio of the epoxy are given the same values as the work done by Hicks (*36*). For each crystal measured, the model took the exact crystal dimensions and gap size of the apparatus as inputs, and computed an average relaxation constant α, defined as $\epsilon_{aa} = \alpha\epsilon_{xx}^{disp}$ for $\epsilon_{xx}^{disp} = \pm 0.1\%$, where ϵ_{aa} is the strain delivered to the crystal. Our results are shown in Table 3-3.

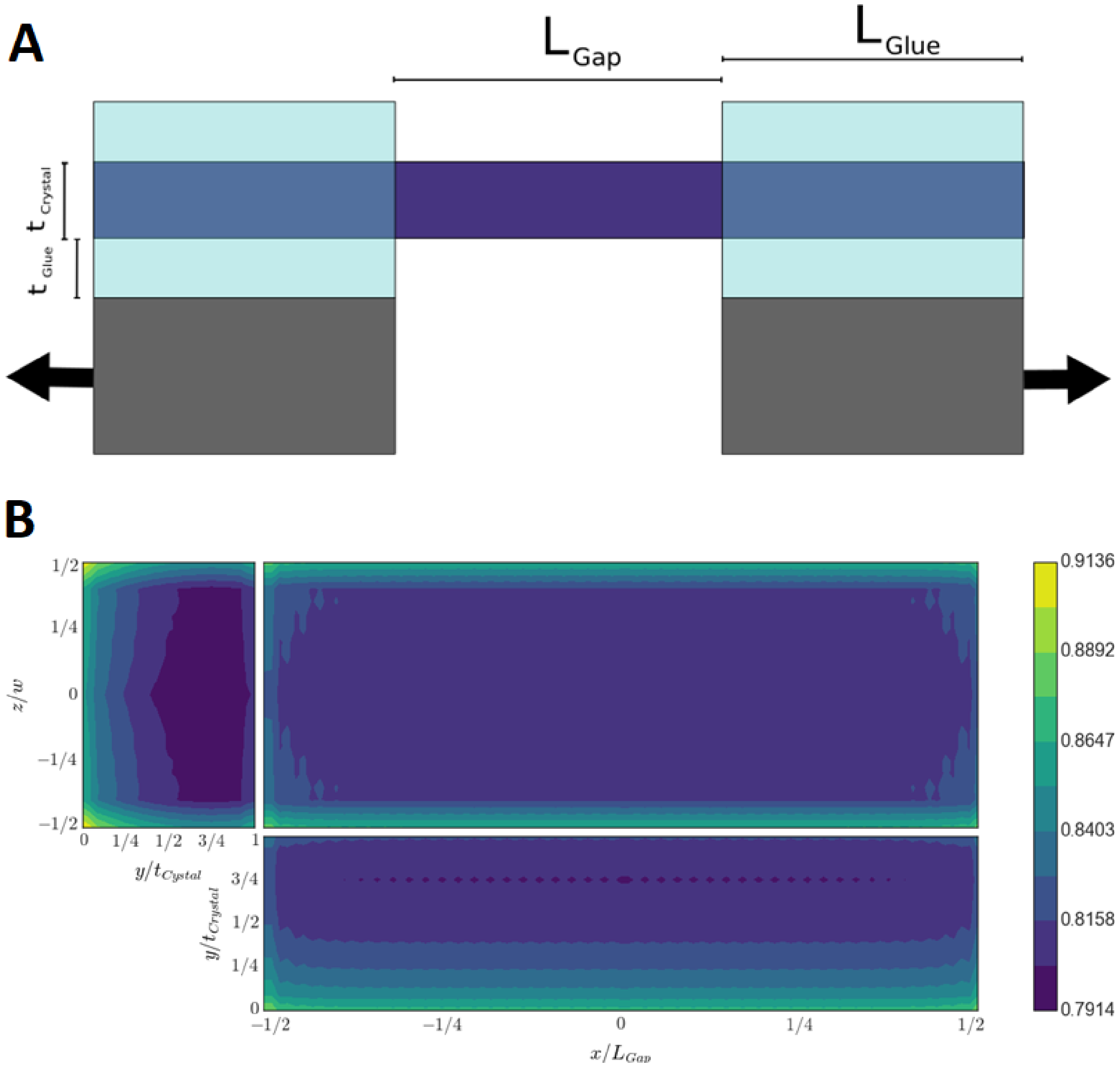

Figure 3-4: Finite element analysis of strain transmission. (**A)** Schematic of system modelled by finite element analysis. For our analysis, we assumed $t_{Glue}/t_{Crystal}$=0.5 and L_{Glue}/L_{Gap}=1, reasonable assumptions given optical images of the experiment. (**B)** Strain transmission α

averaged through the length (upper left), thickness (upper right), and width (bottom right) of the crystal, modelled after a crystal with dimensions of Growth 1, Sample 2.

Sample	Growth	(L_G:w:t) (μm)	α
S1	1	962:60:10	0.93
S2	1	1,060:120:40	0.81
S3	1	490:21:15	0.89
S4	2	800:40:60	0.82
S5	1	0.77:0.03:0.02	0.90

Table 3-3: Finite element analysis of strain relaxation. Dimensions of apparatus gap (L_G), crystal thickness, and crystal width are reported for each crystal in this work. The average strain relaxation α is calculated from these parameters by finite element analysis. The deformation in the vertical axis, Δy, is also calculated.

NANODEVICE PREPARATION

A portion of this work conducted transport measurements on exfoliated flakes of $ZrTe_5$ that were up to 350 nm thick. These devices were processed using standard exfoliation and electron-beam lithography (EBL) techniques. Since most nanodevice fabrication using these techniques is usually focused on fabricating much thinner samples (typically several nanometers thick), I will briefly review the methodology for fabricating the 350 nm thick device.

The exfoliation process is straightforward for $ZrTe_5$. Standard scotch tape methods can yield satisfactory exfoliated flakes. The exfoliated flakes behavior like their bulk counterparts in that it is difficult to isolate wide exfoliated flakes for Hall measurements. While the bulk crystals can be 100 microns wide, it is difficult to find exfoliated flakes wider than 5 microns wide if the flake is ~100 nm thick. For flakes ~50nm thick or thinner, flakes 2-3 microns wide can be found with some difficulty. Pre-treated the silicon substrate with plasma cleaning seems to marginally improve exfoliated flake yield and size.

After a satisfactory flake is discovered, atomic force microscopy (AFM) can be used to verify flake thickness and surface uniformity. Next, choosing an appropriate photoresist thickness is critical for successful EBL. It is recommended to spin coat a photoresist that is ~3 times thicker than the thickness of the exfoliated flake. For the 350nm thick flake shown in Figure 3-5, 1 layer of PMMA A6 followed by 2 layers of PMMA A4 were spin-coated onto the chip. Each layer was spun for

10s at 800 rpm, 60s at 4,000 rpm, and followed by a 5-minute curing time at 125 °C. Because $ZrTe_5$ is known to degrade in heat, 125 °C is the maximum recommended curing temperature, and colder/longer cures may be desirable for thinner flakes. The final thickness of the photoresist was measured at 1100 nm by AFM, close to the target of 3x the thickness of the exfoliated flake. During the EBL process, a dosage of 420 $\mu C/cm^2$ was sufficient to process the 1100 nm of photoresist. After EBL writing, the exposed photoresist was developed by submerging the chip in a cold 3:7 water:IPA mixture for 40 seconds, followed by 10-20s rinsing with IPA and gently drying with nitrogen gas. 5nm of a vanadium sticking laying followed by 430nm of gold (2 Å/s) were evaporated with an E-beam evaporator. The excess photoresist was lifted off by soaking overnight in acetone, followed by an acetone rise.

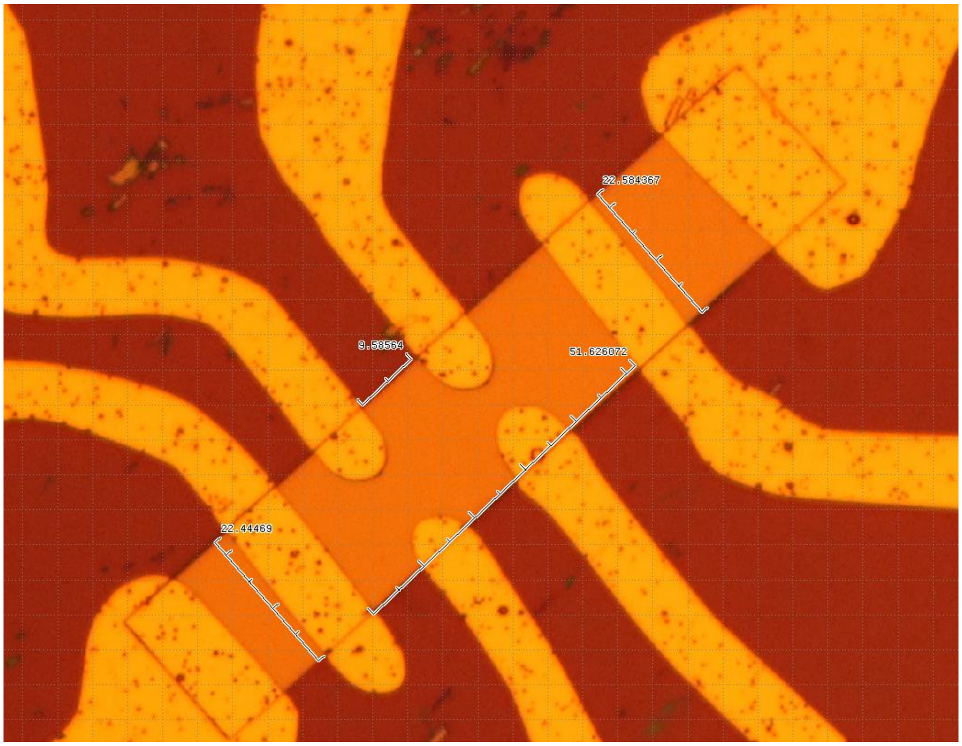

Figure 3-5: 350nm exfoliated flake of $ZrTe_5$ with evaporated gold contants. The fabrication details are discussed in the main text.

CHAPTER 4 - STRAIN-TUNED TOPOLOGICAL PHASE TRANSITION IN ZRTE5

Strong and weak topologically insulating phases are predicted to have surface states on all (strong) or some (weak) of the surfaces of the crystals. Currently there is a lack of experimental evidence that clearly displays the differences between these two phases. In this chapter I introduce using strain as a control mechanism to control the topological phase of $ZrTe_5$. This tuning parameter of strain can easily be used to modulate the topological phase of $ZrTe_5$ down to the lowest temperature we measure, 2K. The boundary between the two phases is marked by a minimum in the resistivity-strain relationship, and differences in the longitudinal magnetoresistance at strains above and below this critical strain indicate distinct topological phases across this boundary. The work presented in this chapter is published in Ref. (*37*), and recently ARPES measurements further corroborate this work (*17*, *38*, *39*).

INTRODUCTION

A phase transition between topologically distinct insulating phases involves closing and reopening the bandgap. Near the topological phase transition, the bulk energy spectrum is characterized by a massive Dirac dispersion, where the bandgap plays the role of mass. We report measurements of strain dependence of electrical transport properties of $ZrTe_5$, which is known to host massive Dirac fermions in the bulk due to its proximity to a topological phase transition. We observe that the resistivity exhibits a pronounced minimum at a critical strain. We further find that the positive longitudinal magnetoconductance becomes maximal at the critical strain. This non-monotonic strain dependence is consistent with the switching of sign of the Dirac mass, and hence a strain-tuned topological phase transition in $ZrTe_5$.

Appreciation of the topological aspects of band structure has fundamentally changed the way we understand the electronic properties of solids. Band insulators with time reversal symmetry can be classified into normal insulators (NI), weak topological insulators (WTI) and strong topological insulators (STI) based on their Z2 topological indices (*38*, *39*). Changing Z2 indices requires closing and reopening the bandgap, and topologically distinct insulating phases are separated by a gapless Dirac or Weyl semimetal phase. The relationship between these phases is summarized in the general phase diagram proposed by Murakami et al. (*9*, *40–44*), as shown in Figure 4-1A. These topological phases have been intensively studied in the past decade (*37*, *45*, *46*). In contrast, the transition between these phases is less explored because it requires changing the band parameters of the solid. It has been demonstrated that topological phase transitions can be induced either by chemical doping or thermal lattice expansion (*20*). Nevertheless, the precise in-situ control of topological phase transition in a three-dimensional system is still an outstanding challenge.

The transition-metal pentatellurides $ZrTe_5$ is an ideal material to realize in-situ control of topological phase transitions. $ZrTe_5$ is a van der Waals (vdW) layered material crystallized in the Cmcm orthorhombic space group. Each layer consists of $ZrTe_3$ chains extending along the a-lattice direction, and the layers are stacked along the b-lattice direction (Figure 4-1B). The material has received significant interest because its mono-layer form is predicted to be a large bandgap quantum spin Hall insulator (*20*, *47*, *48*). It was also suggested that the three-dimensional bulk band structure is very close to the phase boundary between WTI and STI (*49*), indicated by the red line in the universal phase diagram shown in Fig. 1A. Early studies of optical conductivity (*50*, *51*), quantum oscillations (*31*), photoemission, and negative longitudinal magnetoresistance (*52*–*55*) have supported the predicted Dirac semimetal-like band structure in the bulk, with a single Dirac point at the center of the Brillouin zone, Γ. Unlike topological Dirac semimetals such as Na_3Bi or Cd_3As_2, there is no additional crystalline symmetry to protect the Dirac point in $ZrTe_5$, and more recent spectroscopy measurements revealed that its band structure is better described by a massive Dirac dispersion, where mass plays the role of bandgap. The bandgap size measured by different experiments varies, ranging from 10 to 80 meV, and there are conflicting reports on whether the material is a WTI or STI (*55*). These experimental findings suggest that the electronic structure of $ZrTe_5$ may be very sensitive to external perturbation, such as lattice distortion.

In this work, we present evidence for a strain-tuned topological phase transition corresponding to a sign change of the Dirac bandgap in $ZrTe_5$. This conclusion is a result of extensive measurements of bulk electrical transport of $ZrTe_5$ as a function of in-situ tunable anisotropic strain. Although the measurement of surface states is often regarded as the smoking gun evidence of topological insulators, close to a topological phase transition the small bandgap and the Dirac like dispersion in the bulk impose severe challenges for identifying surface states (*53*, *54*). Here we focus on the bulk transport properties, which are highly sensitive to the mass of bulk Dirac fermions near a topological phase transition. We observe that the resistivity exhibits a non-monotonic strain dependence and reaches a minimum at a critical strain. The non-monotonic strain dependence is distinct from the expected behavior of a conventional semiconductor, yet it is consistent with the sign switching of the Dirac mass of a gapped Dirac semimetal. We further discover that the negative longitudinal magnetoresistance also shows a non-monotonic strain dependence and becomes maximal at the critical strain. The extracted helicity relaxation time increases by tenfold as the strain approaches the critical value. Our study presents $ZrTe_5$ as a promising platform for on-demand control of nontrivial topological properties of materials.

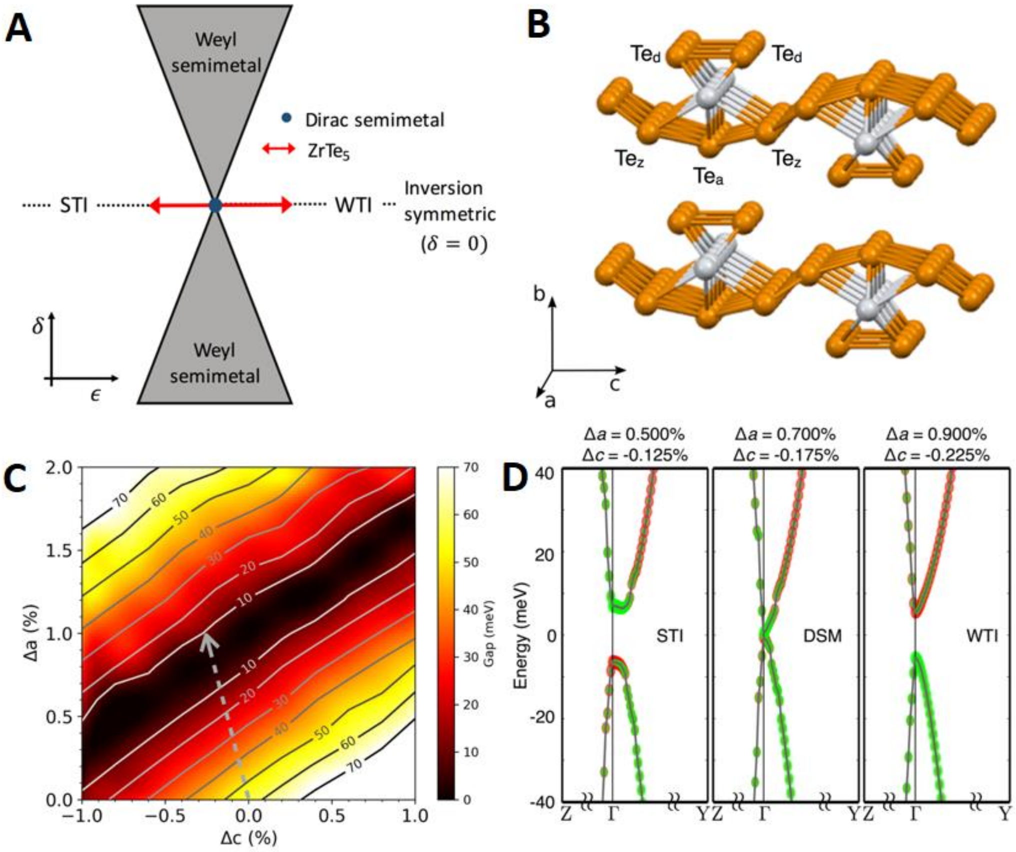

Figure 4-1: Topological phase diagram and band structures of $ZrTe_5$. **(A)** Universal Phase diagram of topological insulators proposed by Murakami for a 3D system. The control parameter δ describes the breaking of inversion symmetry. The control parameter ϵ does not break inversion symmetry. **(B)** Crystal Structure of $ZrTe_5$. Chains of $ZrTe_3$ prisms (consisting of Te_a and Te_d atoms) extend along the a-axis. These chains are connected by Te_z atoms along the c-axis to form layers. These layers are van der Waals bonded in the b-axis direction. **(C)** The size of bandgap E_g at the Γ point as functions of strains in the a and c lattice directions. The dashed grey arrow indicates the anisotropic strain induced by a uniaxial stress along the a-axis direction, as governed by the calculated Poisson's ratio $\epsilon_{aa} = -4.0\epsilon_{cc}$. **(D)** Band structures for different strain states taken at points along the Poisson's ratio path. These points (from left to right) correspond to strong topological insulator, Dirac semimetal, and weak topological insulator,

respectively. Fermi level is defined as the zero energy, and the k-point labeling is based on the primitive unit cell. A band inversion involving Te_d and Te_z p orbitals (shown respectively as red and green colors) is seen in the strong topological insulator phase. Band structure calculation data courtesy of Wei-Chih Chen and Cheng-Chien Chen.

RESULTS

Figure 4-1C shows a contour map of the size of the bandgap E_g at Γ as a function of ϵ_{aa} and ϵ_{cc}, i.e. strain (%) along the a and c lattice directions, calculated by density function theory (DFT). It shows a V-shaped valley, with the minimum of the valley (corresponding to $E_g = 0$) extending along the diagonal direction. Z_2 topological indices were also computed, and the $E_g = 0$ line is indeed the phase boundary between STI and WTI (see Fig. S7). Figure 4-1C reveals a highly anisotropic strain dependence of E_g: the steepest gradient of E_g is along the direction in which ϵ_{aa} and ϵ_{cc} have opposite sign, as the case when a uniaxial stress is applied along the a-lattice direction. In contrast, the strain induced by applying hydrostatic pressure corresponds to a trajectory that is almost parallel to the contour lines. The Poisson's ratio of the anisotropic strain, $\epsilon_{cc}/\epsilon_{aa} = -0.25$, induced by a-axis uniaxial stress was obtained using a fully relaxed vdW-DFT calculation[3], and it is indicated as the grey arrow in Figure 4-1C. It requires less than a percent of ϵ_{aa} to reach the WTI-STI phase boundary. We note that there is uncertainty in the DFT bandgap size for a given set of lattice constants. For example, several spectroscopy measurements reported E_g as low as 10 meV, which is significantly lower than the calculated 60 meV bandgap at zero-strain (*27*, *56*). Hence, the actual strain required to pass through $E_g = 0$ could be smaller (see Figure 4-1D).

We use the bulk electrical transport to study the putative strain-tuned topological phase transition in $ZrTe_5$. As the bulk energy bandgap closes and reopens, the electrical transport properties, such as resistivity, will fall and rise again. The resistivity is determined by the properties of quasiparticles near the chemical potential, hence the strain effect on resistivity will be larger if the doping is lower so that the chemical potential is closer to the band edge. Therefore, we used the flux method to grow single crystals of $ZrTe_5$, which is known to yield crystals closer to perfect chemical stoichiometry with ultra-low carrier density (p-type 10^{15} cm^{-3}) (*55*, *57*). Figure 4-2C shows the resistivity as a function of temperature for several free standing $ZrTe_5$ single crystals

---

[3] The change of b-lattice constant has a much weaker effect on the bandgap, the inclusion of which makes no qualitative change to the argument.

before they were mounted on the strain apparatus. The insulating temperature dependence is consistent with other flux-grown crystals in the literature, indicating that at base temperature the chemical potential of our samples lies just slightly below the valence band maximum (*34*, *58*).

Uniaxial stress was applied along the a-axis of the $ZrTe_5$ crystals using a piezoelectric apparatus introduced by Hicks et al. (*53*, *54*, *59*) as shown in Figure 4-2D. Resistivity (ρ_{aa}) and strain (ϵ_{aa}) were measured along the a-axis (Materials and Methods). The strain dependence of the resistivity, i.e. the elastoresistivity, is non-monotonic at T = 2K, as shown in Figure 4-2A. For all samples measured, the resistivity shows a minimum at a critical strain ϵ_{min}, and increases as the sample is strained away from ϵ_{min}. There is an uncertainty in determining the zero-strain state, i.e. the absolute value of ϵ_{min}, due to the mismatch of thermal contraction between the sample and apparatus. Nevertheless, based on a detailed analysis we estimated $\epsilon_{min} < 0.1\%$ (Methods). For all the data shown here, ϵ_{aa} is measured from ϵ_{min}. We note that although the size of the strain response varies from sample to sample, the appearance of a resistivity minimum is a robust phenomenon seen in every case. It is well known that the resistivity of semiconductors can have a large *linear* response to strain due to its sensitivity to the position of band edges as a function of strain. Such a *non-monotonic* strain dependence is very unusual but is precisely what is expected for the STI-WTI topological phase transition as described above.

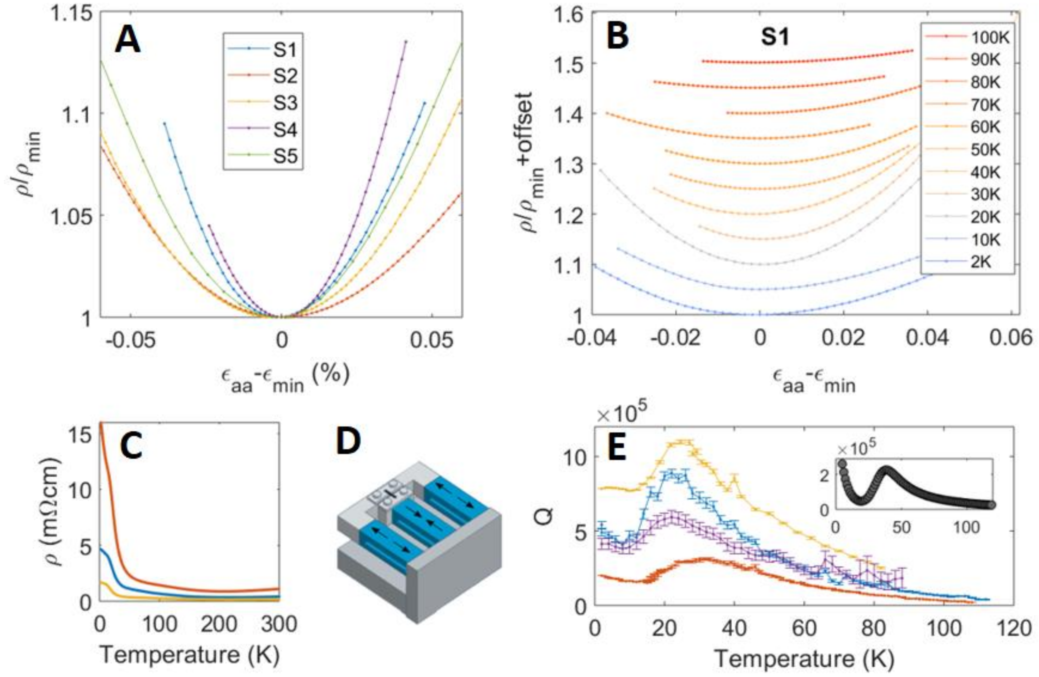

Figure 4-2: Temperature and strain dependence of resistivity of $ZrTe_5$. (**A)** Strain dependence of resistivity of $ZrTe_5$ at T = 2K for five samples S1-S5. A clear minimum in resistivity can be seen for each sample. The resistivity is normalized by its minimum value ρ_{min} , which varies between 1 and 16 $m\Omega cm$. The x axis is the strain along the a-lattice direction, which is estimated based on the method described in the Methods section. (**B)** Resistivity versus strain for temperatures between 2K and 100K. A clear minimum can be seen for the entire temperature range. (**C)** Resistivity versus temperature for three $ZrTe_5$ crystals S1-S3, as measured prior to gluing onto the 3-piezo strain apparatus. (**D)** 3-piezostack apparatus used to deliver strain. (**E)** Quadratic coefficient Q obtained from fitting $\frac{\rho}{\rho_{min}} = 1 + Q\ (\epsilon_{aa} - \epsilon_{min})^2$. The sensitivity of the response to strain shows a non-monotonic temperature dependence, as discussed in the main text. (**E, inset)** The coefficient Q computed using Boltzmann transport equations (Materials and Methods). The main calculated features agree with the experimental data: a local minimum then maximum is seen with increasing temperature. The relative strength and temperature of these features depend on the carrier density input into the model, see the Methods section for more information.

The nonmonotonic elastoresistivity is quadratic and symmetric around ϵ_{min}. This is consistent with expectations based on the massive Dirac Hamiltonian, which has been shown to successfully describe the magneto-optical spectrum of $ZrTe_5$ (*60*). In general, the $k \cdot p$ Hamiltonian of a small bandgap semiconductor gives a dispersion $E(\boldsymbol{k}) = \pm\sqrt{m^2 + \hbar^2 v_\alpha^2 k_\alpha^2}$ where m, which is half of the bandgap $E_g = 2|m|$, is analogous to the rest mass of a relativistic free particle, and v_α, k_α are the Fermi velocities and crystal momentum. Since the strain (ϵ_{aa}, ϵ_{bb} and ϵ_{cc}) induced by the uniaxial stress does not break the D_{2h} point group symmetry of $ZrTe_5$, the parameters of the Hamiltonian, including m, should vary linearly with strain. The band inversion process corresponds to the change in the sign of m as it is tuned through zero by strain. However, the physical observables that determine the resistivity, including bandgap, density of states and velocity, do not depend on the sign of m and thus must vary as m^2 to lowest order. As a result, the resistivity will also be parabolic in strain.

The linear elastoresistivity coefficient in non-degenerate semiconductors is proportional to the ratio of deformation potential ($\partial E_g/\partial\epsilon$) to temperature ($k_B T$) (*26, 53*). We derive a similar relation for the quadratic elastoresistivity coefficient measured in $ZrTe_5$. At low temperature in the quantum degenerate regime when $k_B T \ll E_F$, the Fermi energy E_F plays the same role as $k_B T$. Based on dimensional analysis, the quadratic coefficient $\Delta\rho/\rho$ is determined by *m* normalized by E_F:

$$\frac{\Delta\rho(\epsilon)}{\rho} \approx \left(\frac{m}{E_F}\right)^2 = \left(\frac{\frac{\partial m}{\partial \epsilon}}{E_F}\right)^2 \epsilon^2$$

We also performed a Boltzmann transport calculation and obtain the same expression. The calculation assumes the simplest situation where fixed number of relativistic electrons are scattered from charged impurities (Materials and Methods). This expression agrees with the expectation that the sensitive of resistivity to strain decreases as the chemical potential moves away from the band edge. Using the deformation potential, $\partial m/\partial\epsilon$, calculated by DFT in the above formula, a fit of the quadratic coefficient yields a Fermi energy of 4-8 meV and a carrier density of $0.3 - 2.4 \times 10^{15}\mathrm{cm}^{-3}$. These values are comparable with ARPES and transport measurements of similar samples (*31*). We also measured the elastoresistivity at higher temperatures, which shows quadratic behavior up to 100K. The quadratic coefficient exhibits a non-monotonic temperature dependence, as shown in Figure 1-1E. This is a consequence of a crossover from the quantum degenerate to non-degenerate regime as temperature increases. By including the Fermi-Dirac distribution in the Boltzmann transport calculation, we are able to reproduce the non-monotonic temperature dependence of the quadratic coefficient, as shown in the inset of Figure 4-2E. The overall qualitative agreement suggests that the transport properties of $ZrTe_5$ are well captured by the dynamics of massive Dirac fermions with a strain tunable mass across a wide temperature range.

If the bandgap is truly zero at ϵ_{min}, then the band structure at that point is equivalent to a massless Dirac semimetal, which is known to host the chiral anomaly when electric and magnetic fields are parallel. A manifestation of the chiral anomaly is negative longitudinal magnetoresistance, which has been observed in $ZrTe_5$ previously (*61, 62*). This effect was initially considered in gapless Weyl or Dirac semimetals (*63*), yet for a gapped Dirac semimetal essentially the same mechanism could still apply in the semiclassical regime provided that E_g/E_F << 1 (*36*). In a gapped Dirac semimetal electron helicity plays the same role as chirality in gapless semimetals. The helicity relaxation rate is proportional to $\left(E_g/E_F\right)^2$. As a result, we expect a suppression of negative longitudinal magnetoresistance (i.e. positive longitudinal magnetoconductivity) when the bandgap opens.

To investigate this, we measured the strain dependence of longitudinal magneto-transport ($I \parallel B \parallel \boldsymbol{a}$, see Materials and Methods for field alignment). Figure 4-3A-B show the resistivity versus field for different strain states. A negative longitudinal magnetoresistance is clearly observable, and it disappears if the field is misaligned by more than one degree (see supplementary Figure 6 of (*31*, *57*)), consistent with the literature (*36*). At $\epsilon_{aa} = \epsilon_{min}$ (grey curves) the negative longitudinal magnetoresistance reaches its maximum, and it is progressively suppressed when the sample is strained away from this point. Two other samples were measured and show the same strain dependence (see supplementary Figure 5 of (*50*, *56*)). The magnetoresistance shows an upturn once the field surpasses the quantum limit (estimated to be 2T for 10^{15} cm^{-3} carrier density) (*64*). We notice that the upturn is shifted to higher fields on the STI side, which may be related to the unusual behavior of lowest Landau levels of topological insulators (*63*). Nevertheless, we leave the study of high field magnetoresistance for future works and focus on the weak field semiclassical regime (B < 0.5T), in which the magnetoconductance $\Delta\sigma = \sigma(B) - \sigma_0$ is positive except showing a small dip near zero field (Figure 4-3C) [4]. The magnetoconductance was fitted with a quadratic field dependence, $\sigma = \sigma_0 + \alpha B^2$. The quadratic coefficient α is proportional to the helicity relaxation time (*19*), and it shows tenfold increase as ϵ_{aa} approaches ϵ_{min} (Figure 4-3D). This diverging behavior is consistent with the suppression of helicity relaxation due to the vanishing of the bandgap at $\epsilon_{aa} = \epsilon_{min}$.

---

[4] The small dip in longitudinal magnetoconductance near zero field is commonly observed in other materials that exhibit chiral anomaly. Its origin is not completed understood. Two possibilities are weak antilocalization effect and the classical Lorentz longitudinal magnetoresistance in anisotropic metals that saturates when $\omega_c\tau \sim 1$.

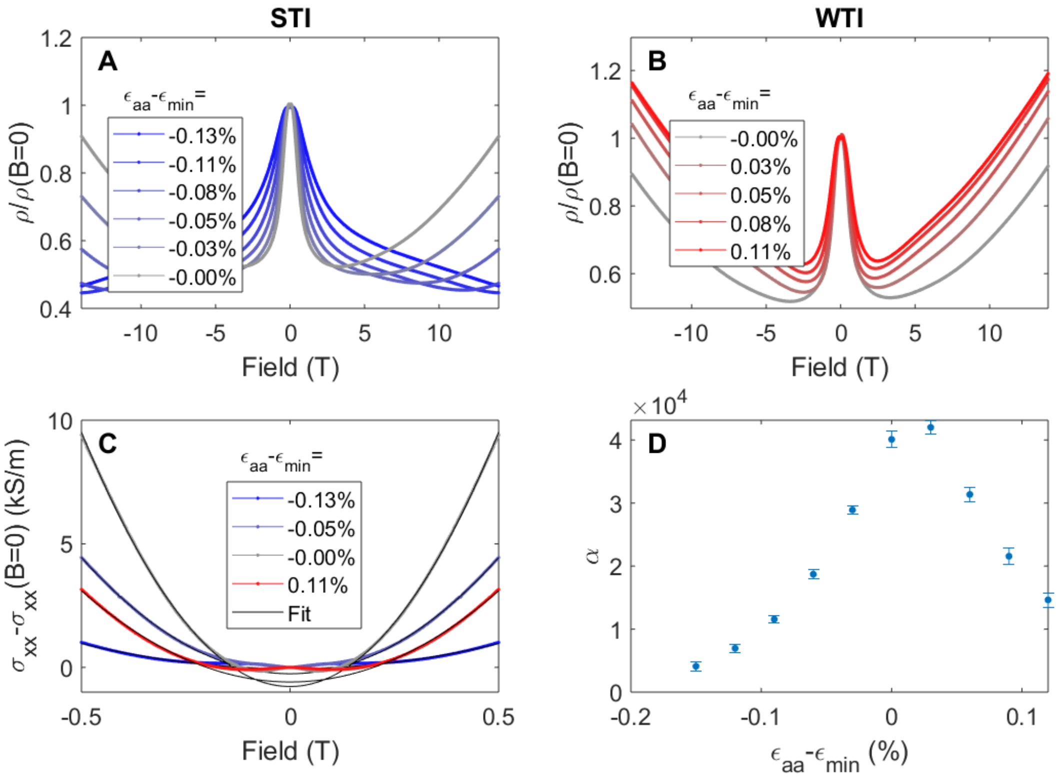

Figure 4-3: Strain dependence of Longitudinal magnetoresistance and magnetoconductance of $ZrTe_5$ at T = 2K. Negative longitudinal magnetoresistance for negative strains **(A)** and positive strains **(B)** measured relative to ϵ_{min}, corresponding to the STI and WTI phases, respectively. The negative magnetoresistance is strongest at ϵ_{min}, at which $ZrTe_5$ is a gapless Dirac semimetal. Straining the crystal away from ϵ_{min} suppresses the negative magnetoresistance. **(C)** Weak field positive magnetoconductance for several strain setpoints close to ϵ_{min}. The conductance is fitted to the equation $\sigma(B) = \sigma_0 + \alpha B^2$ (black solid curves), where α is a positive coefficient proportional to the helicity relaxation time. **(D)** The quadratic coefficient α as a function of strain measured relative to ϵ_{min}.

DISCUSSION

Our extensive transport measurements and detailed data analysis have revealed an exceptionally delicate topological ground state of $ZrTe_5$. The highly non-linear elastoresistivity from a non-symmetry breaking strain is consistent with the sign switching of the Dirac mass. This is further corroborated by the diverging strain dependence of positive longitudinal magnetoconductance near the transition point, which is a more profound consequence of the vanishing of the Dirac mass. In this sense, our study not only represents a new approach to characterize topological phase transitions, but also demonstrates a method to precisely control phenomena associated with the chiral anomaly.

One defining signature that distinguishes STI from WTI is the existence of surface states on all crystal facets, which is not addressed in the current study. On the other hand, all of our transport data on $ZrTe_5$ present strong evidence of an *in-situ* strain-tuned topological phase transition in this material. We note that our experimental setup for applying strain is compatible with photoemission and scanning tunneling spectroscopy measurements. Future studies incorporating spectroscopic techniques capable of measuring surface states and band topology should be able to provide a comprehensive understanding of topological phase transitions.

CHAPTER 5 - ANOMALOUS HALL EFFECT IN ZRTE$_5$

AHE BACKGROUND

The motion of electrons inside a crystal lattice is in general governed by a complicated set of equations. Amazingly, a semiclassical approximation where quantum mechanical wave packets are treated as classical particles describes the motion of these quasiparticles[5] remarkably well. In this semiclassical approximation, the motion of these particles is described by a simple set of equations:

$$\dot{\vec{r_n}} = \frac{\partial \epsilon_{\mathrm{n}}(\vec{k})}{\hbar \vec{k}}$$

$$\hbar\dot{\vec{k}} = -e\vec{E} - e\dot{\vec{r}} \times \vec{B}$$

See, for example, Ref. (*65*) for a derivation of these equations. The complicated forces of the crystal lattice acting on the original electrons have been replaced by much simpler forces acting on the quasiparticles. The velocity is simply given by the energy dispersion relation and the change of momentum by the electric and magnetic fields. This semiclassical set of equations provides accurate predictions for many measured phenomena.

The above equations of motion are inadequate, however, if the energy bands contain Berry curvature. To include the effects of Berry curvature, the velocity equation is updated as follows (*66*):

$$\dot{\vec{r_n}} = \frac{\partial \epsilon_{\mathrm{n}}(\vec{k})}{\hbar \partial \vec{k}} - \frac{e}{\hbar}\vec{E} \times \vec{\Omega}_n(k)$$

Where Ω_n is the Berry curvature associated with the *n*^*th*^ band. This extra term in the velocity equation was initially termed the "anomalous velocity" contribution (*67*, *68*), and only after its initial discovery was it associated with the Berry curvature. The inclusion of this anomalous velocity term into the calculation of the Hall conductivity yields the following expression (*69*):

$$\sigma_{\alpha,\beta} = -\frac{e^2}{\hbar}\sum_n \int_{BZ} \frac{d\boldsymbol{k}}{(2\pi)^3} f_n(\boldsymbol{k})\Omega_{n,\alpha\beta}(\boldsymbol{k})$$

---

[5] I will drop the quasiparticle notation from here on out, and simply refer to the wave packet quasiparticle as a particle or charge carrier. It is understood this will really be referring to the motion of a wave packet quasiparticle.

Where Ω_n is the Berry-curvature of the n^{th} band and f_n is the Fermi-Dirac distribution. This formula for the Hall conductivity is strikingly similar to the 2D formula, with the key difference that integrating over partially filled bands does not yield quantized Chern numbers. Therefore, the intrinsic contribution from the Berry curvature to the 3D Hall conductivity can be thought of as an unquantized version of the quantum Hall effect.

It should be noted that the above formula for the Hall conductivity only takes into account intrinsic contributions to the velocity originating from the band structure. Extrinsic mechanisms such as side jump scattering or skew scattering can also contribute to the Hall conductivity. In these scattering processes, carriers interact with impurities via spin-orbit coupling and can lead to an anomalous current. Understanding which mechanism is responsible for any measured anomalous Hall signal can be a difficult task. Experimental evidence suggests that skew scattering mechanisms only dominate for metals with $\sigma_{xx} > 10^6\ \Omega^{-1} cm^{-1}$ (*70*).

Avoided band crossings, where a gap is formed in the band structure, can generate Berry curvature that can lead to an intrinsic anomalous Hall effect. Detailed calculations have been done on for bcc Fe (*69*), fcc Ni (*71*), and hcp Co that have shown that large Berry curvature is associated with such an avoided band crossing. The correlation between avoided band crossings and intrinsic Berry curvature appears more general than the Fe, Ni, and Co systems (*57*).

An alternative source of intrinsic Berry curvature is Weyl nodes. If present in a system, Weyl nodes can serve as sources or sinks of Berry curvature in the band structure. If Weyl nodes are responsible for an anomalous Hall effect in a material, the magnitude of the anomalous Hall conductivity is proportional to the separation of the Weyl nodes in k-space (*72*).

$ZrTe_5$ displays the potential for Berry curvature to be generated from either an avoided band crossing or the formation of Weyl nodes. The band structure near the Γ point hosts an avoided band crossing (Figure 4-1D). Additionally, in large magnetic fields Zeeman splitting can lead to the formation of Weyl nodes near this Γ point. The presence of these two mechanisms motivates a detailed study of the Hall conductivity in $ZrTe_5$, which we conduct in this chapter. Below, we present measurements that indicate that a significant anomalous Hall conductivity is present in $ZrTe_5$ in extremely low magnetic fields. We present $k \cdot p$ calculations that indicate that the source of this low-field anomalous Hall conductivity arises from Berry curvature associated with the avoided band crossing. The contents of the chapter below are currently available in Ref. (*69*)

AHE IN ZRTE5

The Hall effect arises when time reversal symmetry is broken by either intrinsic magnetism or an external magnetic field (*59*, *73*, *74*). The latter contribution dominates in non-magnetic materials, in which the angular dependence of the Hall effect is typically a smooth cosine function because only the out-of-plane projection of the field generates the in-plane transverse motion of electrons. Here, we report the observation of an abrupt switching of the Hall effect by field rotation in a non-magnetic material, $ZrTe_5$. The angular dependence of the Hall resistivity approaches a signum function, persisting down to an extremely low field of 0.03 T. By varying the carrier density of $ZrTe_5$ over three orders of magnitude, we show that this singular behavior is due to the anomalous Hall effect generated by the ultra-dilute massive Dirac carriers in the quantum limit of Pauli paramagnetism when the Zeeman energy exceeds the Fermi energy. Our results elucidate the origin of the anomalous Hall effect in $ZrTe_5$, arising owing to the spin-polarized massive Dirac electrons rather than the separation of Weyl nodes.

The transition metal pentatelluride $ZrTe_5$ presents a unique paradigm for three-dimensional (3D) topological materials. Early measurements revealed a Dirac-like bulk electronic structure with a Fermi velocity comparable to graphene (*36*, *75*). Unlike graphene, however, $ZrTe_5$ is not a topological semimetal because the band touching at the Dirac point is not explicitly protected by any crystal symmetry. Instead, the Dirac-like dispersion of $ZrTe_5$ emerges from its proximity to the phase boundary between strong and weak topological insulator phases. The magnitude of the Dirac point gap grows as the system is pushed further away from the topological phase boundary(*53*–*55*), endowing the band edge carriers with a mass term (*74*). Since the massive Dirac band is the only band crossing the Fermi level at low carrier density, $ZrTe_5$ serves as a model platform to explore the physics of relativistic quasiparticles in a 3D system.

The unusual electronic structure of $ZrTe_5$ has already enabled a series of striking discoveries, including the chiral magnetic effect (*76*), log-periodic oscillatio(*27*(*27*)(*25*), a 3D quantum Hall effect (*57*, *77*), and the anomalous Hall effect (AHE) (*57*). The observation of the AHE is particularly intriguing, given that $ZrTe_5$ is not an intrinsically magnetic material. The AHE has previously been argued to arise from Weyl crossings induced by the external magnetic field (*78*), in which a pair of Weyl nodes act as the source and sink of Berry flux (*77*, *79*). More recent measurements suggest that an alternative mechanism may instead be responsible, in which the large Berry curvature driving the AHE arises from an avoided crossing of the massive Dirac bands, without any Weyl node formation (*80*). Despite considerable prior experimental attention, the origin of the AHE in $ZrTe_5$ remains to be fully understood.

In this work, we present extensive measurements of the AHE in both bulk single crystals and exfoliated thin flakes of $ZrTe_5$. We find that the Hall conductivity of all samples can be precisely separated into two components, corresponding to the anomalous and orbital Hall contributions. The carrier density varies by over three orders of magnitude in our samples, enabling a quantitative analysis of the AHE as a function of doping. Our measurements unambiguously identify the spin-splitting of the massive Dirac bands as the origin of the AHE in $ZrTe_5$, and are incompatible with the formation of Weyl nodes. Furthermore, we show that $ZrTe_5$ enters a spin-polarized quantum limit state at extremely low magnetic field, giving rise to a singular angle dependence of Hall response reminiscent of a uniaxial ferromagnet.

$ZrTe_5$ has a van der Waals (vdW) layered structure with the Cmcm orthorhombic space group. Each layer consists of ZrTechains extending along the a-lattice direction, and the layers are stacked along the b-lattice direction (Figure 5-1a). For convenience we will adopt the coordination system, in which the x, y and z-axes correspond to the lattice a, c and b-axes respectively. Figure 5-1b-d show the field dependence of resistivity and conductivity tensors of bulk $ZrTe_5$. We see a cusp-like behavior in measurements of ρ_{xx} versus field (Figure 5-1b), saturating to a large magnetoresistance (~400%) at a relatively low field (0.2 T). The saturating behavior is consistent with the magnetoresistance of a single band system with a closed semi-classical orbit (*57*, *76*). ρ_{xy} exhibits a nonlinear field dependence, which has previously been interpreted in the context of either a two-band model (*57*, *77*) or the AHE (*22*). We obtain the field dependence of the longitudinal σ_{xx} (Figure 5-1c) and the Hall conductivity σ_{xy} (Figure 5-1c-d) by inverting the resistivity tensor (see methods, Figure 5-4). The Hall conductivity shows a dispersive resonant-like behavior, in which σ_{xy} rapidly reaches a peak value at a very low field (0.01 T) and decreases gradually afterwards. Such a field dependence of σ_{xy} corresponds to the single-band Drude orbital Hall conductivity

$$\sigma_{xy}^{orbital} = \frac{pe\mu^2 B}{1 + \mu^2 B^2}$$

where p is the carrier density and e is the electron charge. In this expression, $\sigma_{xy}^{orbital}$ displays a maximum at a peak field corresponding to $\mu B = 1$, providing a direct measure of the average mobility, μ. In systems with highly mobile carriers, such as the Dirac semimetal Cd_3As_2, the condition $\mu B = 1$ can be achieved at a very low field (*22*). The sharp peak of σ_{xy} at 0.01T in Fig. 1d indicates that the mobility of our sample is also extremely high. However, whereas the low-field behavior of σ_{xy} is well described by $\sigma_{xy}^{orbital}$, the high-field behavior shows a clear deviation. Instead of decaying to zero as expected from the expression for $\sigma_{xy}^{orbital}$, our measurements of σ_{xy} in ZrTe$_5$ saturate to a finite value in high field (see Figure 5-5 more samples and higher fields). This contrasts previous observations in Cd$_3$As$_2$, in which σ_{xy} exhibits the anticipated decay to zero at high field (*22*).

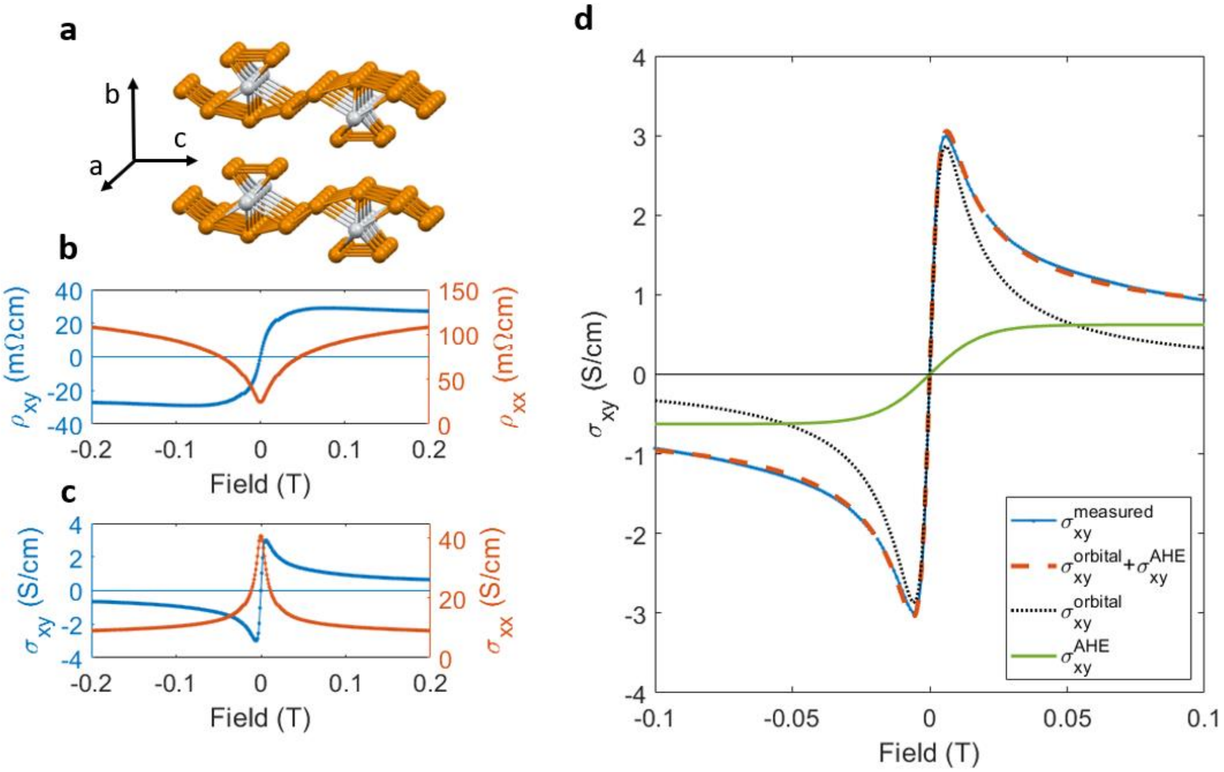

Figure 5-1: Anomalous Hall effect in ZrTe$_5$. (a) Crystal structure of ZrTe$_5$. Chains of tightly bound Zr atoms extend along the *a* lattice direction, forming sheets in the *ac* plane that are van der Waals coupled in the *b* lattice direction. (b) Resistivities ρ_{xx} and ρ_{xy} measured in a bulk crystal at 2K. (c) Conductivities σ_{xx} and σ_{xy} calculated from ρ_{xx} and ρ_{xy}. See Methods for details of the inversion of the resistivity tensor. (d) The Hall conductivity (solid blue) is decomposed into an orbital term $\sigma_{xy}^{orbital} = pq\mu^2/(1+\mu^2B^2)$ (dotted black) and an anomalous term fitted with a smooth activation function, $\sigma_{xy}^{AHE} = \sigma_0^{AHE}\tanh\,(B/B_0)$ (solid green). The total fit $\sigma_{xy}^{orbital} + \sigma_{xy}^{AHE}$ is shown in dashed orange.

We decompose our measured σ_{xy} in Figure 5-1d by fitting $\sigma_{xy} = \sigma_{xy}^{orbital} + \sigma_{xy}^{AHE}$ where $\sigma_{xy}^{AHE} = \sigma_0^{AHE}\tanh B/B_0$. The choice of a hyperbolic tangent function for the σ_{xy}^{AHE} component is purely phenomenological in order to capture the step function behavior, and the sharpness of the step function is characterized by the saturation field B_0. We find σ_{xy}^{AHE} saturates to $0.06\ \mathrm{S/cm}$ with a saturation field of $B_0 \sim 0.02$ T. The data cannot be fit by a two-band orbital model, ruling out this scenario (Figure 5-6). From the $\sigma_{xy}^{orbital}$ fit, we extract the carrier density, $p \sim 2.2 \times 10^{12}\ \mathrm{cm}^{-3}$, and average mobility, $\mu = 1.7 \times 10^{6}\ \mathrm{cm}^2/(\mathrm{V} \cdot \mathrm{s})$. This high mobility is comparable to the cleanest Dirac and Weyl semimetals previously investigated, including Cd_3As_2 (*81*) and TaAs (*82*).

CARRIER DENSITY DEPENDENCE

Having established the decomposition of σ_{xy} to the $\sigma_{xy}^{orbital}$ and σ_{xy}^{AHE} components, we now examine how each component varies as a function of carrier density. We utilize three methods to tune the carrier density of $ZrTe_5$ by more than three orders of magnitude (from $p \sim 9.8 \times 10^{12}\ \mathrm{cm}^{-3}$ to $p \sim 7.4 \times 10^{15}\ \mathrm{cm}^{-3}$). First, we purify the starting materials in the crystal growth process (see Methods for more details), which substantially reduces the carrier density. Second, we mechanically exfoliate bulk crystals down to flakes with thicknesses ranging from $105 - 350$ nm. The reduction of the sample thickness appears to increase the carrier density (*57*). Third, we utilize a parallel plate capacitor geometry to apply a back-gate voltage to the 105 nm thick exfoliated sample resting on a Si/SiO_2 wafer. Although gating a thick sample inevitably introduces a vertical potential gradient, we nevertheless observe a monotonic modulation of the carrier density, as determined from the fitting of $\sigma_{xy}^{orbital}$, and from a gate-dependent change in the resistivity. We are able to achieve a 50% change in the carrier density by applying 80 V to the Si back gate with a 285 nm capping layer of SiO_2 (Figure 5-7). Although the origin of this carrier density variation in thin flakes and the mechanism of gating are not fully understood, it offers a convenient tuning knob to tune the relative contribution of to $\sigma_{xy}^{orbital}$ and σ_{xy}^{AHE}. As we discuss below, these tuning capabilities are the key to understanding the origin of AHE.

For all the samples, σ_{xy} can be cleanly decomposed into $\sigma_{xy}^{orbital}$ and σ_{xy}^{AHE} according to the methodology shown in Figure 5-1d. Figure 5-2a shows the carrier density (p) and the mobility (μ) extracted from the $\sigma_{xy}^{orbital}$ component for all of our measured bulk single-crystals and exfoliated flakes. In Fig. 2b-c we present the saturation value σ_0^{AHE} and the saturation field B_0. All three quantities μ, σ_0^{AHE} and B_0 exhibit clear trends as a function of p. The mobility μ increases with reducing carrier density without any sign of a metal-insulator transition, characteristic of narrow or zero-gap semiconductors[20]. On the other hand, both σ_0^{AHE} and B_0 grow with carrier density, increasing from σ_0^{AHE} = 0.95 S/cm and B_0 = 0.01 T for the bulk crystal with the most dilute carriers (p =9.8 × 10^{12}) to σ_0^{AHE} = 34 S/cm and B_0 = 0.16 T for the 105nm thick exfoliated sample (p =7.4 × 10^{15} cm^{-3}).

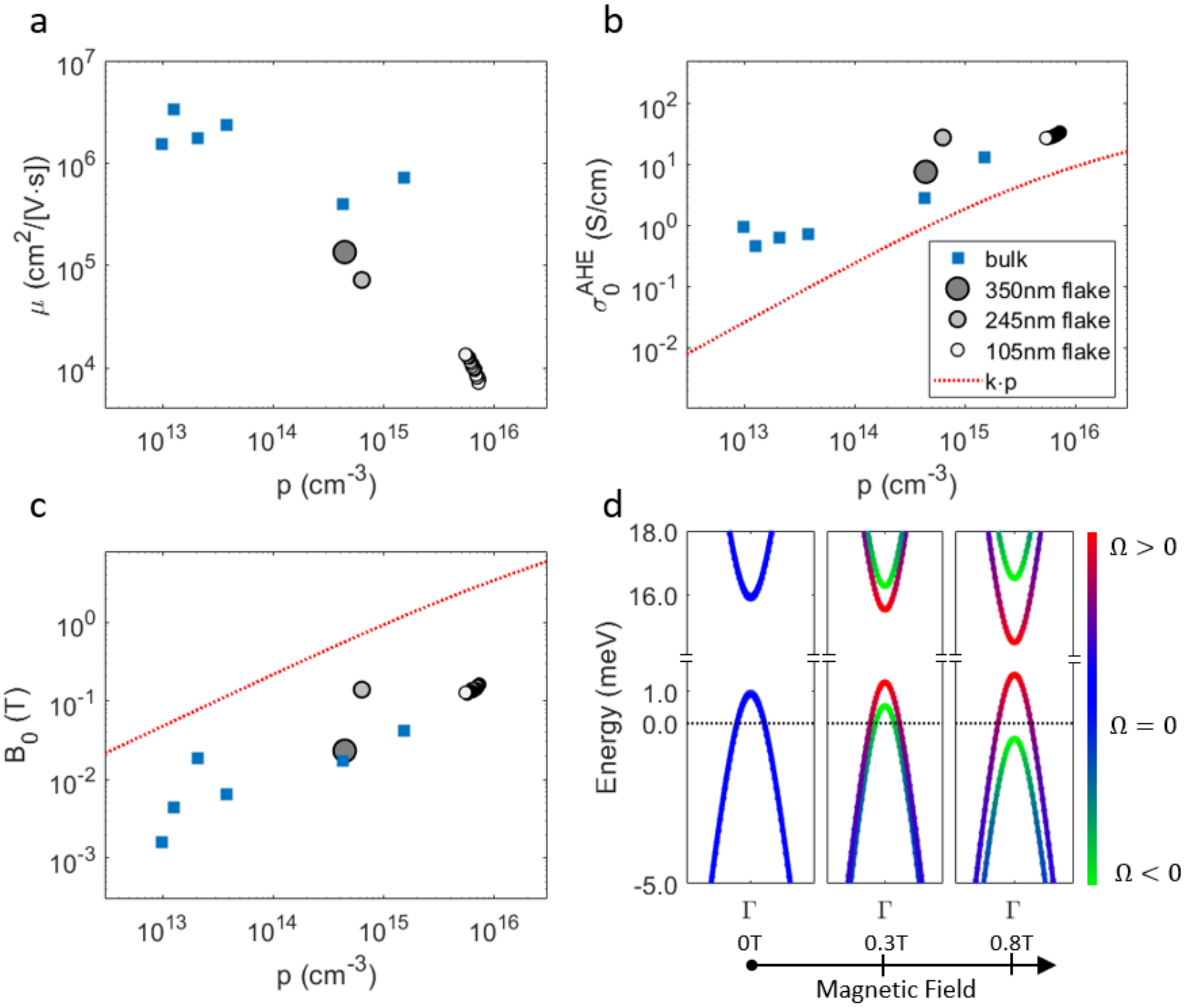

Figure 5-2: Doping dependence of the AHE in ZrTe$_5$. (a-c) Mobility (a), saturated anomalous Hall conductivity (b), and saturation field (c) plotted as a function of carrier density. The carrier density is extracted from the fitting procedure of σ_{xy} shown in Fig. 1. Blue squares indicate bulk samples. Black circles indicate exfoliated flakes with thicknesses 350 nm, 245 nm, and 105 nm. The 105 nm thick flake was additionally doped with a silicon back gate. The red dotted line in (b) corresponds to the magnitude of σ_0^{AHE} for a fully spin polarized band calculated using the $\boldsymbol{k} \cdot \boldsymbol{p}$ model. The red line in (c) corresponds the calculated magnetic field strength required to reach full spin polarization. (d) Band structure and Berry curvature of ZrTe$_5$ calculated using the $\boldsymbol{k} \cdot \boldsymbol{p}$ model. The Fermi energy corresponds to a carrier density of $5 \times 10^{14}\ cm^{-3}$. The green (red) color denotes the Berry curvature from spin up (down) electrons. The magnetic field is 0, 0.3 and 0.8 T from left to right. At 0.8 T the Zeeman splitting is large enough to fully spin polarize the

carriers for the indicated carrier density. $k \cdot p$ model calculations courtesy of Chong Wang and Di Xiao.

AHE MECHANISM – SPIN POLARIZED QUANTUM LIMIT

Currently, there are two competing explanations for the origin of the AHE in $ZrTe_5$. In one scenario, Weyl nodes form owing to an inversion of the valence and conduction bands in an external magnetic field (*55*). The AHE results from the finite Berry curvature of the Weyl nodes when the Zeeman splitting, E_Z, exceeds the energy gap, Δ. The AH conductivity grows continuously subsequent to Weyl node formation since it is proportional to their separation in momentum space, before eventually saturating at large B when the two Weyl points annihilate each other at the boundary of Brillouin zone. In the other scenario, $E_Z < \Delta$ and hence the valence and conduction bands stay well separated and Weyl nodes do not form. Although the massive Dirac bands are endowed with very large Berry curvature at the band edge, the net Berry curvature remains zero at $B = 0$ since time reversal symmetry (TRS) enforces a degeneracy between bands with opposite spin (and therefore opposite signs of the Berry curvature). However, the Zeeman splitting of the bands exposes a finite Berry curvature at the band extrema when TRS is broken by a magnetic field. The AHE onsets immediately upon lifting the spin degeneracy, and then saturates at the quantum limit when the E_Z exceeds the Fermi energy, E_F, after which all the electrons are spin-polarized. Figure 5-2d shows an illustration of this scenario.

These competing scenarios present distinct, experimentally testable predictions for the behavior of the AHE for magnetic fields aligned in various directions with respect to the principal crystal axes of $ZrTe_5$. For the purposes of this discussion, we take band structure parameters and g-factors previously reported for $ZrTe_5$, however the conclusions of our analysis do not depend on the exact values of these parameters. Assuming $\Delta = 10$ meV, $g_z = 21.3$, and a valence band bandwidth of 150 meV along the interlayer direction (*57*), we estimate that Weyl nodes form for $B > 8$ T, with a saturation field of $B_0 \sim 120$ T corresponding to their annihilation. This sharply contrasts with our experimental observations, in which we find that the anomalous Hall conductivity (AHC) is well described by a step function that onsets at extremely small $B > 0$, with a saturation field as low as 0.01 T in bulk crystals, and 0.17 T in the thinnest exfoliated crystals we measured.

In contrast, our observations match well with the predictions of the latter scenario, in which the AHE arises due to spin-split massive Dirac bands with large Berry curvature. We find that B_0 increases monotonically with p (Figure 5-2c), consistent with the expectation that larger B is required to reach the spin-polarized quantum limit ($E_Z > E_F$) since the chemical potential increases with doping (see schematics in Figure 5-2d). Furthermore, the monotonic increase of σ_{xy}^{AHE} with carrier density is consistent with the expectation that the Fermi surface encloses more Berry flux generated by the Dirac mass for larger E_F.

We calculate the intrinsic AHC using the previously reported $\boldsymbol{k} \cdot \boldsymbol{p}$ Hamiltonian of $ZrTe_5$ (Methods). The results reproduce all the qualitative features described above, including the saturation of the AHC when $E_Z > E_F$ (Figure 5-8), and the increase of the AHC with carrier density. We plot the calculated saturation field and the saturated AHC as a function of carrier density p (red dotted lines in Figure 5-2b-c). Although the calculated AHC depends on the specific band parameters for a given doping, the doping dependence of the AHC is robust against changes in these parameters and exhibits excellent agreement with our data. Our results reveal a striking picture of $ZrTe_5$: even without intrinsic magnetism, $ZrTe_5$ becomes a spin-polarized metal upon reaching the quantum limit of Pauli paramagnetism in a field as low as 0.01 T. Because of the ultra-high mobility, the orbital Hall effect is strongly suppressed at this weak field (peak field $\sigma_{xy}^{orbital}$ ~ 0.01 T), therefore the transverse conduction is dominated by the dissipationless AH current.

Finally, we turn to the angular dependence of the Hall effect, in which we rotate a constant magnetic field either within the *bc* or *ba* plane. As shown in Figure 5-3a-b, the magnitude of the Hall resistivity is nearly constant as a function of angle, but switches sign abruptly when the field rotates across the *ac* plane. This signum function angular dependence persists down to an extremely low magnetic field, below which the angular dependence returns to a smooth cosine function. We additionally find that this abrupt switching effect persists up to ~135 K for $B = 14$ T, as shown in Figure 5-3c for a representative bulk crystal. This corresponds approximately to the condition where $k_BT > E_Z$, providing additional evidence that spin-splitting of the massive Dirac valence band is required in order to see the abrupt switching of ρ_{xy}.

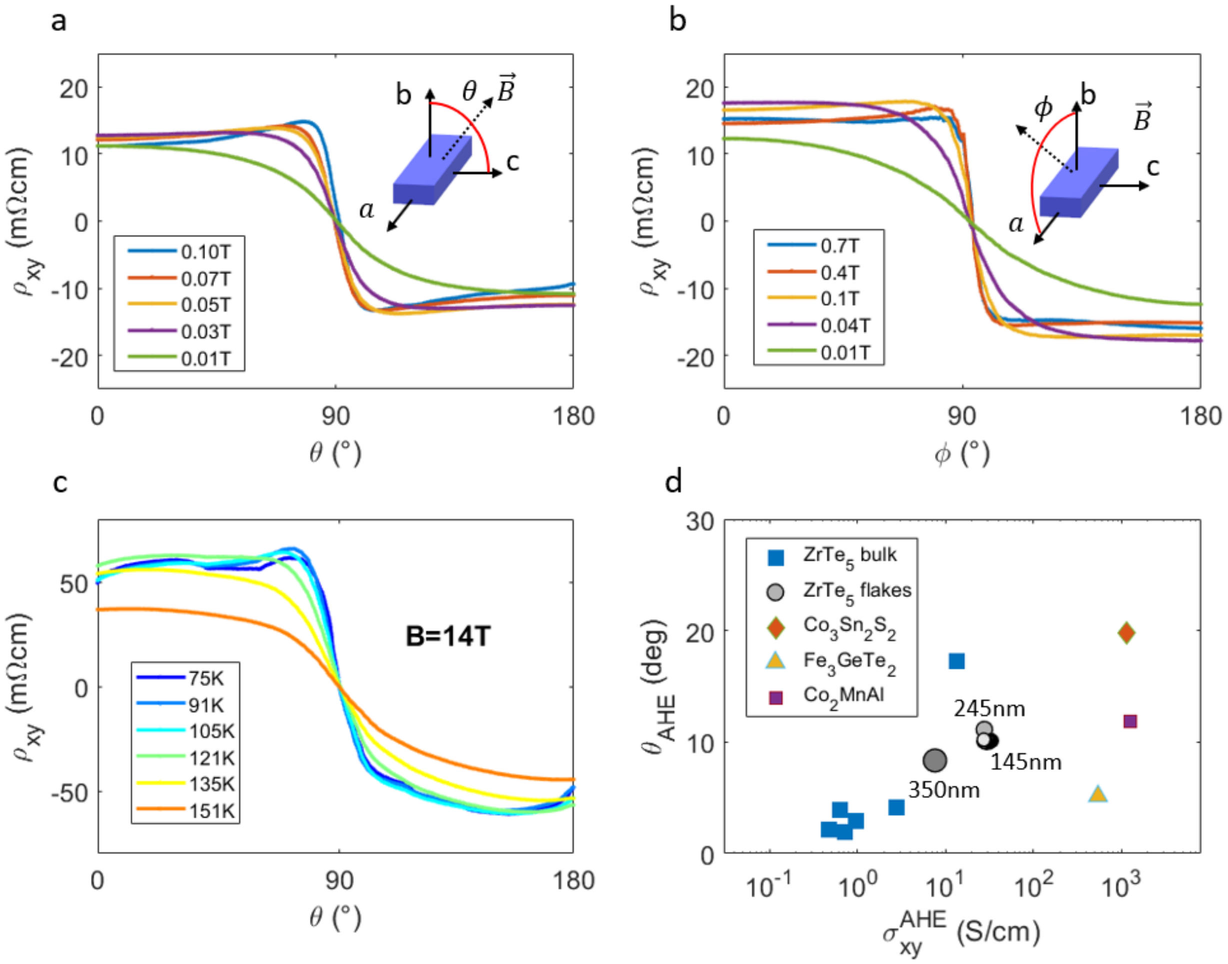

Figure 5-3: Angle dependence of the AHE in ZrTe$_5$. (a-b) ρ_{xy} measured at 2K at fixed field, measured as a function of magnetic field angle for a typical low-carrier density bulk crystal. The field is rotated in the *bc* plane in (a), and the *ac* plane in (b), as indicated schematically in the insets. For both orientations of the field, there is a sudden switching of ρ_{xy} as the field crosses the plane. (c) Temperature dependence of ρ_{xy} as the field is rotated across the *bc* plane. The field is fixed at 14 T. A strong deviation from cosine-like behavior is seen up to ~135 K. (d) The anomalous hall angle ($\theta_H^{AHE} = \tan^{-1}(\sigma_0^{AHE}/\sigma_{xx})$) for bulk ZrTe$_5$ (blue squares) and exfoliated flakes of ZrTe$_5$ (black circles). We find θ_H^{AHE} reaches up to 17.2° in the highest carrier density bulk crystal we measure. For comparison we also show θ_H^{AHE} for other magnetic topological semimetals.

Although previous work has also shown step-function dependence in the AH resistivity (*73*), this feature is only observed at fields above 1 T and additionally requires a background subtraction to eliminate the orbital Hall component. Here, we find that the raw ρ_{xy} exhibits this singular behavior at B > 0.03 T, enabled by our synthesis of ZrTe$_5$ samples with the most dilute carriers and highest mobility. Singular angle dependence of ρ_{xy} has previously been observed only in uniaxial ferromagnets, in which it arises from the abrupt reversal of the intrinsic magnetization. Owing to the combination of the large anisotropy of the g-factor of $ZrTe_5$ (21.3 along the b-axis versus ~2-3.2 in-plane (*79*)) and the ultra-low carrier density of our samples, a very small amount of out-of-plane field projection is sufficient to drive the system into the spin-polarized quantum limit. The resulting plateau of the AH conductivity as a function of angle can only be understood in this context, as magnetic field-induced Weyl node formation is not expected to result in such abrupt switching at very low field((*25*).

The AHE in $ZrTe_5$ is exceptional even in the broader context of magnetic materials. We calculate the anomalous Hall angle, $\theta_{AHE} = \tan^{-1}(\sigma_0^{AHE}/\sigma_{xx})$ for all the samples we measured and plot them against the AHC (Fig. 3d). We find that θ_{AHE} reaches a value of 17.2° as the carrier density increases, comparable to the magnetic topological semimetals with the largest θ_{AHE}[21-23], albeit with smaller AHC due to low carrier density. This large Hall angle is another signature of dissipationless nature of the anomalous Hall current. Intriguingly, for a high carrier density bulk sample the Hall angle, $\theta_H = \tan^{-1}(\rho_{xy}/\rho_{xx})$, reaches a value as large as 64° in fields as low as 0.04 T without any background subtraction of ρ_{xy} (Figure 5-9). This large Hall angle is likely a result of the combination of both anomalous Hall and orbital Hall effects, and it is approaching the 90° limit of the 3D quantum Hall effect that was also discovered in $ZrTe_5$ (*83*). Understanding how the AHE in the quantum limit of Pauli paramagnetism evolves towards the 3D QHE remains an open question for future study.

METHODS

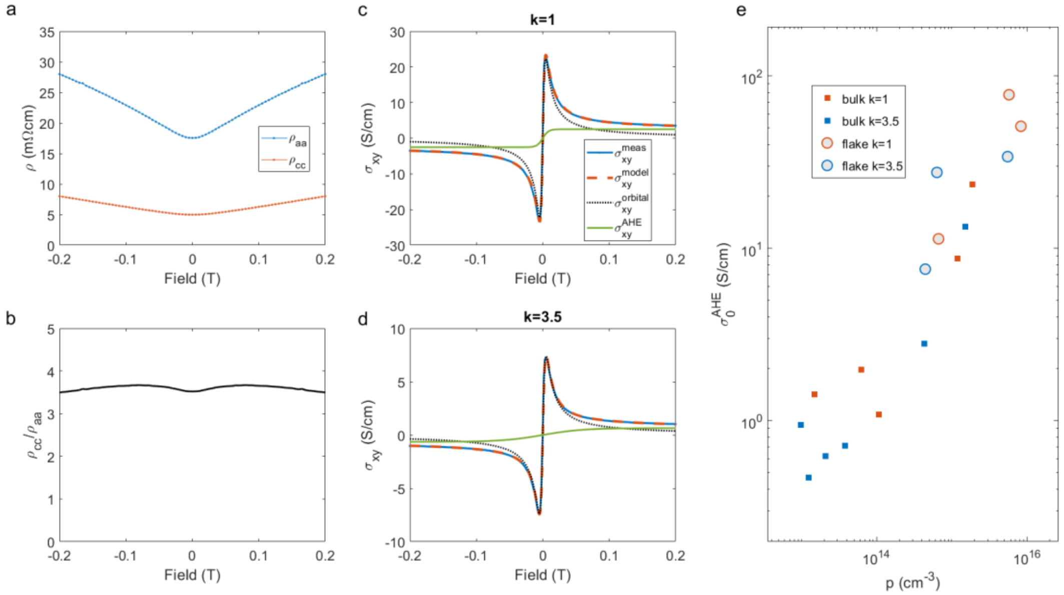

Figure 5-4: Inversion of the $ZrTe_5$ resistivity tensor. (a) ρ_{aa} (ρ_{xx}) and ρ_{cc} (ρ_{yy}) as a function of field at 2K. (b) The resistivity anisotropy ratio $k = \rho_{cc}/\rho_{aa}$ was found to be nearly constant, varying by less than 5% in the relevant field range used in our fitting. (c-d) Hall conductivity and its fitting based on the assumption of k=1 (c) and k=3.5 (d) when using the formula $\sigma_{xy} = \rho_{xy}/(\rho_{xy}^2 + \rho_{xx}\rho_{yy})$. The magnitude of the total and fitted anomalous Hall conductivities is reduced when k increases. (e) The relationship between σ_0^{AHE} and the carrier density p is relatively unchanged when using different values of k. Blue data indicates fitting results for k=1, and red data for k=3.5.

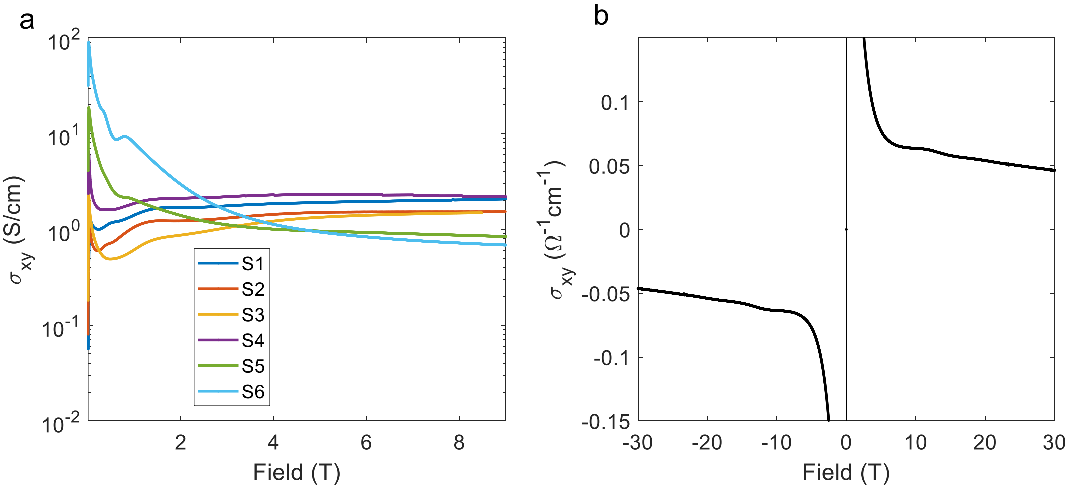

Figure 5-5: High field σ_{xy} behavior of $ZrTe_5$. Saturation of σ_{xy} at high fields. (a) Field dependence of σ_{xy} up to 9 T for all bulk samples measured in this work. (b) σ_{xy} of a representative sample measured up to 30T.

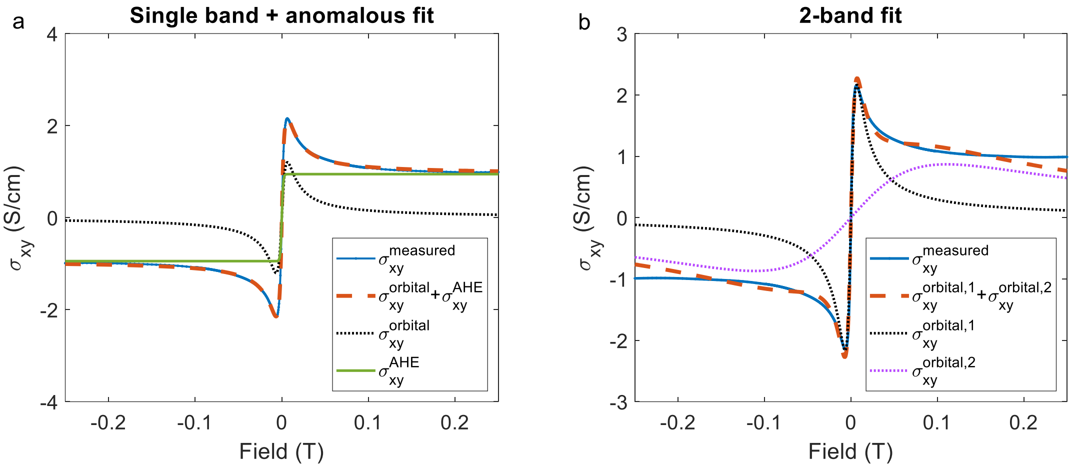

Figure 5-6: Inability of two-band model to describe σ_{xy}. Comparison of two fitting schemes. (Left) σ_{xy} fit with a single band orbital Hall effect and an anomalous Hall term. (Right) Fitting with a 2-band model without an anomalous Hall term.

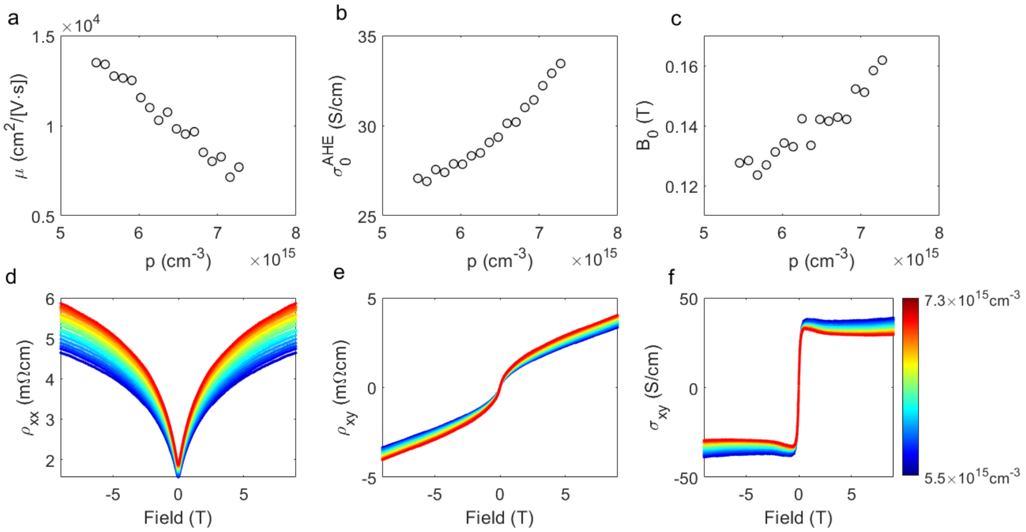

Figure 5-7: Gating dependence of σ_{xy} for a 105nm thick flake of $ZrTe_5$. (a-c) Fitting parameters from the $\sigma_{xy} = \sigma_{xy}^{orbital} + \sigma_{xy}^{AHE}$ model for the gated 105nm flake. (d-f) ρ_{xx}, ρ_{xy}, and σ_{xy} as a function of field for gating voltage setpoints. The color bar denotes the carrier density inferred from the $\sigma_{xy}^{orbital}$ fit.

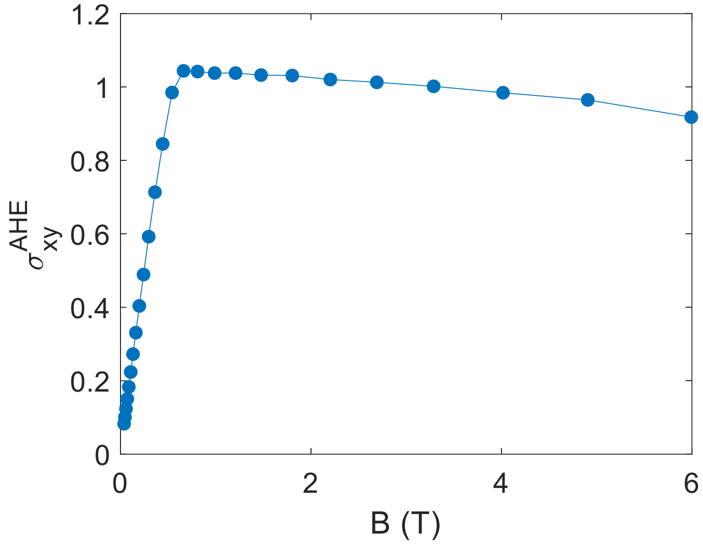

Figure 5-8: $k \cdot p$ model of σ_{xy}. σ_{xy} as a function of magnetic field calculated from the $k \cdot p$ model and assuming a g factor of 21.3 for a carrier density of $5 \times 10^{14} cm^{-3}$. $k \cdot p$ model calculations courtesy of Chong Wang and Di Xiao.

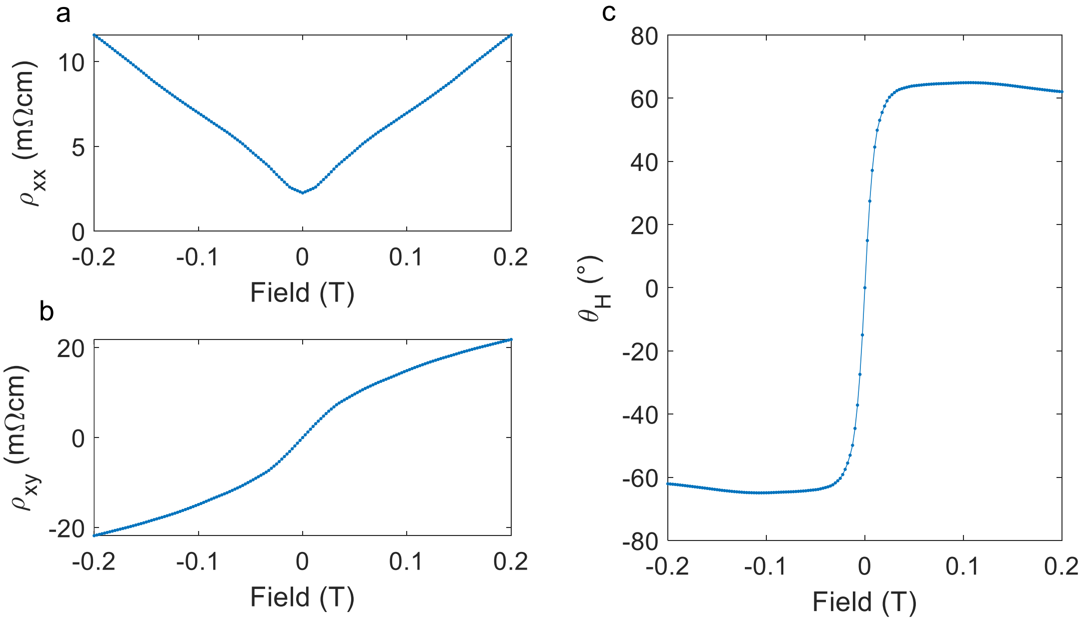

Figure 5-9: Large Hall angle in bulk ZrTe5. (a-b) ρ_{xx} and ρ_{xy} at 2K for a bulk crystal with the highest hall angle measured in this work. (c) The hall angle defined as $\theta_H = \tan^{-1}\left(\frac{\rho_{xy}}{\rho_{xx}}\right)$.

CHAPTER 6 - MAGIC ANGLE EFFECT IN ZRTE5

In this section I will discuss a “magic angle” effect in ZrTe5. The term “magic angle” originates to the Lebed magic angle effect that was predominately studied in the 1980s and 1990s in quasi-1D organic salts, and unrelated to the recent magic angle effect that has attracted recent attention in twisted bilayer devices. I will first review the most popular theory for the Lebed magic angle effect developed in the 1980s and 1990s, and we will see that this theory is incapable of explaining why a magic angle effect occurs in $ZrTe_5$. To arrive at a potential explanation for the mechanism of the effect in $ZrTe_5$, I will review some theoretical groundwork of magnetic Bloch bands (MBBs) and the 2D Hofstadter spectrum, then discuss how MBBs and a Hofstadter spectrum may arise in a 3D system such as $ZrTe_5$.

LEBED’S MAGIC ANGLES IN QUASI-1D MATERIALS

The Lebed magic angle effect, or simply the magic angle effect as I will refer to it in this text, occurs in quasi-1D conductors when the magnetic field is rotated in the direction perpendicular to the most conducting direction, as shown in Figure 6-1. The magnetoresistance of the crystal displays sharp dips at the magic angles. These angles correspond to when the magnetic field is commensurate with the lattice, where the field vector connect nearest or next-nearest neighbor lattice sites, shown in Figure 6-1c.

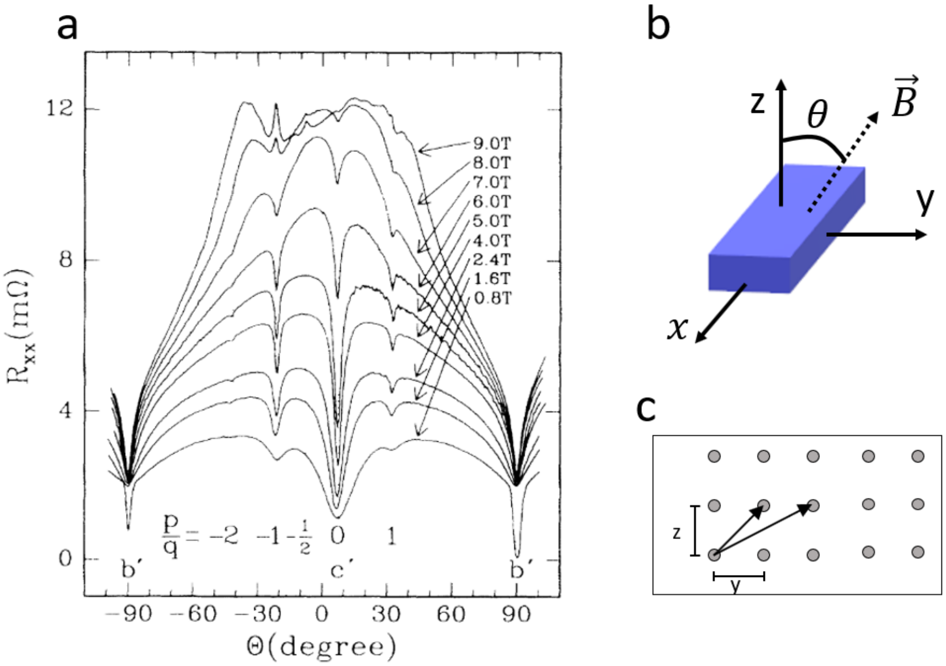

Figure 6-1: The magic angle effect in $(TMTSF)_2PF_6$. (a) The magnetic field is rotated in the plane perpendicular to the most conducting direction, shown on the right. Sharp dips in the resistance are seen when the field is commensurate with the crystal lattice. Data from Ref. (*84*, *85*). (b) Orientation of the field rotation in the y/z plane. (c) A cross section of the crystal lattice in the y/z plane is shown here. The gray circles correspond to lattice sites. The field is said to be commensurate with the lattice with the field vector connects nearest or next nearest neighbor lattice sites, shown by the arrows.

The sharp dips in the magnetoresistance for commensurate field orientations is quite striking. Typically, the angle dependent magnetoresistance is a smooth, cosine-like function of angle that reflects different in-plane and out-of-plane carrier mobilities. This magic angle effect was first measured in 1991 in the organic material $(TMTSF)_2ClO_4$ (*86*) although since then it has been measured in several other similar organic materials in the Bechgaard salt family (*86*). The materials in which the magic angle effect have been measured share a common feature of strong anisotropy, which results in a quasi-1D fermi surface of warped fermi sheets.

The quasi-1D warped fermi sheet is a consequence of the anisotropy of the system, and is easily visualized resulting from the following tight binding dispersion relation:

$$\epsilon(\vec{p}) = -2t_x \cos\left(\frac{p_x a_x}{\hbar}\right) - 2t_y \cos\left(\frac{p_y a_y}{\hbar}\right) - 2t_z \cos\left(\frac{p_z a_z}{\hbar}\right) - \epsilon_F$$

Here a_i is the lattice constants in the i^{th} coordinate, and t_i is the hopping parameter. In the case of strong anisotropy along one direction, $t_x \gg t_y \sim t_z$, the fermi surface will quickly reach the Brillouin zone boundaries in the *y* and *z* direction but not the *x* direction. The dispersion along the *x* direction can be approximated as a linear fit at the fermi level, and the dispersion relation becomes:

$$\epsilon(\vec{p}) = v_F(|p_x| - p_F) - 2t_y \cos\left(\frac{p_y a_y}{\hbar}\right) - 2t_z \cos\left(\frac{p_z a_z}{\hbar}\right)$$

Where v_F and p_F are the fermi velocity and momentum, respectively. This dispersion relation now describes a pair of warped fermi sheets, shown in Figure 6-2.

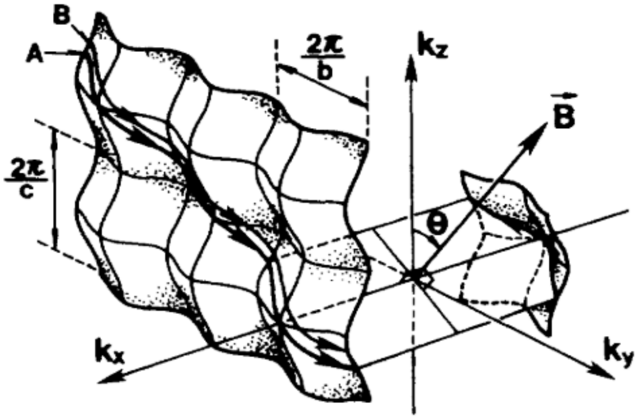

Figure 6-2: The fermi surface of a warped sheet. The sheet is open (reached the Brillouin zone boundary) along the *y* and *z* directions and closed along the highly conducting *x* direction. Two paths of particle motion are shown, marked path A and path B.

I follow the methodology of (*87*) to see how these fermi sheets are responsible for the magic angle effect. The basic phenomena that gives rise to the magic angle effect is from a resonant effect in the motion of charge carriers across these warped sheets. Consider a magnetic field perpendicular to the x direction, $\vec{B} = (0, B\sin\theta, B\cos\theta)$. Applying the standard semiclassical equation of motion, $\dot{\vec{p}} \propto \frac{1}{\hbar}\frac{\partial\epsilon}{\partial\vec{p}} \times \vec{B}$, we found that charge carriers pass through the Brillouin zone at a nearly constant speed. The frequencies of charge carriers traversing the Brillouin zone are:

$$\omega_y = \frac{a_y}{\hbar}\left|\frac{dp_y}{dt}\right| = \frac{ev_F a_y}{\hbar} B\cos\theta$$

and

$$\omega_y = \frac{a_y}{\hbar}\left|\frac{dp_y}{dt}\right| = \frac{ev_F a_y}{\hbar} B\cos\theta$$

For an arbitrary orientation of the magnetic field, these frequencies are incommensurate, and the motion is non-repeating. However, when the magnetic field is commensurate with the crystal lattice, these frequencies are commensurate, and the motion through momentum space (as well as real space) is repeating. This periodic repeating of motion is a resonance of sorts, and transport properties are sensitive to the resonance.

The first person to realize the significance of this resonance was Lebed, for whom the magic angle effect is named. Lebed realized the significance of this resonance before experimental measurement and predicted in 1985 that this resonance may create a susceptibility to a spin density wave formation (*88*). Lebed's original prediction, however, was that the resistivity should display spikes at the magic angles, whereas the experimental realization is that the resistivity displays dips at the magic angles. Furthermore, no experimental evidence confirms the formation of spin density waves at the magic angles. Despite this, Lebed's contribution realizing the significance of the resonant motion is significant.

Perhaps the simplest model that accurately describes the resistivity dips rather than spikes at the magic angles is given in (*88*). Here, the authors extend tight-binding dispersion relation to include contributions from next nearest neighbors as follows:

$$2t_y \cos\left(\frac{p_y a_y}{\hbar}\right) + 2t_z \cos\left(\frac{p_z a_z}{\hbar}\right) \rightarrow \sum_{m,n} t_{mn}[(mp_y a_y + np_z a_z)/\hbar]$$

Where t_{mn} is the hopping corresponding to $(0, ma_y, na_z)$. The solution to the Boltzman transport equation, solved in (*89*), predicts dips at commensurate angles of the magnetic field, similar to experimental results. A key feature of this model is that it requires the motion of carriers to traverse the entire Brillouin zone, meaning that an open fermi surface similar to the corrugated sheets of Figure 6-2 is still a necessary requirement to observe the magic angle effect.

A conceptually easy alternative explanation for the magic effect is given by a "hot spot" model, where certain locations of the fermi surface are prone to increased scattering (*86*). At incommensurate orientations of the magnetic field, non-periodic motion of charge carriers traverses the entire phase-space of the Brillouin zone, encountering these high-scattering hot spots and increasing resistivity. At commensurate orientations of the magnetic field, however, the periodic motion of the carriers can avoid these hot spots, leading to a decrease in the resistivity.

Like the previous model discussed, this hot spot model requires an open fermi surface. Although many other models have been proposed for the magic angle effect (*71*), an open fermi surface is always a necessary requirement. This is perhaps intuitive: in the momentum-space picture that describes carrier motion, lattice constants only enter the mathematics at the Brillouin zone edge, where they are used to define the boundary. Carrier motion that crosses this zone boundary can be more easily understood to display a dependence on lattice constants compared to motion on a closed fermi surface.

Therefore, the observation of the magic angle effect in $ZrTe_5$, which is presented below, presents a mystery as to the origin of the behavior. The fermi surface of $ZrTe_5$ is accepted to be an extremely small ellipsoid, well contained within a small fraction of the Brillouin zone. This closed nature of the fermi surface is at odds with previous models of the magic angle effect used to explain the phenomenon in the Bechgaard salts. Insight into the mechanism for the magic angle effect in $ZrTe_5$ may come from understanding carrier motion in strong magnetic fields, where the magnetic field is so strong that it can no longer be treated as a small perturbation to the periodic potential of the lattice. In this scenario, we describe the energy bands as magnetic Bloch bands rather than Bloch bands, which we discuss below.

MAGNETIC BLOCH BANDS AND THE HOFSTADTER BUTTERFLY

The challenge of describing single particle motion in a crystal lattice is a seemingly difficult problem but is made analytically solvable by simplifying the problem using the periodicity of the lattice through Bloch's theorem. Solutions to the Schrodinger equation form energy bands known as Bloch bands in crystal momentum space. Upon application of a magnetic field, a vector potential is introduced to the system through the Peierl's subsitution ($\vec{p} \to \vec{p} - e\vec{A}$) which destroys translational invariance by a single lattice vector. While small magnetic fields can be treated as a perturbation to the Bloch band solutions, the Schrodinger equation is more difficult to solve if the magnetic field strength is significant and unable to be treated as a perturbation. Below, I will follow the methodology of (*90, 91*) to highlight some unusual properties that arise when both the magnetic field and lattice potential are significant. The Hamiltonian we want to solve is:

$$H_0 = \frac{1}{2m}\left(-i\hbar\frac{\partial}{\partial\vec{r}} + e\overrightarrow{A_0}(r)\right)^2 + V(r)$$

While this Hamiltonian is no longer invariant under translations by an integer multiple of a lattice vector, we can define "magnetic translation operators" by which this Hamiltonian is invariant. These operators are defined as

$$T(\vec{r}) = \exp\left(\frac{ie}{\hbar}\int_0^{\vec{r}} d\vec{r}' \cdot \overrightarrow{A_0}(\vec{r} + \vec{r}')\right)\exp\left(\vec{r} \cdot \frac{\partial}{\partial\vec{r}}\right)$$

where $\vec{r}$ is the translation. Although the magnetic translation operator commutes with the Hamiltonian, magnetic translations along different crystal axis orthogonal to the magnetic field do not commute with each other unless there is an integer number of magnetic flux quantum ($\phi_0 = \frac{h}{e}$) enclosed in the area spanned by each translation operator. When this magnetic field requirement is reached, the Schrodinger equation can be solved, and the solutions are referred to as magnetic Bloch bands (MBB) rather than Bloch bands. The magnetic translation operators can themselves be integer multiples of the original lattice vectors. In this case, a new, "magnetic unit cell" that is

q times larger than the unit cell is formed, and MBBs form when the flux piercing this magnetic unit cell (Φ) is an integer multiple p times the flux quantum (ϕ_0). Succinctly, MBBs form when $\Phi = \frac{p}{q}\phi_0$, and correspond to an enlarged magnetic unit cell that is q times larger than the original unit cell.

The dependence of MBBs on the magnetic flux through a unit cell being a rational fraction of the magnetic flux quantum is peculiar. This is exactly the peculiarity that Douglass Hofstadter pointed out in his famous 1976 paper (*92*) in which he plotted the fractal-like energy spectrum of electrons in a 2D crystal lattice experiencing an out of plane magnetic field. Since increasingly large integer values for p and q lead to finer and finer details, the energy solutions exhibit a finely-detailed fractal-like spectrum. In reality, thermal and disorder blurring of the energy states can erase some of these details, but many features of the butterfly have been experimentally observed in recent years (*71*).

Moving away from the exact MBB solutions that occur for $\Phi = \frac{p}{q}\phi_0$, we can use the MBBs as an unperturbed basis and solve for the equations of motion for electrons in non-rational magnetic fields. The equations of motion are listed below, and exemplify some of the rich features of these states:

$$\dot{\vec{r}} = \frac{\partial E_n(\vec{k})}{\hbar \partial \vec{k}} - \dot{\vec{k}} \times \vec{\Omega}_n(\vec{k})$$

$$\dot{\vec{k}} = -e\vec{E} - e\dot{\vec{r}} \times \delta\vec{B}$$

The above equations are very similar for electron dynamics in a Bloch band perturbed by a small magnetic field, with the one exception that $\dot{\vec{r}} \times \vec{B}$ is replaced by $\dot{\vec{r}} \times \delta\vec{B}$, where $\delta\vec{B}$ is the deviation of the magnetic field from the magnetic field (B_0) associated with $\Phi = \frac{p}{q}\phi_0$ from which we build our perturbed model. The result is striking: MBBs at precise values of $\Phi = \frac{p}{q}\phi_0$ experience an effective magnetic field of zero, and only the difference from B_0 effects electron kinematics near these MBB states. Just as Bloch electrons perturbed by a weak magnetic field form cyclotron motion with radius proportional to the magnetic field, magnetic Bloch electrons can form so-called "hyperorbit" motion with radius proportional to δB.

Before continuing, it is worth pointing out the typical field scales that one might expect to see evidences of the Hofstadter spectrum and MBBs. For typical lattice parameters of $a{\sim}2$Å, it turns out that $\Phi = \phi_0$ corresponds to a huge magnetic field on the order of 10^5 T. This implies that for fields easily obtainable in modern laboratories (~10 T) the periodic potential associated with the magnetic field can be treated as a small perturbation of the periodic potential of the crystal lattice, and Bloch bands rather than MBBs are the basis states of solution to the Schrodinger equation inside a crystal lattice. In recent years, however, enlarged unit cells such as those of twister bi-layer graphene devices have drastically reduces this field scale, and evidence of MBBs have been seen in these devices (*93*).

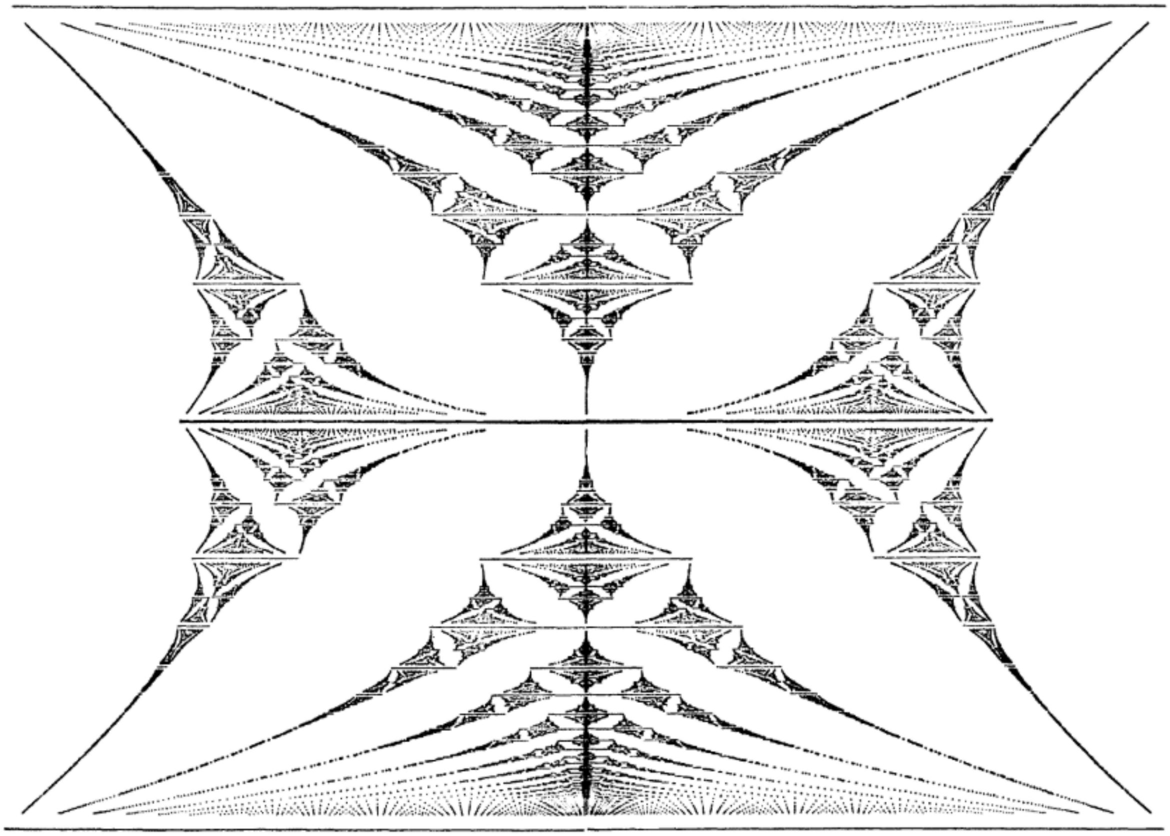

Figure 6-3: The Hofstadter butterfly. Energy (x axis, arbitrary units) plotted against alpha (y axis, ranging 0 to 1). Dark regions indicated allowed states, white regions indicated an energy gap. Figure taken from (*71*)

3D HOFSTADTER SPECTRUM

The previous discussion on the Hofstadter spectrum only considered the energy levels of electrons in the plane normal to the magnetic field. Dispersion of energy levels along the field direction would potentially wash out the Hofstadter spectrum, and Figure 6-3 is generally only considered for 2D systems. If a version of the Hofstadter spectrum exists in 3D, one might think that it is a remnant of the 2D spectrum that hasn't been washed out by the *z* axis dispersion. However, it turns out that there potentially exists a 3D version of the Hofstadter spectrum that is unique to 3D. To understand this, I will briefly review Koshino's derivation in (*71*) and review the Hamiltonian associated with the 2D Hofstadter butterfly, then show how a similar Hamiltonian can arise in 3D systems.

We start with a 2D tight binding Hamiltonian given by

$$H = \sum_{<i,j>} (t_{ij} e^{i\theta_{ij}} c_i^\dagger c_j + H.c.)$$

Where $\theta_{ij} = (e/\hbar) \int_i^j \vec{A} \cdot d\vec{l}$ is the Peierls phase. It we have a 2D system with an out of plane magnetic field, we can choose $A = (0, Bx)$ for our gauge and the wavefunction can be shown to be $\psi_{lm} = e^{ik_y m} F_l$, where *l* and *m* are integer positions corresponding to the lattice sites along the *x* and *y* directions. The Schrodinger equation then takes the form of what is known as Harper's equation,

$$-t_x(F_{l-1} + F_{l+1}) - 2t_y \cos\left(2\pi l + k_y\right) F_l = EF_l$$

In the isotropic case when the overlap integral along each direction is the same ($t_x = t_y$), this Harper's equation is the equation that Hofstadter studied in his 1976 paper and the Hofstadter spectrum emerges (*71*). To see how the Harper equation can arise in three dimensions, we consider the case of rotating a magnetic field in the *yz* plane. The magnetic field is given by $\vec{B} = (0, Bsin\theta, -Bcos\theta)$, and the vector potential can be chosen to be $\vec{A} = (0, Bxcos\theta, -Bxsin\theta)$. The Schrodinger equation is now $\psi_{lmn} = \exp\left(ik_y m + ik_z n\right) F_l$, where (*l*,*m*,*n*) label the lattice coordinates corresponding to (*x*,*y*,*z*). The Schrodinger equation is now:

$$-t_x(F_{l-1} + F_{l+1}) - \left[2t_y \cos\left(2\pi\phi_z l + k_y\right) + 2t_z \cos\left(-2\pi\phi_y l + k_z\right)\right] F_l = EF_l$$

This is substantially different than the Harper equation of the 2D system with an out of plane magnetic field. However, for the case of anisotropic hopping integrals, Koshino pointed out that the Harper equation can arises as an approximation to this 3D Schrodinger equation if $t_y \gg t_z$ and

$\phi_z > \phi_y$. In this case, bounds states form in the wells associated with the $t_y \cos(2\pi\phi_z l + k_y)$ term, and we can consider hopping between states in each well given by a hopping parameter t' and well number l'. The Schrodinger equation now becomes:

$$t'(J_{l'-1} + J_{l'+1}) - 2t_z \cos\left[-2\pi\left(\frac{\phi_y}{\phi_z}\right)l' + \left(\frac{\phi_y}{\phi_z}\right)k_y + k_z\right]J_{l'} = EJ_{l'}$$

Where J_l labels the wavefunction. This is now the Harper equation, and the Hofstadter spectrum now exists in three dimensions!

Of course, such a theoretical construct is subject to critical examination, especially since evidence for such a 3D Hofstadter spectrum has not been experimentally observed. We know that the 2D Hofstadter spectrum is only seen in huge magnetic fields (~10^5 T) unless the unit cell is enlarged through moiré superlattices. The first reality check as to whether this model is feasible is to consider the physical length of the hopping distance for carriers trapped in adjacent local minimums of the $2t_y \cos(2\pi\phi_z l + k_y)$ potential. For a field strength associated with ϕ_z, this means that two adjacent minimums are separated by a distance of $1/\phi_z$ lattice sites. In the table below, I use the lattice parameters of ZrTe5 to calculate the physical separation distance between adjacent wells in the $ZrTe_5$ model. For field strengths of 0.01T, the separation distance is over 100,000 nm, while for 100T the separation distance is 15 nm. If states bound in neighboring wells overlap and a non-zero hopping is present, the 3D Koshino-Hofstadter butterfly may form.

B (T)	ϕ_0/ϕ_z	$\frac{\phi_0}{\phi_z} \times a$ (nm)
0.01	3.7×10^5	1.5×10^5
0.1	3.7×10^4	1.5×10^4
1	3.7×10^3	1.5×10^3
10	3.7×10^2	1.5×10^2
100	3.7×10^1	1.5×10^1

Table 6-1: Separation between adjacent minimums in the Koshino model. The lattice parameters of $ZrTe_5$, $a \sim 0.4nm$ and $c \sim 1.4nm$, were used to calculate the flux through the unit cell associated with the magnetic field strength. The middle column corresponds to the number of lattice sites between adjacent minimums, and the right column to the physical length between them.

APPLICATION TO ZRTE5

Sharp, anomalous dips in the angular dependence of the magnetoresistance of $ZrTe_5$ single crystals are observed. These dips occur at fixed angles once the magnetic field passes the quantum limit and correspond to commensurate angles where the field direction connects neighboring lattice sites. This is reminiscent of the “magic angle” effect found in organic, quasi-1D materials. Unlike these previous materials, a quasi-1D open fermi surface is absent in bulk $ZrTe_5$ and is replaced with an ellipsoidal Fermi surface well contained within a small fraction of the Brillouin zone. We study the temperature dependence and sensitivity of the magic effect affect to perturbations such as doping and magnetic field misalignment. A possible 3D correlation to Brown-Zak oscillations and the 2D Hofstadter spectrum is discussed.

In the semiclassical picture of magnetotransport, electrons travel along constant energy contours on a plane perpendicular to the magnetic field in k-space. Therefore, anomalies in magnetoresistance (MR) are generally associated with geometric features in k-space. These features are determined by the band-structure and Fermi energy, and hence are only indirectly coupled to the crystal lattice. For example, the frequency of SdH oscillations is determined by the extremal area of the Fermi surface cross section (*19*), and angle dependent MR oscillations of quasi-2D systems are determined by the warping of Fermi surface cylinders (*88*, *94*).

There are only two occasions in solids where charge carriers directly sense the effect of the crystal lattice under magnetic fields. The first one is the so-called Lebed Magic Angle Effect (MAE) of quasi-1D organic materials (*83*, *95*). When a magnetic field is rotated about the axis defined by the 1D chain of these materials, sharp anomalies appear in both in-plane and interlayer resistance when the field is aligned along a commensurate angle, corresponding to the field connecting lattice sites that are neighbors or next-nearest neighbors.

The second case is observed in Morié superlattices formed by stacking monolayers of BN and graphene with a misalignment angle between the two layers (*92*). In this case the wavelength of the superlattice is long enough to become comparable to the magnetic length in moderate fields of just a few telsa. In addition to the well-known Hoftstadter butterfly, one notable obsrvation is the so-called Brown-Zak (BZ) oscillations (*96*). Here, Bloch states form when the magnetic flux through a unit cell of the superlattice is a rational fraction of the flux quantum, $\frac{\Phi}{\Phi_0} = \frac{p}{q}$, resulting in an anomalous spike of the conductivity at these rational values of the magnetic flux.

Here we report a third case: the observation of the MAE in single crystal $ZrTe_5$, where we observe sharp dips in the resistivity of $ZrTe_5$ at commensurate orientations of the magnetic field. The observation of the MAE in $ZrTe_5$ is significant because semiclassical theories of the MAE require an open fermi surface (*94*, *97*, *98*), a condition met by previous materials that displayed the MAE. However, $ZrTe_5$ has an extremely small, closed fermi surface well contained within a fraction of the Brillouin zone (*99*). The sensitivity of magnetotransport to the underlying crystal lattice suggests significant quantum mechanical effects which are not taken into consideration by the semiclassical model. Below, we examine the sensitivity of the MAE in $ZrTe_5$ to temperature, doping, and azimuthal misalignment of the magnetic field. We find that the azimuthal angle dependence of the MAE effect in $ZrTe_5$ suggests that the quasi-1D nature of $ZrTe_5$ plays an important role, suggesting a potential correlation to a 3D Hofstadter butterfly.

RESULTS

$ZrTe_5$ is a van der Waals layered material crystallized in the Cmcm orthorhombic space group, as shown in Figure 6-4. Each layer consists of $ZrTe_3$ chains extending along the a-lattice direction, and the layers are stacked along the b-lattice direction. The chains of $ZrTe_3$ are coupled in-plane by a zigzag chain of Te atoms. We grew $ZrTe_5$ by the chemical vapor transport (CVT) and flux growth methods. The flux method is known to produce crystals with fewer Te-vacancies compared to the CVT method (*27*). Figure 6-4A shows that the CVT-grown crystals display a resistivity maximum near 130K, consistent with previous reports and indicates a shifting fermi level as a function of temperature (*27*, *73*). For the flux-grown crystals, Figure 6-4B shows the resistivity peaks at the base temperature at 2K, which is consistent with previous reports on flux-grown crystals and indicates a very low carrier density (*27*).

We measured the angular magnetoresistance (AMR) for both the CVT-grown and flux-grown crystals with the current applied along the a lattice direction of the crystal and the magnetic field rotated in the *b*-*c* plane perpendicular to the current. For the CVT-grown crystal, the base temperature carrier density is around $n = 3 \times 10^{19} cm^{-3}$ and a strong AMR oscillation pattern is seen with maximums and minimums in the resistivity as the field is rotated, shown in Figure 6-4C. These extremums in the resistivity result from the magnetic field quantizing the k-space radius of electron orbits into distinct “Landau tubes”. When the radius of one of these tubes matches the extremal cross section of the fermi surface area perpendicular to the field, the conductivity displays a maximum. In this regard, the mechanism behind this AMR oscillation pattern is the same mechanism behind Shubnikov-de Haas (SdH) oscillations seen at a fixed angle as a function of increasing magnetic field, which has been studied previously in this system (*73*, *100*).

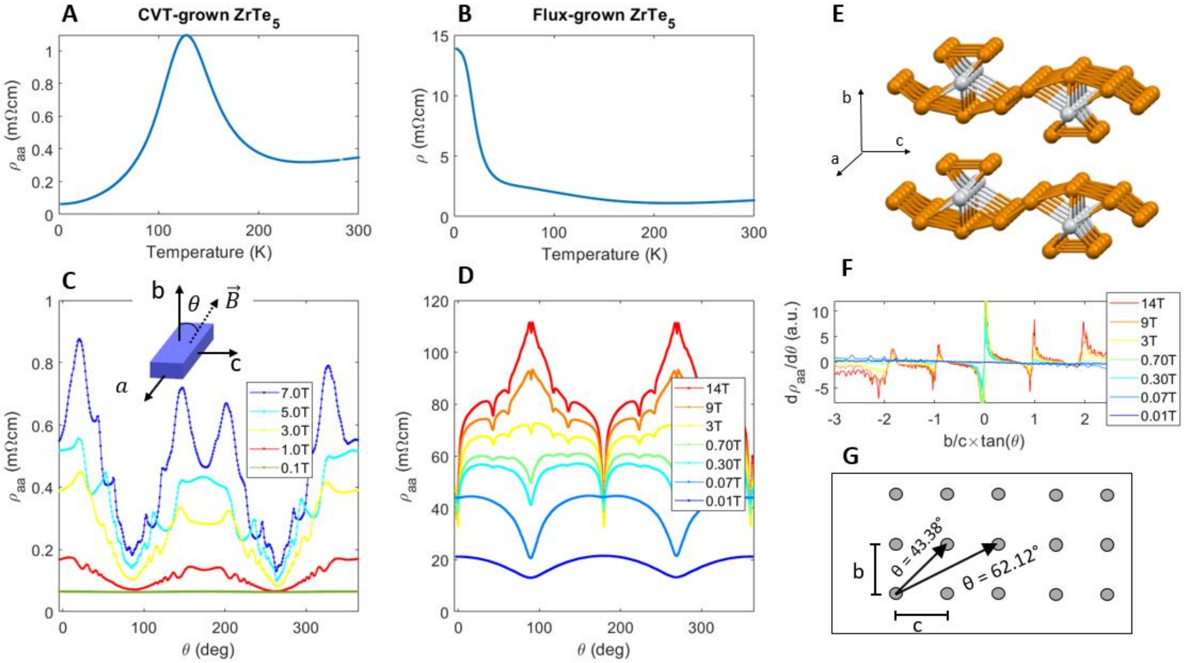

Figure 6-4: Magic angle effect in $ZrTe_5$ **(A-B)** Resistivity-temperature curves for CVT-grown (A) and flux-grown (B) single-crystals of ZrTe5. **(C-D)** Resistivity-angle curves for CVT-grown (C) and flux-grown (D) crystals. The different colors correspond to different field setpoints, and the field is rotated in the b-c plane as shown in the inset of C. **(E)** The crystal structure of $ZrTe_5$. Chains of $ZrTe_3$ are tightly bound along the *a* lattice direction, coupled in-plane by zig-zag Te atoms. Single layers of $ZrTe_5$ are van der Waals bonded in the *b* lattice direction. **(F)** The angular resistivity derivative $d\rho/d\theta$ of the flux-grown crystal plotted against $b/c\ \times tan\theta$. Integer values on the *x* axis correspond to when the field is commensurate with the lattice, as shown in the panel below. **(G)** The grey circles correspond to lattice sites in the b-c cross section of the crystal. The commensurate orientations $\theta = 43.38°$ and $\theta = 62.12°$ correspond to $\frac{b}{c} \times tan\theta = 1, 2$, respectively.

A key feature of the CVT AMR oscillation pattern is that the extremums in the resistivity do not occur at fixed angles but shift if the field setpoint is changed. This AMR oscillation pattern is qualitatively different from the AMR of the flux-grown crystal, which has a much lower carrier density of around $4 \times 10^{14} cm^{-3}$. Figure 6-4D shows that the AMR of the flux-grown crystal displays sharp dips in the resistivity that always occur at the same angles regardless of the field strength. These angles correspond to when the magnetic field is commensurate with the crystal lattice, as indicated in Figure 6-4. This is precisely the same effect as the Lebed Magic Angle effect measured in quasi 1D organic materials, despite $ZrTe_5$ not possessing an open fermi surface which has been attributed as the mechanism for this effect.

The low carrier concentration of the flux-grown crystals appears to be an important factor behind the origin of the MAE in $ZrTe_5$. To demonstrate this, we systematically grew several flux $ZrTe_5$ growths with varying purity of the starting materials. We were able to create a doping range between $10^{14} cm^{-3}$ and $10^{16} cm^{-3}$ for flux grown crystals, shown in Figure 6-5A. For all these crystals, we estimated the onset field (B_{onset}) at which the MAE emerges in $ZrTe_5$ (see Figure 6-5B-D). There is a strong correlation between the carrier density p and B_{onset}, with a scaling of approximately $B_{onset} \propto p^{\frac{2}{3}}$. This scaling suggests that the onset of the MAE is associated with the system entering the quantum limit, where all charge carriers reside in the lowest Landau level. This correlation is further corroborated by the data shown in Figure 6-5E-F, which presents AMRO data for a flux-grown crystal that displays both traces the conventional AMRO pattern as well as the sharp dips at fixed angles. The onset of the sharp dips begins only at high fields after the traditional AMRO pattern has ceased, confirming the MAE is associated with the system entering the quantum limit.

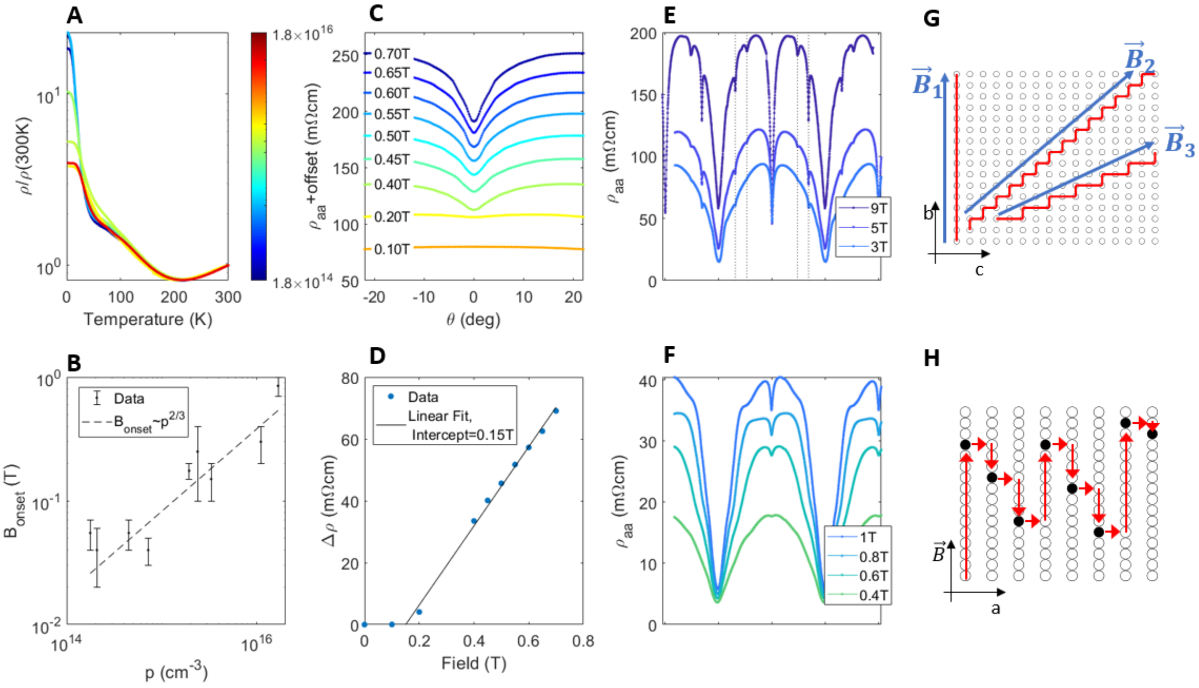

Figure 6-5: Onset behavior of the magic angle effect in $ZrTe_5$. **(A)** The resistance-temperature curve for several flux-growths of ZrTe5. Different purity of the starting materials leads to a variation of the carrier density p ranging from $p \sim 1.8\times10^{14}cm^{-3}$ to $p \sim 1.8\times10^{16}cm^{-3}$. The higher purity (lower carrier density) crystals display a higher base temperature resistance. **(B)** The onset field of the MAE, B_{onset}, is plotted against carrier density p for the same crystals shown in panel (A). B_{onset} is seen to approximately scale with $p^{2/3}$. **(C-D)** Characteristic data of the field onset of the MAE and the determination of B_{onset}. In (C), resistance-angle curves at different field setpoints show that the resistivity dip at 0° grows with increasing field for fields near the onset field. Data corresponding to different field setpoints have been plotted with different offsets to see this trend. In (D), the strength of this dip is plotted against field strength. The y-axis intercept of a linear extrapolation of the high-field data indicates the approximate onset field B_{onset}. **(E-F)** Resistivity-angle curves for a flux-grown crystal that displayed both conventional AMRO (F) and the MAE (E). In (F), conventional AMRO is seen as a single hump in the dataset that shifts with a changing field setpoint. In (E), the MAE is seen to emerge at 43° and 62° only in high fields, once the traditional AMRO oscillation has ceased. **(G)** White circles represent lattice sites in the b-c plane. Commensurate field orientations are shown by the vectors $\vec{B}_{1,2,3}$. Paths of charge carrier drift parallel to the field are indicated by the red lines. **(H)** The vertical axis here is defined by one of the commensurate field orientations of panel (G). The *x* axis corresponds to the crystal *a* axis. Here we indicate how delocalization along the field direction allows carriers to propagate forward, perpendicular to the field. Impurity sites (black circles) create scattering events that allow the charge carriers to hop forward. Only because the carriers are delocalized along the field direction do they have an increased probability of encountering an impurity site and completing the hopping process.

DISCUSSION

A simple model can be constructed that explains why a resistivity dip occurs once the system enters the quantum limit. When electrons are in the quantum limit, they are confined to a 1D tube (a Landau tube) defined by the field direction. Only when the field is aligned commensurate with the lattice do the electrons in this Landau tube experience a periodic potential. At these commensurate orientations, electrons can drift parallel to the field in Landau tubes (Figure 6-5G), and conduction perpendicular to the field is achieved through hopping between tubes via scattering events (Figure 6-5H). The periodic potential of the field + lattice system allows electrons to delocalize along the Landau tubes, increasing the likelihood of experiencing a scattering event and completing a hopping process which increases conductance (decreases resistance).

In principle, the picture of electrons drifting along Landau tubes should only be applied when the field is commensurate with a lattice direction. Arbitrary misalignments of the magnetic field along any lattice direction should destroy this commensurability. However, we performed a complete two-axis rotation (Figure 6-6) and discovered that the MAE in ZrTe5 is only sensitive to the field commensurate with the lattice in the *b*-*c* plane, and insensitive to misalignments along the *a* lattice direction. This insensitivity to azimuthal magnetic fields indicates a symmetry breaking effect, since rotating the field along the *b*-*c* plane yields qualitatively different results than rotating the field along the *a*-*c* or *a*-*b* plane. The broken symmetry is consistent with a quasi-1D nature of the electronic states, which is consistent with previous reports on $ZrTe_5$ indicating the hopping parameter along the *a* axis direction is much larger than hopping along the *c* or *b* lattice directions. Intriguingly, it has been predicted that a 3D Hofstadter Butterfly can be realized by rotating magnetic fields across a quasi-1D lattice (*93*, *101*). Analogous to the 2D butterfly, the rotation angle of a fixed field in a 3D lattice plays the role of the field strength in 2D. The key insight drawn from this analogy is that the 2D butterfly is a consequence of interference between the underlying lattice and the magnetic length, whereas the 3D butterfly is due to interference between the crystal lattice, magnetic flux through the *a*-*b* plane, and magnetic flux through the *a*-*c* plane. Therefore, commensurate angles in 3D match the commensurate flux filling of 2D, which exactly matches the resistance dip of Brown-Zak oscillations in 2D. Additionally, the 3D Hofstadter Butterfly has been predicted to be insensitive to azimuthal misalignments, in agreement with the measured insensitivity of $ZrTe_5$.

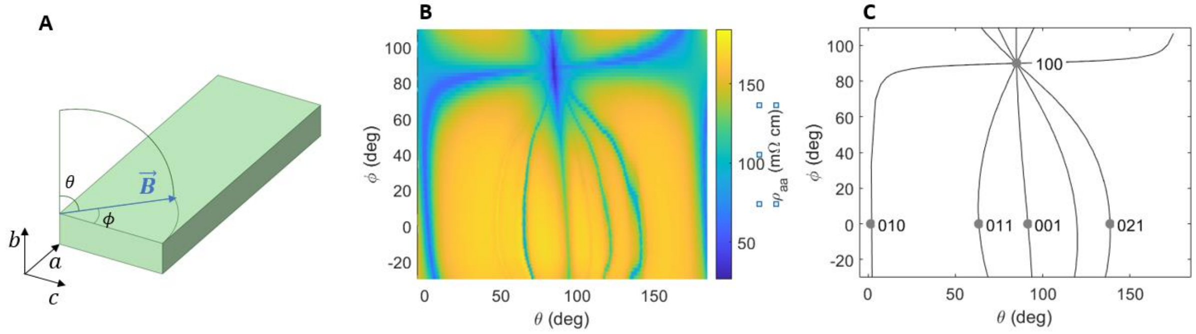

Figure 6-6: 2-axis rotation of $ZrTe_5$. **(A)** Schematic of the 2-axis rotations. At zero azimuthal angle ($\phi = 0°$), θ corresponds to the angle in the b-c plane. At $\phi = 90°$, θ corresponds to the angle in the b-a plane. **(B)** Resistivity (color) as a function of θ (x axis) and ϕ (y axis). This data was collected at a temperature of 2K and a field of 9T. Several sharp dips can be seen, indicated by the blue color. **(C)** High symmetry orientations of the field are marked by large gray circles and their miller indices are noted. The black lines correspond to partial commensurate orientations of the field where the field is commensurate in the b-c plane but not necessarily commensurate along the a lattice direction, e.g. the projections of the field along the b and c directions are a constant ratio: $B_b/B_c = p/q$, where p and q are simple integers. The exact curvature of these lines takes into account a misalignment of about 1.5° between the sample and the sample stage of the 2-axis rotator.

Since the 3D butterfly is created by rotating a fixed field, in principle it can be seen in an arbitrarily small magnetic field. In practice, a charge carrier's mean free path is finite, therefore carriers can only "sense" the butterfly effect when the periodicity of the magnetic potential ($\frac{\phi_0}{\phi}a$) is smaller than the mean free path. In Figure 6-7F, we compare B_{onset} with 1/μ, where the average mobility μ is estimated by fitting $\frac{\Delta\rho}{\rho} \sim \mu^2 B^2$ to the low-field magnetoresistance. At temperatures well above the resistivity maximum in ZrTe5 transport is dominated by a single band (*27*), and in this temperature range B_{onset} and 1/μ track exceedingly well, indicating $\frac{\phi_0}{\phi}a \sim l_{MFP}$ since the periodicity of the magnetic potential varies inversely with B. Intriguingly, in Figure 6-7E we compare B_{onset} with the carrier density, p, and find that $B_{onset} \sim \frac{\hbar}{e} p^{2/3}$ over a wide range of temperatures, consistent with the requirement that the system enter the quantum limit for the onset of the MAE (*102*).

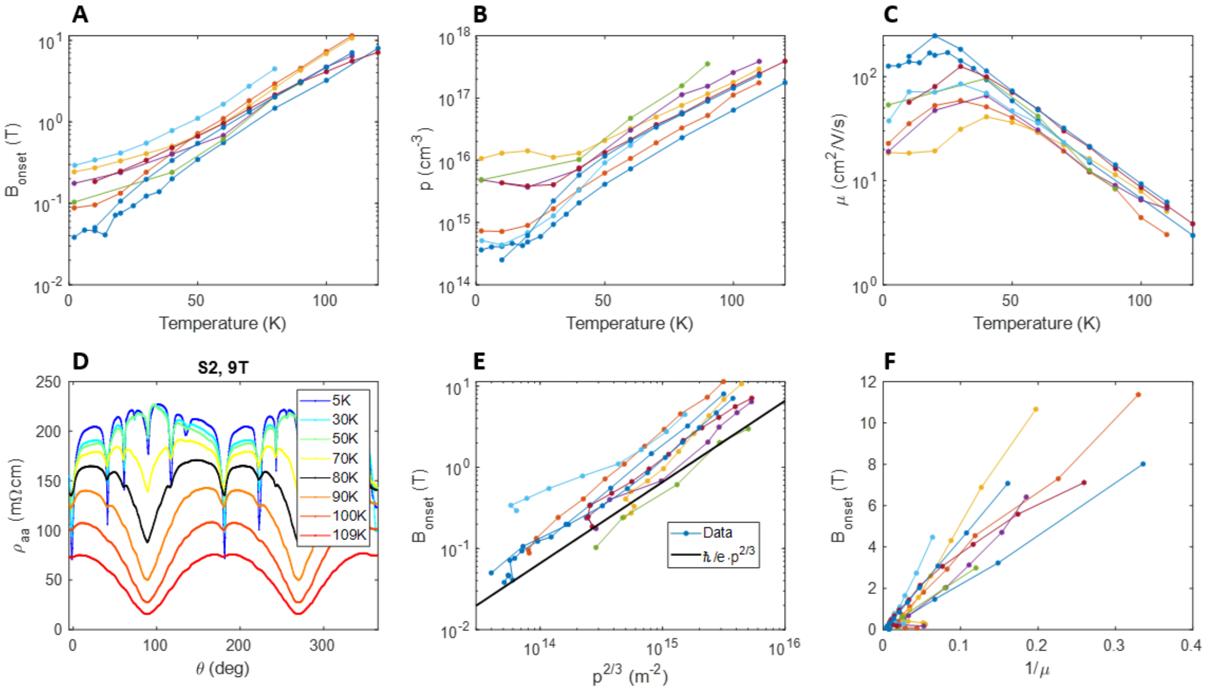

Figure 6-7: Temperature dependence of the MAE in ZrTe$_5$ **(A-C)** The onset field of the MAE (A), carrier density (B), and mobility (C) measured as a function of temperature. Each color denotes a measurement on a separate crystal. **(D)** Resistivity-angle curves at a constant field of 9T at different temperature setpoints. As temperature is increased, the MAE is seen to wash out. **(E)** B_{onset} is plotted against $p^{2/3}$. The field associated with the system entering the quantum limit, $\frac{\hbar}{e}p^{\frac{2}{3}}$, is plotted in the solid black line. **(F)** B_{onset} is plotted against inverse average mobility estimated from the low-field magnetoresistance, $\Delta\rho/\rho = \mu^2 B^2$. For temperatures above ~30K, B_{onset} scales linearly with $1/\mu$.

In conclusion, the observation of the MAE in ZrTe$_5$ cannot be explained by previous semiclassical theories for the MAE, which require an open fermi surface which is not present in ZrTe$_5$. We have proposed a simple delocalization model where drifting parallel to the magnetic field enables quasi-1D states to escape impurity localization. This simple model is consistent with a more general energy spectrum associated with a 3D analogy to the famous 2D Hofstadter butterfly. In the 3D Hofstadter butterfly, strong competition between the periodicity of the potentials of the magnetic field and the crystal lattice creates a fractal energy spectrum where delocalized states occur at commensurate angles. Although direct evidence for the 3D Hofstadter spectrum is lacking, the existence of the transport phenomenon (resistivity dips at commensurate angles) at remarkably low magnetic fields is shocking, indicating magnetic fields introduce significant effects that are not necessarily a small perturbation. Further theoretical and experimental work examining the connection to the 3D Hofstadter butterfly would be interesting.

CHAPTER 7 – SUMMARY AND OUTLOOK

To conclude, $ZrTe_5$ presents an ideal paradigm to study topological features associated with the STI, DSM, and WTI topological phases. The simplicity of the band structure allows for transport measurements to be sensitive to only the topologically nontrivial bands at the Γ point, with little to no interference from trivial secondary bands. It is because of this simplicity of the band structure that evidence for the strain-tuned topological phase transition of Chapter 4 and the anomalous Hall contribution of Chapter 5 is so clearly evident from bulk transport measurements alone.

The motivation to study $ZrTe_5$ is further accentuated by the ability to fabricate bulk samples with ultra-low carrier densities as low as $p{\sim}10^{14}cm^{-3}$. Reducing the carrier density to these extremely low levels tunes the Fermi energy to close to the charge neutrality point and allows electrical transport measurements to be governed by the low-energy physics at energy scales close to the band edge. Additionally, such low carrier densities allows accessing the quantum limit, where all charge carriers reside in the lowest Landau level, at very low magnetic fields.

Finally, the ultra-high mobility ($\mu > \frac{10^6 cm^2}{V \cdot s}$) that persists even at ultra-low carrier densities is another unique feature. While a few other topological materials with such high mobility exist, such as Cd_2As_2 or TaAs, such a high mobility is still relatively rare. It is perhaps because of this ultra-high mobility that features such as the magic angle effect of Chapter 6 exist.

With such an ideal paradigm of a material, there is still much work that can be done. For example, the negative longitudinal magnetoresistance when the magnetic field is parallel to the current is somewhat controversial. In Chapter 4, we saw different qualitative behavior of this effect and attributed it to evidence of a phase transition, probably related the chiral anomaly. It has been pointed out the current jetting could be a trivial explanation for the negative magnetoresistance. While it is improbably that current jetting would explain the qualitative different behavior across the phase transition, fully quantifying and understanding the physics of this behavior would be an interesting project. Some unpublished 2-point resistivity measurements I've taken seem to exclude the current jetting effect, although this project could be more fleshed out.

Other future work involves using the tool of the strain-tuned topological phase transition to understand how the topological phases are related to the anomalous Hall effect, magic angle effect, or even the log(B) oscillations. While I have some preliminary measurements for each of these projects, fully quantifying and understanding these results is a difficult challenge.

Finally, it remains an outstanding challenge to isolate a monolayer of $ZrTe_5$ and search for evidence of the quantum spin Hall state in 2D. $ZrTe_5$ proves to be a challenge to exfoliate to such a thin layer – below ~10nm thick it oxidizes in atmosphere, so working in a glove box is essential. Additionally, simple exfoliation techniques have never yielded samples below ~4-5 nm thick, and thin samples are difficult to lift off of a silicon substrate if transferring is needed.

A natural project to pursue is to more closely examine $HfTe_5$. $HfTe_5$ is also predicted to be a quantum spin Hall insulator in monolayer form, and close to the same STI-WTI phase transition in 3D. $HfTe_5$ is also almost as easy to fabricate with the flux technique as $ZrTe_5$, although the ideal flux ratio I've discovered is lower, typically ~1:40-1:80 work well. There are, however, advantages and disadvantages with the $HfTe_5$ growth. The disadvantages are that it is more difficult to effectively remove the Te flux from the $HfTe_5$ crystals – after centrifuging the crystals are speckled with Te flux. Additionally, it is difficult to obtain pure starting Hf material. Arc-melting the starting Zr material proved to be essential to developing high purity $ZrTe_5$ crystals. Hf tends to be commercially available in powder form, which has more impurities to begin with and is impossible to effectively purify through arc melting. However, with a longer lead time (several months) pellets of hafnium can be commercially obtained to arc melt and purify. The main advantage to the hafnium growth is that the $HfTe_5$ crystals tend to grow much larger than the $ZrTe_5$ crystals. The small crystal size presents experimental challenges to effectively measure the Hall conductivity or resistivity anisotropy.

In conclusion, the non-trivial topology and simplistic band structure of $ZrTe_5$ make it an ideal material to study. The ability to easily fabricate ultra-high purity crystals and rich spectrum of unique transport phenomenon motivates further intense experimental study.

CHAPTER 8 – APPENDICES

The solution to Boltzmann transport equations shows that thermopower is sensitive to the energy states immediately above or below E_F, while electrical conductivity is most sensitive to the energy states directly at E_F (*103*). This sensitivity to different portions of the electronic density of states highlights the fact that thermopower measurements can provide a complementary measurement to electrical conductance measurements. For example, thermopower measurements probe the mismatch in the density of states above and below E_F, which results in the sign of the Seebeck coefficient determining the sign of the majority carriers for doped semiconductors. The ability for thermopower measurements to predict carrier sign without relying on a magnetic field (such as Hall effect measurements) displays the power and complementary nature of thermopower measurements.

The power of thermopower as a probe into the underlying physics of a system is demonstrated by several recent measurements or predictions of unique thermopower behavior that arises from the topological state of a material. For example, the thermopower of Dirac and Weyl semimetals is predicted to increase without saturating in a magnetic field, with potential useful applications in thermoelectrics (*104*). In ZrTe5, the thermoelectric hall conductivity displays a robust plateau in the extreme quantum limit that is independent of carrier density and field strength, which is attributed to its Dirac semimetal spectrum (*105*). Anomalously large (*106*) and unconventional (*107*) Nernst effects have also been reported for Dirac and Weyl semimetals, respectively.

Due to the richness of the thermopower probe, a systematic study of the thermoelectric properties of ZrTe5 as a function of strain would be highly interesting, due to the ability of strain to tune the topological phase of ZrTe5 (see Chapter 4). Such a study would be able to study how these thermoelectric phenomena vary as the system is tuned through the STI, DSM, and WTI phases. In Appendix 1, the groundwork for such a project is developed by designing astrain-controllable thermopower measurement apparatus, where $BaFe_2As_2$ is measured as a test material. In Appendix 2, the novelty and power of thermoelectric measurements is further explored in anisotropy thermopower measurements of TaIrTe4, which displays n-type behavior in one direction and p-type behavior in another direction, so-called $p \times n$ behavior.

APPENDIX 1 – STRAIN TUNED SEEBECK COEFFICIENT

We present the design and construction of an apparatus that measures the Seebeck coefficient of single crystals under in-situ tunable strain at cryogenic temperatures. A home-built three piezostack apparatus applies uni-axial stress to a single crystalline sample and modulates anisotropic strain up to 0.7%. An alternating heater system and cernox sensor thermometry measures the Seebeck coefficient along the uniaxial stress direction. To demonstrate the efficacy of this apparatus, we applied uniaxial stress to detwin single crystals of $BaFe_2As_2$ in the orthorhombic phase. The obtained Seebeck coefficient anisotropy is in good agreement with previous measurements using a mechanical clamp.

INTRODUCTION

The Seebeck coefficient is the ratio of the voltage difference to the temperature difference in a material:

$$S = -\frac{\Delta V}{\Delta T}$$

Measurements of the Seebeck coefficient provide a uniquely different and complementary probe compared to resistivity measurements, in part because of its sensitivity to particle-hole asymmetry (*103*). For example, it is often used to determine if a semiconductor is p-type or n-type simply by the sign of the coefficient. While this direct correlation between the sign of the Seebeck coefficient and carrier type doesn't hold for all metals, (e.g., the noble metals), the sign, magnitude and anisotropy of Seebeck coefficient provide strong constraint to the theory of strongly correlated materials. Nernst and thermopower measurements have been a useful tool in probing the broken symmetries of both copper and iron based superconductors, in some cases providing a much more sensitive probe to the broken symmetry compared to resistivity measurements (*108*, *109*). Additionally, searching for materials with a large Seebeck coefficient is an active area of research due to applications in power generation, thermometry, and electronic refrigeration (*110*–*112*).

In the past few years, in-situ tunable strain has proven to be a powerful tool to probe and control exotic phases in both topological (*36*, *113*) and strongly correlated materials (*58*, *114*, *115*). Most of the in-situ strain work to date relies on the measurement of electrical resistivity as a probe of the electronic structures. In this paper, we introduce an apparatus design that measures the Seebeck coefficient as a function of in-situ strain. The apparatus described here offers in-situ control of strain up to +/- 0.7% strain at 100K, while simultaneously measuring the Seebeck coefficient with fine resolution. As a demonstration, we performed measurements on single crystal of $BaFe_2As_2$. BeFe2As2 goes through a tetragonal to orthorhombic structural transition near 135K and forms dense twin domains. We applied uniaxial stress to detwin the crystal and determined the Seebeck coefficient anisotropy, which is in agreement with previous measurements using a mechanical clamp (*116*).

EXPERIMENTAL SETUP

We used a home-built three-piezo strain apparatus to control strain, as shown in Figure 8-1a. This three-piezo technique was first introduced by Hicks et al (*35*). It has the advantage of minimizing uncontrolled strain bias due to the mismatch in thermal contraction. This apparatus also provides a large in-situ uni-axial strain tunability. As shown in Figure 8-1, the apparatus induces tensile and compressive stress by changing the width of a gap between two pieces of titanium blocks, which are glued to the outer and inner piezostacks. Titanium was chosen as the construction material due having a similar thermal constraction as the transverse direction of the piezostacks, as noted in previous works (*35*). Applying voltages of opposite polarity to the outer and the inner piezostacks results in a displacement of titanium blocks, which applies a uni-axial stress to a crystal glued across the gap. For the thermopower measurement, a 0.031-inch thick piece of G-10 was glued on either side of this gap to provide thermal insulation. Next, cernox sensors (CX-1050-SD, Lake Shore Cryotronics) were glued on top of this G-10 layer. Finally, strain-gauge heaters (KFH-1.5-120-C1-11L1M2R, OMEGA) were glued on each cernox sensor, and a crystal was glued across the gap between the cernox sensors, as shown in Figure 8-1 b-c. We used STYCAST 2850FT, Loctite epoxy for each layer of glue. A strain gauge (MMF003096, Micro-measurements) was glued on the side surface of one of the outer piezostacks to measure its strain, ϵ_{piezo}. The total strain induced by the gap displacement is estimated as $\epsilon_{xx}^{disp} = 2 \times \frac{L}{l} \times \epsilon_{piezo}$, where L is the length of the piezostack (9mm) and l is the adjustable width of the apparatus gap. For the apparatus presented in this paper l~0.75mm, which translates to ϵ_{xx}^{disp} ~ 0.7% at T = 100K for typical voltages applied to the piezostacks. The actual strain experienced by the crystal is typically 70% of ϵ_{xx}^{disp} due to the strain relaxation in the G10, epoxy and cernox. A detailed finite element simulation of strain relaxation is presented in Finite Element Analysis.

We used a Janis flow cryostat (ST-100, Janis Research) to provide the cryogenic environment. Since the Janis cryostat operates under vacuum pressures of order ~10^{-6} Torr, heat conduction from the cold head to the sample must be bridged by the piezostacks if no other conduction path is provided. The piezostacks are extremely thermally insulating. In order to more efficiently cool the sample, we used twisted bare copper wire pairs to provide addition heat conduction path. As shown in Figure 8-1a, the twisted wires were adhered to the titanium blocks by STYCAST 2850FT epoxy and the wires are flexible enough to allow the displacement of titanium blocks.

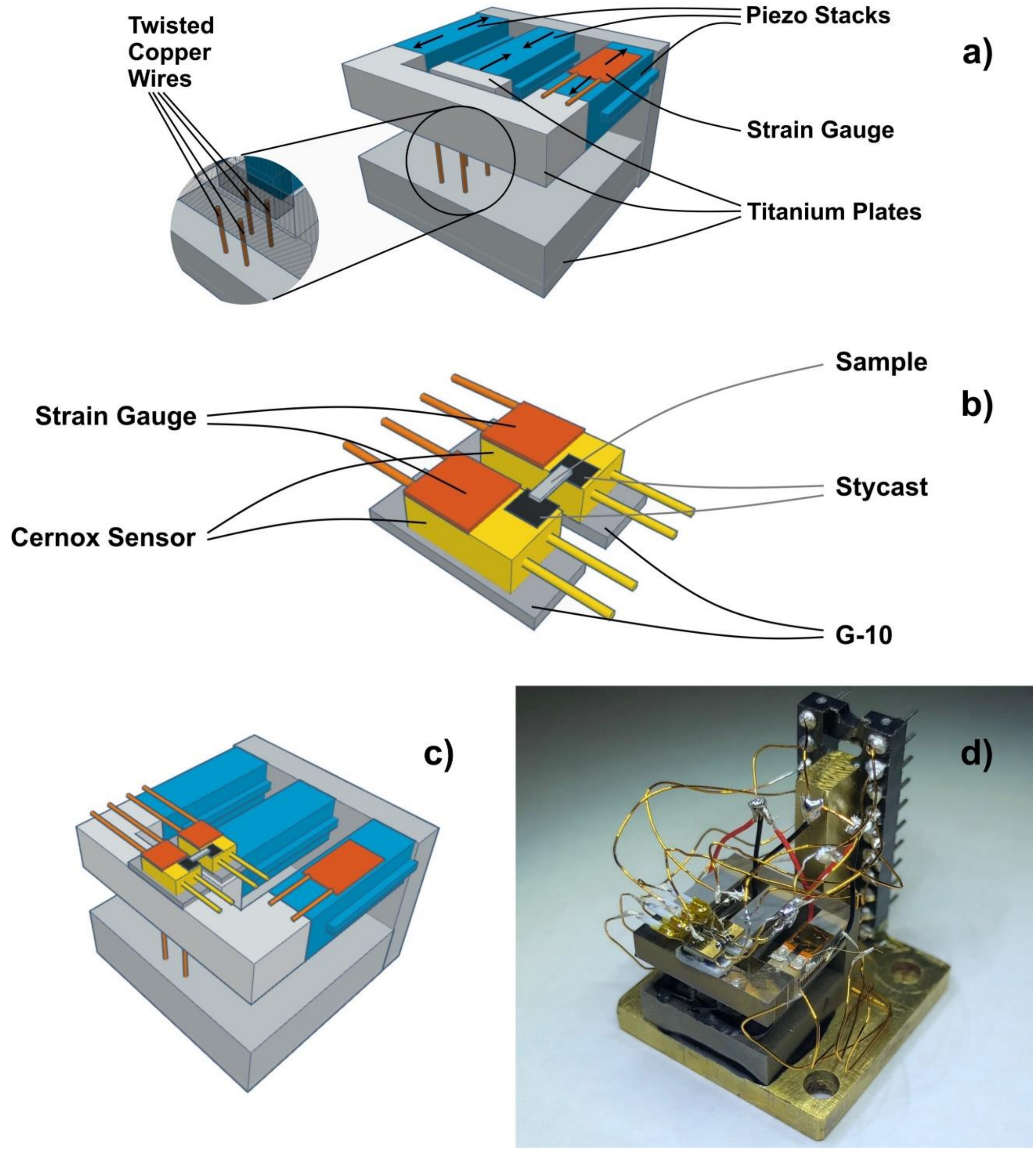

Figure 8-1: Strain controlled thermopower measurement apparatus. (a) Three piezostack strain apparatus: Piezostacks are shown blue, strain gauges in orange, titanium plates in gray, and the twisted copper thermal bridges are shown in the inset. Arrows show the displacement of the piezostacks when providing tensile strain. (b) Seebeck measurement components. The strain gauges are shown orange. The two smaller strain gauges act as heaters, while the larger strain gauge measures ϵ_{piezo}. The cernox sensors are shown in yellow, the G-10 plates are shown in dark gray, and the STYCAST used to adhere the crystal is shown in black. (c) The assembled entire apparatus, combining both the strain mechanics shown in (a) and the Seebeck components shown in (b). The Seebeck measurement components are mounted across the gap that is displaced by the strain apparatus. (d) Photograph of the apparatus.

The electrical schematic of the apparatus is shown in Figure 8-2, following the design introduced by Eundeok et al (*117*). To minimize unwanted emfs arising from thermal gradients in the cryostat, we used phosphor bronze wiring for the sample voltage measurement. A 32-gauge phosphor bronze wire (Lake Shore Cryotronics) was used to connect the electrical feedthrough of the Janis to the top of the cold head. This wire was briefly interrupted by a stainless-steel dip socket connection for ease of assembly, and eventually connected to 25-micron diameter phosphor bronze wire (Goodfellow, 346-032-19). This 25-micron diameter phosphor bronze wire made contact to the crystal using DuPont 4929 silver paint. To further eliminate an offset error resulting from thermal emfs, we employed a “heater switching” method, similar to a method reported by Eundeok et al (*117*). By alternating heating each end of the sample, erroneous thermal emfs in the circuitry can be eliminated by examining the difference of the sample voltage response to each heating configuration.

A single crystalline sample of $BaFe_2As_2$ was prepared by cleaving and cutting into a rectangular shape. The dimensions of the sample are approximately 1mm×0.1mm×0.01mm. The sample was sputtered with gold on two ends and a two points contact was made using phosphor bronze wire and silver paste. Non-destructive recovery of the crystal after the measurement was performed was not possible, as the glued crystal had to be scraped off of the apparatus with a knife.

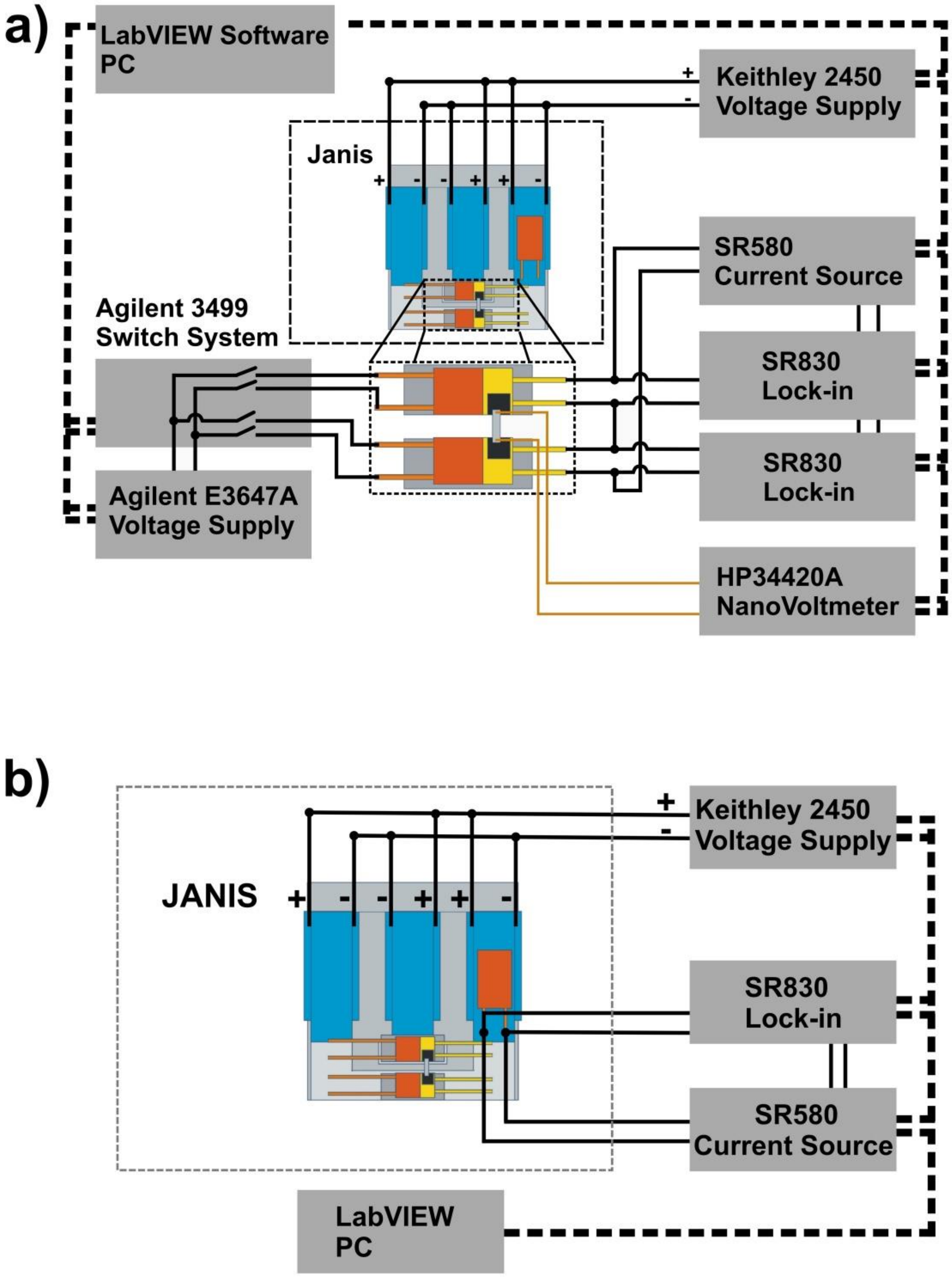

Figure 8-2: Diagram and circuitry for strain controlled thermopower measurement. Block diagram of the experimental circuitry for (a) Seebeck measurement and (b) strain measurement. (a) The system temperature is controlled by a Lakeshore 335 temperature controller. All instruments shown are controlled by LabVIEW software via a GPIB interface. The strain gauges acting as heaters are powered by a DC voltage supply (E3647A, Agilent). The resistances of the

cernox sensors are measured by two Lock-in Amplifiers (SR830, Stanford Research System) and a voltage controlled current source (CS580, Stanford Research System). The voltage applied to the parallel piezo stacks is controlled by an interactive source meter (Model 2450, Keithley). The sample voltage is measured by a nanovoltmeter (HP34420A). (b) Circuit diagram for the strain measurement of ϵ_{piezo}. The resistance of the strain gauge is measured using a 4-point measurement with one of the lock-in amplifiers and the voltage controlled current source. Altogether, the system uses 18 electrical pins, making it possible to do with a standard 19-pin feedthrough.

MEASUREMENT PROCEDURE

Prior to the measurement, the cernox censors were calibrated in order to obtain an accurate temperature profile on both sides of the sample. The setup is the same as shown in Figure 8-2a, except the sample voltage wasn't recorded and the heater voltage was set to 0V. The resistance of both cernox sensors was measured at temperature set points in 1.5K intervals. To overcome any thermal lag, we waited for 10 minutes for the apparatus to reach temperature stability at each temperature setpoint. This data was linearly interpolated to provide a temperature calibration over the relevant temperature range.

The Seebeck coefficient was measured at fixed strain setpoints. First, the cryostat was ramped to a temperature setpoint, then given 30 minutes to establish temperature stability. Prior to performing the Seebeck measurement, a strain measurement of ϵ_{piezo} was performed to estimate the strain delivered to the crystal, using the circuitry shown in Figure 8-2b. A voltage triangle wave was applied to the piezostacks, as shown in Figure 8-3a. This triangle wave looped three times to inspect the repeatability of the piezostack hysteresis curve. At the same time, the resistance of the foil strain gauge glued to one of the piezostacks was measured to determine ϵ_{piezo}, shown in Figure 8-3b. The offset expansion feature of the SRS 830 Lock-in was used to enhance the sensitivity of the resistance measurement. Inspecting the foil strain gauge resistance as the piezostacks were trained showed a difference between the first and second voltage waves, which is likely due to the charge built up from the pyroelectric effect of the ferroelectric materials of the piezostacks (*19*). However, the second and third voltage waves showed a consistent piezostack hysteresis. By applying this voltage waveform to the piezostacks prior to measuring the Seebeck coefficient, the piezostacks are trained to operate on a consistent hysteresis curve, and the measured ϵ_{piezo} of either the second or third wave can be used to calibrate the Seebeck measurement later. Repeating this process after the Seebeck coefficient measurement showed no evidence of strain drift over time.

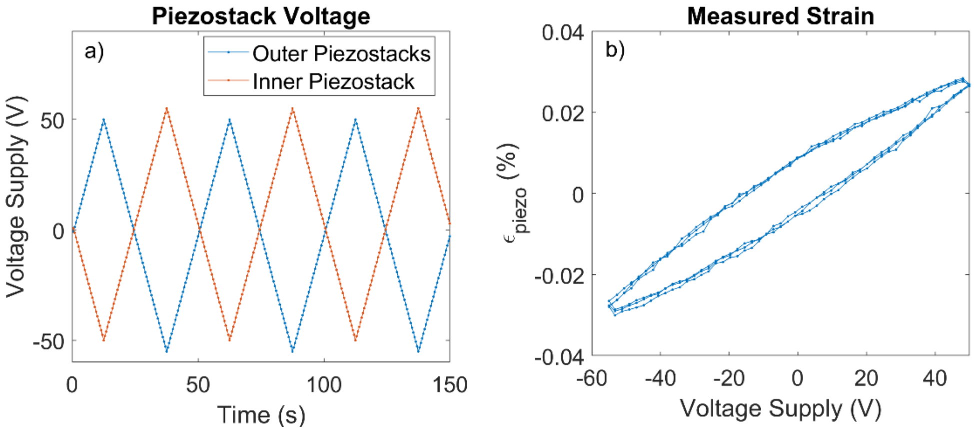

Figure 8-3: Strain provided by piezostacks versus voltage supply to piezostacks at 120K (a) Voltage across the inner and outer piezostacks with respect to time. (b) ϵ_{piezo} measured by the foil strain gauge versus voltage supply across one of the outer piezostacks. Three voltage loops across the piezostacks were performed in order to inspect the repeatability of the piezostack hysteresis.

After training the piezostacks and measuring ϵ_{piezo}, the voltage of the piezostacks was ramped to a fixed setpoint, and given one minute to stabilize. Next, one heater (Heater #1) attached to one of the cernox sensors was turned on by applying a DC voltage across the heater. After two minutes, Heater #1 was turned off, and Heater #2 was turned on. Heater #2 stayed on for two minutes, then was turned off as well. Both heaters were kept off for 1 minute to complete one heating cycle. During this heating cycle, the temperature of each cernox sensor and the voltage output from the sample was recorded and displayed live time by a LabVIEW program, similar to what is shown in Figure 8-4a-b. Monitoring this output in real time allowed the parameters (heating time, heating power) to be adjusted as necessary to ensure that a stable temperature gradient is reached within the heating cycle. We targeted $\Delta T = \sim 1K - 2K$, and found heating powers of $3mW - 15mW$ generally accomplished this. After completing one heating cycle, the voltage across the piezostacks was then ramped to the next set point, and another heating cycle began. The strain loop was repeated at least three times to inspect the repeatability of the result.

The Seebeck coefficient was determined by using the difference in temperature and difference in sample voltage extracted from the equilibrium portions of the dataset, after each heater had been on for two minutes. We follow the explanation given in (*117*) to extract the Seebeck coefficient. Letting the subscript *i* indicate the time just before alternating power to the heaters, and the subscript *f* indicate the time just before turning off both the heaters, then

$$2\mathit{\Delta} T = T_{2f} - T_{1f} + (T_{1i} - T_{2i})$$

$$2\Delta V = V_f - V_i$$

$$T_{avg} = \frac{T_{1f} + T_{1i} + T_{2f} + T_{2i}}{4}$$

$$S = -\frac{2\Delta T}{2\Delta V}$$

It is recognized that both the factor of 2 in 2ΔT and 2ΔV results from the alternative heating scheme. The temperature corresponding to the measured Seebeck coefficient corresponds most closely to T_{avg}.

From the data recorded during each heating cycle, the Seebeck coefficient S was plotted against the piezostack voltage, as shown in Figure 8-4f. The pronounced hysteresis is associated with the hysteretic strain-voltage response of piezostacks. To remove this hysteresis effect, the measured strain ϵ_piezo from the foil strain gauge was used to calibrate strain per voltage for increasing and decreasing voltage. By estimating $\epsilon_{xx}^{disp} = 2 \times \frac{L}{l} \times \epsilon_{piezo}$, as discussed in the Experimental Setup section, the Seebeck coefficient can be plotted against the apparatus strain, and the hysteresis effect is removed. Our finite element analysis estimates a relaxation factor α~0.67, which indicates that the strain delivered to the sample is $\epsilon_{aa} = \alpha\epsilon_{xx}^{disp}$. In Figure 8-5, we plot the Seebeck coefficient versus ϵ_{aa} for the same dataset as shown in Figure 8-4f, as well as an additional dataset that includes higher magnitude strains. A large Seebeck coefficient response to strain is seen for low strains, with a saturating behavior at large strains. The saturated values are consistent with previously reported values (*116*, *118*) measured by a mechanical clamping method, shown in the inset in Figure 8-5.

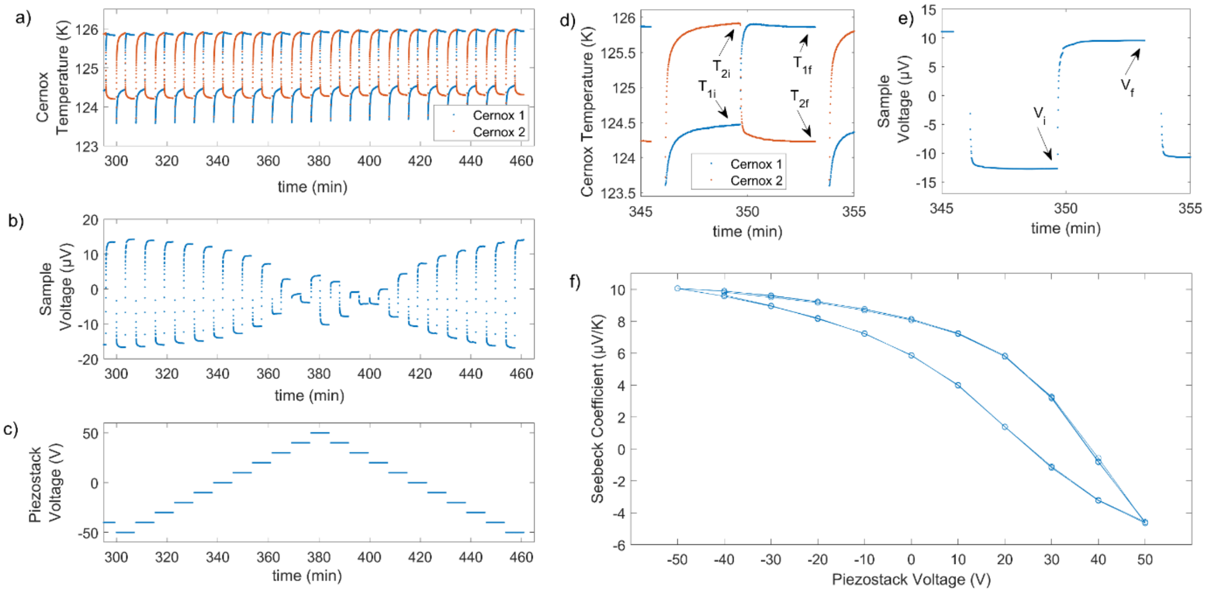

Figure 8-4: Data from strain controlled thermopower measurement for $BaFe_2As_2$ at 125K. (a) Temperature on each side of the sample versus time. Each side of the sample was heated in an alternating fashion. (b) Voltage measurement across the sample for approximately 20 heat cycles in one strain loop (c) Voltage supplied to the piezostacks. Positive (negative) voltage across the piezostacks corresponds to tensile (compressive) stress applied to the sample. The time scale of the x axis in (a-c) corresponds to one strain loop. (d-e) Zoomed in views of (a) and (b), respectively. The time scale of the x axis in (d-e) corresponds to one measurement at a fixed strain setpoint. The initial and final temperatures of the cernox sensors and voltage of the sample are shown. (f) Calculated Seebeck coefficient versus piezostack voltage. Several strain loops of data are shown to inspect repeatability of the measurement. A hysteresis is seen, which is associated with the hysteretic behavior of the piezostacks.

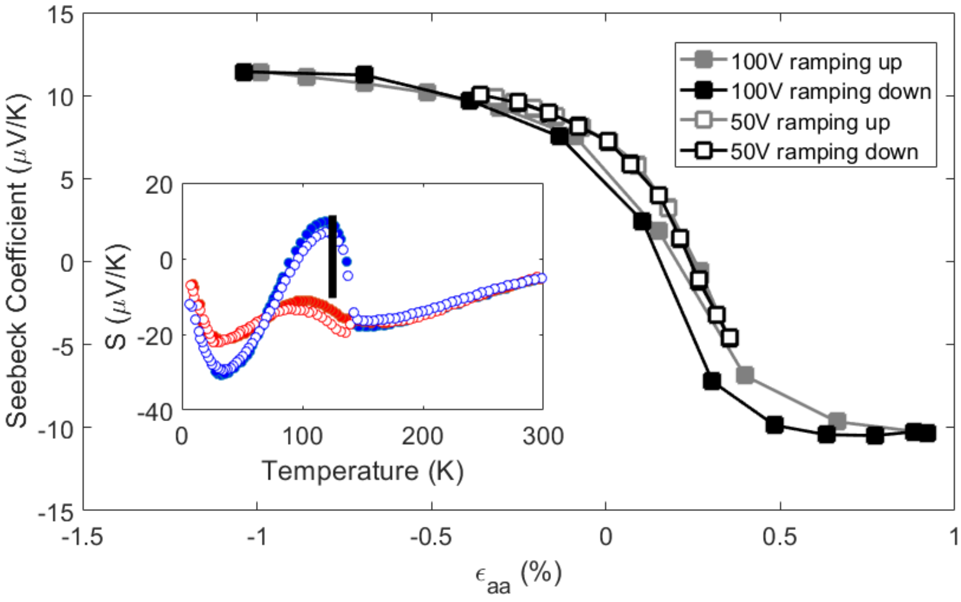

Figure 8-5: The Seebeck Coefficient versus strain of BaFe2As2 at 125K. Increasing strain and decreasing strain are shown in two different colors (gray and black, respectively). The hysteresis seen in Figure 8-4f was removed by using ϵ_{piezo} as measured by the strain gauge for increasing and decreasing strain. The strain reported in the x axis, ϵ_{aa}, is given by $\epsilon_{aa} = 0.67 \times 2 \times \frac{L}{l} \times \epsilon_{piezo}$, as described in the Experimental Setup section. where 0.67 is a relaxation factor calculated by finite element analysis. There is an uncertainty $\delta\epsilon$ associated with the zero strain point due to the difference between the thermal contraction of the titanium apparatus and the crystal ($\Delta\epsilon_{thermal}$), as well as a difference in twin domain populations between the strained crystal and the unstrained crystal ($\Delta\epsilon_{domain}$). These uncertainties are estimated at $|\Delta\epsilon_{thermal}| < 0.16\%$ and $|\Delta\epsilon_{domain}| < 0.75\%$ (*119–121*). INSET: The Seebeck coefficient of detwinned BaFe$_2$As$_2$, data taken from (*116*). Here, the crystal has been detwinned by mechanical clamping. The red (blue) circles correspond to the Seebeck coefficient along the *a* (*b*) lattice direction, while the open and closed circles correspond to measurements on two different samples. The black bar at 125K indicates the range of tunability measured by our apparatus.

DISCUSSION AND CONCLUSION

Most of the strain dependent Seebeck coefficient measurements reported to date have been done by mechanical clamping (*116*, *118*). While this technique has the benefit of delivering large amounts of strain, controllable in-situ strain measurements are desirable to monitor the exact Seebeck-strain dependence. A very recent report demonstrated the measurements of elasto-Seebeck and elasto-Nernst measurements of the 1111 iron-based superconductors by gluing the crystals on the sidewall of piezo-stacks, yet the amount of strain that can be delivered by this method is an order of magnitude smaller than the our setup (*122*). Although we only present measurements in zero field, the set up could be easily extended to an environment with magnetic fields because of the low field dependence of the cernox thermometry used. Field-dependent thermoelectric measurements have already provided useful information in strongly correlated electron systems and high-T_c superconductors. Adding another control knob of strain can be a useful and exciting tool.

FINITE ELEMENT ANALYSIS

In order to estimate the strain transmission, defined as the ratio of strain delivered to the crystal to the apparatus strain, we modelled our setup with the ANSYS Academic Research Mechanical 19.1 finite element analysis package. 3-piezo strain apparatuses such as the one we use have been used before in literature (*36*, *58*, *113*). In these simpler systems, the strain transmission is generally above 70%, depending on the crystal composition and dimensions and mounting technique. However, in our more complicated system, G-10, Cernox sensors, and finally the crystal are stacked together and adhered with stycast epoxy. This allows for a stronger relaxation effect associated with the glue. Our finite element model investigates if these effects are significant.

We modelled a 2mm x 0.2mm x 0.02mm $BaFe_2As_2$ crystal glued across our apparatus. The elastic coefficients of this crystal were sourced from Fujii et al (*123*) at 250K, with the missing C_{13} coefficient estimated as 34 GPa by comparison between Fujii et al. and the stiffness tensor calculated by the Materials Project. The crystal was mounted such that strain was applied along the Fe-Fe direction. The cernox sensors, stycast glue, and G-10 plastic were all modelled as isotropic, and the values for the Young’s modulus and Poisson’s ratio used in our model are given in Table 8-1. The stycast glue is modelled as 0.02mm thick for most connections, and 0.01mm thick between the cernox sensor and the crystal.

Component	**Young’s Modulus (GPa)**	**Poisson’s ratio**
Cernox sensor	400	0.245
G-10	18	0.13
Stycast epoxy[15]	15	0.3

Table 8-1: Finite element input parameters for analysis of strain controlled thermopower apparatus. The cernox sensors were modelled as 99.5% alumina. While the physical properties of alumina depend on purity, the Young’s modulus is always at least one order of magnitude higher than any other material in our apparatus. The G-10 properties are were modelled according to the manufacturer datasheet.

In our model, we analyzed a 0.1% tensile strain applied to the apparatus and calculated the average strain transmission in the crystal in the strained region. This yielded a strain transmission of 67%, as opposed to 88% with the same crystal similarly epoxied to a bare 3-piezo device. Figure 8-6 shows a schematic of the simulation results.

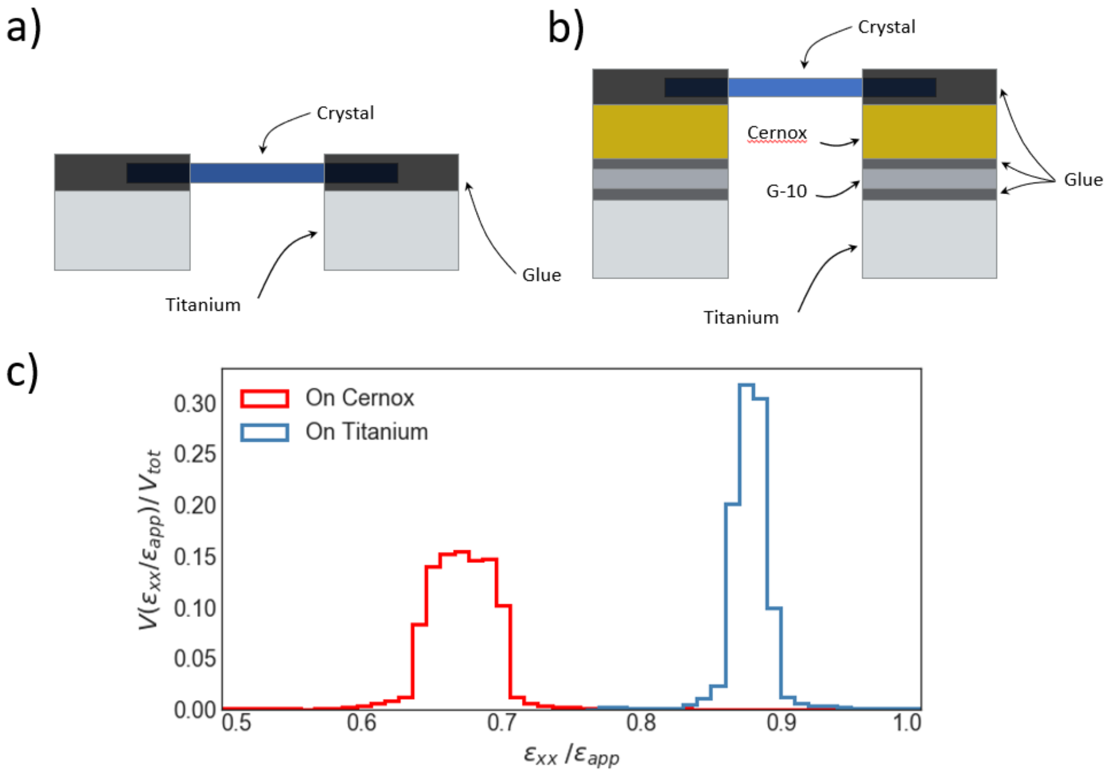

Figure 8-6: Finite element analysis of strain controlled thermopower apparatus. a) Schematic (not to scale) of the Finite Element Analysis (FEA) model for a crystal glued directly across two titanium block in a simple strain apparatus. The gap between the titanium blocks was displaced to induce a strain of $\epsilon_{xx}^{disp} = 0.1\%$. b) Schematic of the FEA model for a crystal glued to our strain and Seebeck apparatus. Several elements are stacked together and adhered with glue, allowing for a stronger relaxation effect associated with the glue. The glue thickness between the apparatus and G-10, and between the G-10 and the Cernox sensor was modelled as 0.02mm thick. The glue thickness between the Cernox sensor and crystal was modelled as 0.01mm thick. c) Average strain transmission for models shown in a) (blue line) and b) (red line). The volume fraction of the crystal is plotted as a function of strain transmission, binned into 1% strain transmission intervals. The average strain delivered to the crystal is $\overline{\epsilon_{aa}} = 0.88\epsilon_{xx}^{disp}$ for model a), and $\overline{\epsilon_{aa}} = 0.67\epsilon_{xx}^{disp}$ for model b). Model b) has a wider volume fraction distribution of strain compared to direct gluing on the titanium. In both models, the ends of the crystal are submerged in the glue.

Acknowledgement

This work was supported by NSF MRSEC at UW (DMR-1719797) as well as the Gordon and Betty Moore Foundation's EPiQS Initiative, Grant GBMF6759 to J.-H.C. J.-H.C. also acknowledges the support from the State of Washington funded Clean Energy Institute, The Alfred P. Sloan Foundation and The David Lucile Packard Foundation.

APPENDIX 2 – ANISOTROPIC THERMOPOWER MEASUREMENTS OF TAIRTE4 AND NBIRTE4

ABSTRACT

Materials with a p-type Seebeck coefficient in one direction and an n-type coefficient in the other (so-called "$p \times n$ type materials") have attracted recent attention due to their applications in transverse thermoelectric devices (*124*, *125*). Despite the desirable nature of these materials, very few materials with sizable p x n type behavior have been discovered to-date. Here, we report the observation of $p \times n$ type behavior in $TaIrTe_4$, which obtains a maximum thermopower anisotropy $S_{xx} - S_{yy} \sim 40 \mu V/K$ with minimal temperature variation between 150K and 300K. We discover that such $p \times n$ type behavior is absent in the similar compound $NbIrTe_4$. We compare thermopower and resistivity measurements between these two compounds as well as examine DFT calculations to examine the source of the $p \times n$ type behavior in $TaIrTe_4$.

INTRODUCTION

Transverse thermoelectric devices have been shown to provide geometric tuning advantages compared to longitudinal thermoelectrics (*125*, *126*). Transverse thermoelectric behavior can be obtained by engineering composite devices of layered p-type and n-type materials, the Nernst effect, or through intrinsic $p \times n$ type materials. $p \times n$ type materials are particularly desirable due to the simplicity of device design compared to composite devices and no magnetic field requirement. In $p \times n$ type materials, current and heat can flow in orthogonal directions if the applied gradient is not along a principal axis of the material. This transverse flow of current and heat enables greater efficiencies and coefficients of performance for heat recovery and refrigeration applications compared to parallel current and heat flow, even in materials with the same figure of merit. The performance of devices using $p \times n$ type architecture can be additionally enhanced through geometric tapering of the device. Similar performance increases in longitudinal thermoelectrics can only be achieved through much more complicated device architecture, such as a cascading design of stacked layers of materials.

Searching for new $p \times n$ type materials has been the focus of recent works (*127*), and the most common mechanism responsible for $p \times n$ type behavior is the multiband effect, where *p*-type bands *n*-type bands dominate conduction in different directions. In a two-band model of one *p*-type band and one *n*-type band, the total Seebeck tensor can be expressed as:

$$\boldsymbol{S} = \left(\boldsymbol{\sigma_p} + \boldsymbol{\sigma_n}\right)^{-1}(\boldsymbol{\sigma_p S_p} + \boldsymbol{\sigma_n S_n})$$

Despite the potential for applications of $p \times n$ type materials, only a handful of materials have been identified that display this behavior (*128*). Even fewer materials have been identified with a peak thermopower anisotropy greater than $5\mu V/K$ or that persists beyond low temperatures, and to the best of our knowledge this list only includes $ReGe_XSi1.75_{1-x}$ (*129*), $CsBi_4Te_6$(*130*), $NaSnAs_2$ (*131*), $Al_{13}Co_4$ (*132*), $Tl_2Ba_2CuO_{6-x}$ (*13*, and (BEDT-TTF)$_2$Cu[N(CN)$_2$]X (X=Cl, I, Br) (*133, 134*). Of these materials, all except j-(BEDT-TTF)$_2$Cu[N(CN)$_2$]X (abbreviated to k-X) exhibit $p \times n$ type behavior only when comparing in and out of plane thermopowers. Even the behavior of k-X is pseudo out of plane since the $p \times n$ type behavior is orthogonal to 1D chains within its complicated unit cell. Here we report the first observation of in-plane $p \times n$ type behavior in single crystals of $TaIrTe_4$. Interestingly, we find this behavior absent in $NbIrTe_4$, which is purely *p*-type in both directions. DFT band structure calculations indicate the $p \times n$ type behavior in $TaIrTe_4$ results from enhanced mobility of the *n*-type bands in the *x* direction, which display steeper curvature in the *x* direction compared to the *n*-type bands in the Nb compound.

$TaIrTe_4$ and $NbIrTe_4$ both crystallize in a noncentrosymmetric orthorhombic structure of space group Pmn21 (*135*, *136*), shown in Figure 8-7(a). Tellurium octahedra structures form in the *a/b* plane, with alternating tantalum and iridium atoms contained within the octahedra structures. These layers van der Waals couple in the out of plane *c* lattice direction. DFT calculations indicate that $NbIrTe_4$ hosts two closed hole pockets and two electron pockets that are open along the k_z direction (*136*), and SdH measurements corroborate this band structure (*137*). DFT calculations on $TaIrTe_4$ indicate three closed hole pockets and two electron pockets that are open along the ky direction (*135*). dHvA measurements on $TaIrTe_4$ broadly corroborate this band structure, although they indicate a fermi energy ~30-40 meV higher than calculated that eliminates the smallest hole pocket and possibly introduces additional electron pockets (*138*). Both materials are predicted to host tilted type-II Weyl nodes; $NbIrTe_4$ is predicted to host 16 nodes (12 above and 4 below the fermi energy), and $TaIrTe_4$ is predicted to host 4 nodes (approximately 80meV above the calculated fermi energy).

RESULTS

Bulk single crystals of $TaIrTe_4$ and $NbIrTe_4$ were grown out of Te flux following procedures similar to previous reports (*135*). Ta or Nb powder, Ir powder, and Te shot were mixed in an atomic ratio of 1:1:20 with a total mass of starting material ~ 3.5g and loaded into alumina crucibles which were then sealed in quartz tubes under a low-pressure argon environment. The growths were placed into box furnaces and heated to 1000 ℃ over 12 hours, held at 1000 ℃ for 24 hours, and then slowly cooled to 700 ℃ over 150 hours. The growths were then decanted via centrifuge to separate the excess Te flux from the resulting single crystals. For both compounds, the yield resulted in single crystals with shiny facets and ribbon or needle morphology.

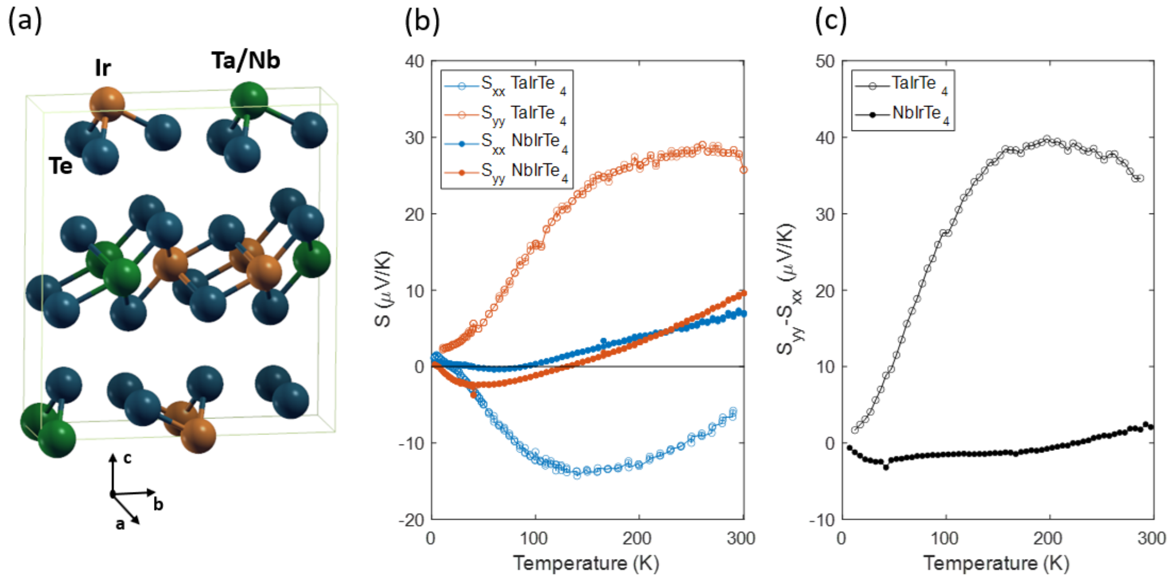

Figure 8-7: Anisotropic thermopower measurements of $TaIrTe_4$ and $NbIrTe_4$. (a) Crystal structure of XIrTe4. Tellurium atoms are shown in blue, iridium in orange, and the tantalum or niobium atoms are shown in green. (b) Thermopower measurements for $TaIrTe_4$ (open circles) and $NbIrTe_4$ (closed circles) along the *x* (blue) and *y* (red) directions. (c) The strength of the thermopower anisotropy, $S_{xx} - S_{yy}$, for $TaIrTe_4$ (open circles) and $NbIrTe_4$ (closed circles).

We measured the Seebeck coefficient and resistivity for $TaIrTe_4$ and $NbIrTe_4$ in the in-plane *a* and *b* lattice directions. We use the convention *x:y:z* to refer to the *a:b:c* lattice directions of the crystal. Figure 8-7 shows our main result: The sign of the Seebeck coefficient of $TaIrTe_4$ changes sign along different axes, measuring *n*-type in the *x* direction and *p*-type in the *y* direction. This directional dependence persists from 20K to the maximum temperature we measured at 300K and attains a maximum difference of $S_{xx} - S_{yy} = 40\mu V/K$ at 200K. Below 20K, small magnitude *p*-type behavior is measured in both directions. This strong anisotropic behavior is absent in the thermopower measurement of $NbIrTe_4$, where both S_{xx} and S_{yy} display similar temperature dependence and are smaller in magnitude compared to $TaIrTe_4$.

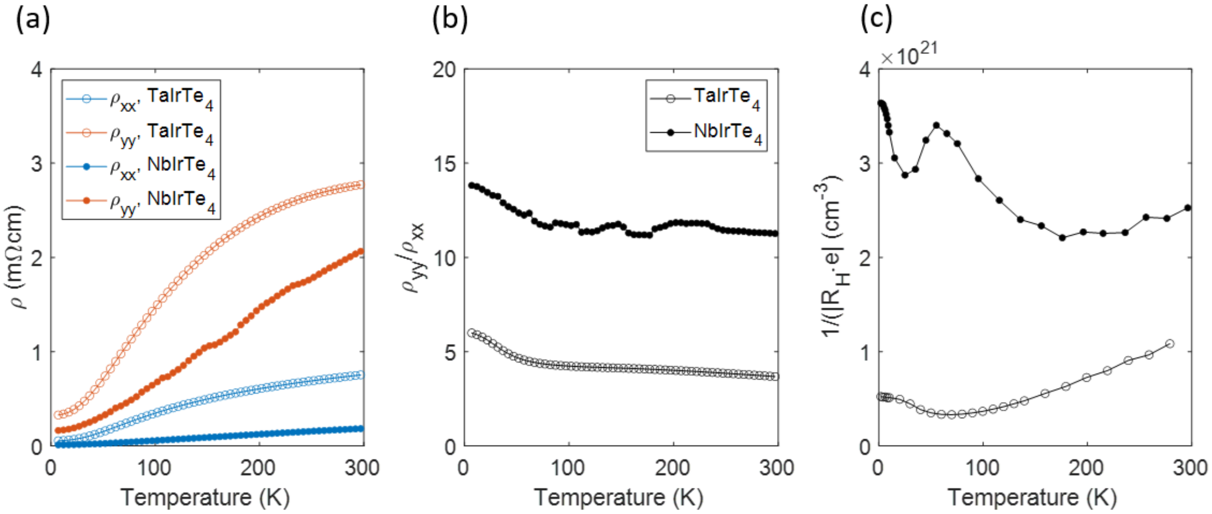

Figure 8-8: Anisotropic resistivity measurements in $TaIrTe_4$ and $NbIrTe_4$. (a) Resistivity measurements for TaIrTe4 and NbIrTe4 along the x and y directions. (b) The resistivity anisotropy of $NbIrTe_4$, defined as ρ_{yy}/ρ_{xx}, is stronger than that of $TaIrTe_4$. (c) Carrier density as approximated by a linear fit of the Hall resistivity between -1T and 1T.

To gain insight into the mechanism behind this $p \times n$ type behavior in $TaIrTe_4$, we also performed resistivity measurements along the in-plane axes for both the Ta and Nb compounds, shown in Figure 8-8. Both $TaIrTe_4$ and $NbIrTe_4$ show relatively strong in-plane resistivity anisotropy, with $\rho_{yy}>\rho_{xx}$ for both compounds. The resistivity anisotropy of $NbIrTe_4$ is greater than that of $TaIrTe_4$ by almost a factor of three, despite $NbIrTe_4$ being much more isotropic in the thermopower measurement.

This asymmetry between the thermopower and resistivity anisotropies is consistent with the multi-band effect required to generate $p \times n$ type behavior. Both electron and hole pockets with strong anisotropy are required to generate $p \times n$ type behavior, but the resistivity anisotropy of the electron and hole pockets must be rotated with respect to one another. Specifically, electron carriers that are highly mobile in the *x* direction and hole carriers that are highly mobile in the *y* direction could create the $p \times n$ type behavior seen in $TaIrTe_4$. Suppressing the *x* direction mobility of the *n*-type carriers would have the effect of enhancing the resistivity anisotropy but suppressing the thermopower anisotropy, as measured in $NbIrTe_4$. Therefore, the measurement of weaker resistivity anisotropy simultaneous to $p \times n$ type behavior is consistent with the multi-band mechanism of Equation 1 being responsible for the thermopower anisotropy in $TaIrTe_4$, rather than an alternative explanation such as the recently discovered goniopolar effect (*131*).

Both $TaIrTe_4$ and $NbIrTe_4$ host multiple electron and hole pockets necessary for $p \times n$ type behavior. To verify that the $p \times n$ type behavior observed in $TaIrTe_4$ is consistent with the reported band structure, we performed DFT calculations on both materials. Details about DFT calculation here.

Using our DFT band structure calculation, we calculated the thermopower along each in-plane direction for both compounds using Quantum Espressso. The results of the calculated Seebeck coefficient shown in Figure 8-9 are broadly consistent with our measurements. $NbIrTe_4$ is calculated to be much more isotropic and display a much smaller magnitude thermopower compared to $TaIrTe_4$, which is calculated to be *n*-type and *p*-type in the *x* and *y* directions, respectively. Despite the calculation predicting $NbIrTe_4$ to be *n*-type in the *y* direction, the small magnitude of the calculated thermopower is in excellent qualitative agreement to experiment, and small changes in the fermi energy can explain the quantitative discrepancies.

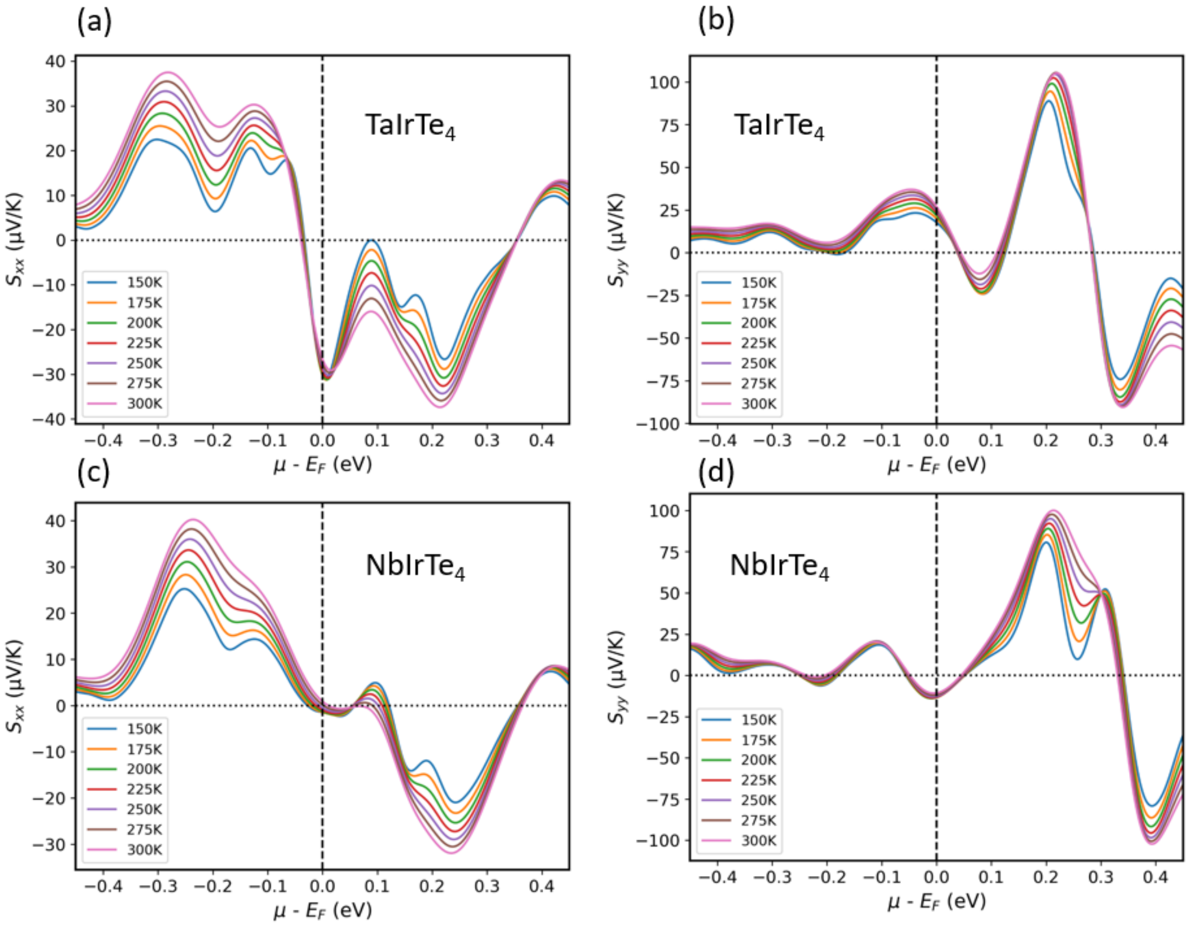

Figure 8-9: DFT calculations of $TaIrTe_4$ and $NbIrTe_4$ thermopower. The thermopower of $TaIrTe_4$ (a & b) and $NbIrTe_4$ (c & d), calculated along the x (a & c) and y (b & d) directions. The thermopower was calculated over a temperature range of 150K-300K, as denoted in the legend.

To demonstrate the applicability of $p \times n$ type materials to engineering transverse thermoelectric devices, we cut $TaIrTe_4$ samples at 25° and 55° degree angles to the x axis, and performed longitudinal and transverse thermopower measurements along the axes of the cut samples. In the rotated sample geometry, heat and charge flow are no longer parallel with one another, which creates a transverse Seebeck effect and suppresses the longitudinal Seebeck effect. As shown in Figure 8-10, we achieve a maximum $S_{xy} = 16\mu V/K$ and 18 μV/K for the 25° and 55° cuts, respectively. The maximum S_{xy} occurs near 250K in both instances, but shows relatively little variation between the temperatures of 200K and 300K. For the 25° cut, the magnitude of the longitudinal signal is very small over this temperature range, indicating the charge and heat flow are nearly orthogonal at this angle, ideal for efficient transverse thermoelectric devices.

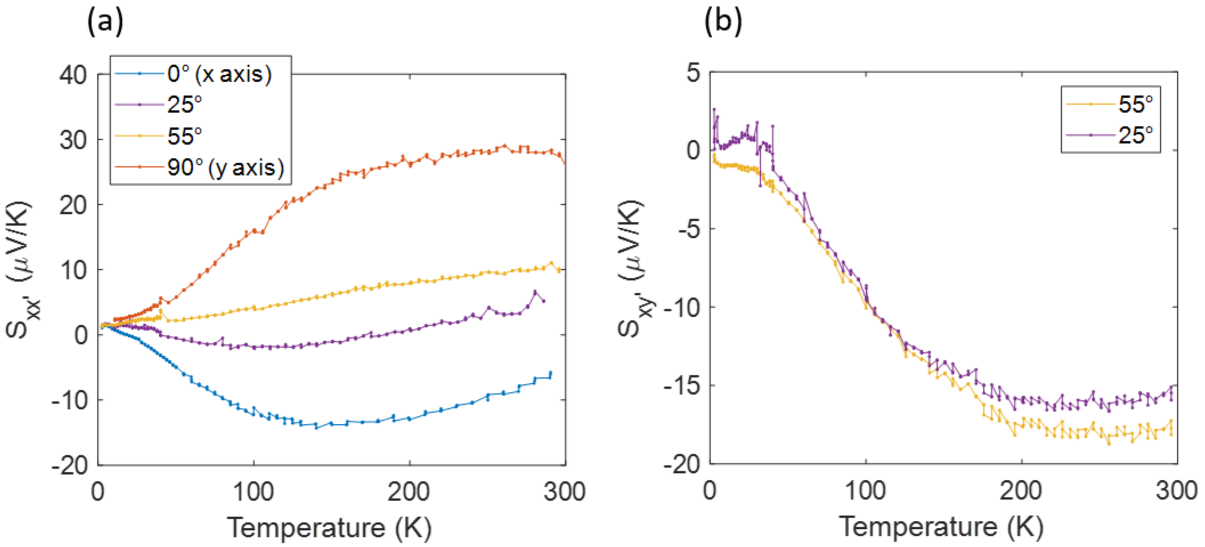

Figure 8-10: Longitudinal and transverse thermopower measurements on rotated $TaIrTe_4$ crystals. Longitudinal (a) and transverse (b) thermopower measurements for samples of TaIrTe4 cut at angles to the *x* axis. The longitudinal and transverse direction are with respect to the rotated direction of the cut sample, e.g., 0° and 90° directions are along the original *x* and *y* directions of the crystal. For the 25° and 55° cuts, non-zero diagonal terms of the Seebeck tensor $S_{xy'}$ are measured.

CONCLUSION

Transverse thermoelectric devices provide the potential for engineering advantages such as geometric tapering which are unavailable in traditional, longitudinal thermoelectrics. It was recently shown that a Nernst effect of 4-6 $\mu V/K$ in an iron-based compound could achieve large power generation capacity in micro-scale devices (*139*). $p \times n$ type materials are excellent candidates for transverse thermoelectric applications, since a transverse thermopower can be generated when samples are cut at an angle to the principal axes. In this study, we were able to achieve a transverse Seebeck coefficient of 18 μV/K in $TaIrTe_4$ in a sample cut at a 55° angle to the *x* axis.

Despite the advantages of $p \times n$ type materials, only a handful of materials with this behavior have been identified due to the difficulty of engineering multiple bands with rotated anisotropies. In $TaIrTe_4$, we report the first in-plane $p \times n$ type behavior and trace the origin of the effect to a combination of the Ta 5d, Ir 5d, and Te 5p orbitals creating strongly anisotropic electron and hole pockets. The effect is especially unique considering the large carrier density of TaIrTe4 – up to 10^{21} cm^{-3} carriers at room temperature. The uniqueness of such strong electrical anisotropy at such high carrier densities has been previously reported for $TaIrTe_4$ (*140*), but our results illuminate the fact that individual bands of carriers are even more anisotropic than electrical measurements indicate, since the resistivity measurement averages out multiple anisotropies. In $NbIrTe_4$, the p-type carriers more effectively dominate conduction, and the resistivity measurements are more indicative of the anisotropy of just these carriers.

It is worth addressing the topological nature of both $TaIrTe_4$ and $NbIrTe_4$, which are both predicted to be type-II Weyl semimetals with tilted Weyl cones. Connections between topological materials and good thermoelectric materials have been pointed out before, exemplified by Bi_2Te_3, a longstanding hallmark of thermoelectric materials as well as a topological insulator. The simplest connection between topology and thermoelectricity seems to be that they both favor heavy elements: in thermoelectricity heavy elements aid in reducing thermal conductivity, while in topology the heavy elements help induce spin-orbit coupling which helps aid the band inversion process (*141*). It seems the $p \times n$ type behavior in $TaIrTe_4$ is unrelated to the existence of the Weyl nodes, and not dictated by some fundamental topology. The first indicator that the coexistence of $p \times n$ type behavior and Weyl nodes is a coincidence is that the Weyl nodes of $TaIrTe_4$ are associated only with the p-type bands, while strong anisotropy of both the p-type and the n-type bands is crucial for $p \times n$ type behavior. Additionally, $NbIrTe_4$ is also a Weyl semimetal, but $p \times n$ type behavior is absent in this compound, indicating that Weyl nodes are not a sufficient requirement to observe $p \times n$ type behavior. It seems that the complicated band structures induced by spin orbit coupling may coincidentally create both $p \times n$ type behavior and Weyl nodes, but one does not imply the other.

In conclusion, we have measured the thermopower and resistivity anisotropies of TaIrTe4 and $NbIrTe_4$. $TaIrTe_4$ displays strong thermopower anisotropy leading to $p \times n$ type behavior, while the thermopower of $NbIrTe_4$ is much more isotropic. Conversely, the resistivity anisotropy of $NbIrTe_4$ is much stronger than the resistivity anisotropy of $TaIrTe_4$. All these findings are consistent with a multi-band effect creating the $p \times n$ type behavior in $TaIrTe_4$, which is further consistent with DFT calculations of the band structure that indicates that the highly anisotropic p and n bands are associated with the Ta 5d, Ir 5d, and Te 5p orbitals. While any applications are limited due to the low earth abundance of these materials, such in-plane $p \times n$ type behavior is completely novel. This opens the door for a search of more materials within this family with potential applications in $p \times n$ type thermoelectrics.

BIBLIOGRAPHY

1. X. L. Qi, S. C. Zhang, The quantum spin Hall effect and topological insulators. *Physics Today*. **63**, 33–38 (2010).

2. D. J. Thouless, M. Kohmoto, M. P. Nightinggale, M. de Nijs, Quantized Hall conductance in a two dimensional periodic potential. *Physical Review Letters*. **49**, 405 (1982).

3. X. Qian, J. Liu, L. Fu, J. Li, Quantum spin Hall effect in two-dimensional transition metal dichalcogenides. *Science*. **346**, 1344–1348 (2014).

4. J. E. Avron, D. Osadchy, R. Seiler, A topological look at the quantum hall effect. *Physics Today*. **56**, 38–42 (2003).

5. K. v. Klitzing, G. Dorda, M. Pepper, New method for high-accuracy determination of the fine-structure constant based on quantized hall resistance. *Physical Review Letters*. **45**, 494–497 (1980).

6. J. E. Avron, D. Osadchy, R. Seiler, A topological look at the quantum hall effect. *Physics Today*. **56**, 38–42 (2003).

7. J. Riess, Quantized Hall conductance as a topological invariant. *Epl*. **31**, 3372–3377 (1985).

8. B. I. Halperin, Quantized Hall conductance, current-carrying edge states, and the existence of extended states in a two-dimensional disordered potential. *Physical Review B*. **25**, 2185–2190 (1982).

9. M. Z. Hasan, C. L. Kane, Colloquium: Topological insulators. *Reviews of Modern Physics*. **82**, 3045–3067 (2010).

10. R. Jackiw, C. Rebbi, Solitons with fermion number. *Physical Review D*. **13**, 3398–3409 (1976).

11. W. P. Su, J. R. Schrieffer, A. J. Heeger, Solitons in polyacetylene. *Physical Review Letters*. **42**, 1698–1701 (1979).

12. Topology in Condensed Matter, (available at https://topocondmat.org/w3_pump_QHE/QHEedgestates.html).

13. M. König, L. W. Molenkamp, X. Qi, S. Zhang, Quantum Spin Hall Insulator State in HgTe Quantum Wells. *Science*. **318766**, 766–771 (2007).

14. C. Wu, B. A. Bernevig, S. C. Zhang, Helical liquid and the edge of quantum spin hall systems. *Physical Review Letters*. **96**, 1–4 (2006).

15. C. L. Kane, E. J. Mele, Quantum Spin hall effect in graphene. *Physical Review Letters*. **95**, 1–4 (2005).

16. X. L. Qi, S. C. Zhang, The quantum spin Hall effect and topological insulators. *Physics Today*. **63**, 33–38 (2010).

17. L. Fu, C. L. Kane, Topological insulators with inversion symmetry. *Physical Review B - Condensed Matter and Materials Physics*. **76**, 1–17 (2007).

18. S. Murakami, Phase transition between the quantum spin Hall and insulator phases in 3D: Emergence of a topological gapless phase. *New Journal of Physics*. **9** (2007), doi:10.1088/1367-2630/9/9/356.

19. N. W. Ashcroft, N. D. Mermin, Solid State Physics (1976).

20. H. Weng, X. Dai, Z. Fang, Transition-metal pentatelluride ZrTe5 and HfTe5: A paradigm for large-gap quantum spin hall insulators. *Physical Review X*. **4**, 1–8 (2014).

21. H. Wang, H. Liu, Y. Li, Y. Liu, J. Wang, J. Liu, J. Y. Dai, Y. Wang, L. Li, J. Yan, D. Mandrus, X. C. Xie, J. Wang, Discovery of log-periodic oscillations in ultraquantum topological materials. *Science Advances*. **4** (2018), doi:10.1126/sciadv.aau5096.

22. T. Liang, Q. Gibson, M. N. Ali, M. Liu, R. J. Cava, N. P. Ong, Ultrahigh mobility and giant magnetoresistance in the Dirac semimetal Cd3As2. *Nature Materials*. **14**, 280–284 (2015).

23. P. Yang, W. Wang, X. Zhang, K. Wang, L. He, W. Liu, Y. Xu, Quantum Oscillations from Nontrivial States in Quasi-Two-Dimensional Dirac Semimetal ZrTe 5 Nanowires. *Scientific Reports*. **9**, 1–7 (2019).

24. W. Wang, X. Zhang, H. Xu, Y. Zhao, W. Zou, L. He, Y. Xu, Evidence for Layered Quantized Transport in Dirac Semimetal ZrTe5. *Scientific Reports*. **8**, 2–6 (2018).

25. F. Tang, Y. Ren, P. Wang, R. Zhong, J. Schneeloch, S. A. Yang, K. Yang, P. A. Lee, G. Gu, Z. Qiao, L. Zhang, T. Hall, Three-dimensional quantum Hall effect and metal–insulator transition in ZrTe5. *Nature*, doi:10.1038/s41586-019-1180-9.

26. H. Chi, C. Zhang, G. Gu, D. E. Kharzeev, X. Dai, Q. Li, Lifshitz transition mediated electronic transport anomaly in bulk ZrTe5 (available at https://arxiv.org/ftp/arxiv/papers/1701/1701.04737.pdf).

27. P. Shahi, D. J. Singh, J. P. Sun, L. X. Zhao, G. F. Chen, J. Yan, Bipolar Conduction is the Origin of the Electronic Transition in Pentatellurides : Metallic vs . Semiconducting Behavior.

28. W. G. Moffatt, *The Handbook of Binary Phase Diagrams* (Genium Publishing Corporation, 1976).

29. P. C. Canfield, New materials physics. *Reports on Progress in Physics*. **83** (2020), doi:10.1088/1361-6633/ab514b.

30. A.-P. Tsai, C. Cui, *Handbook of Crystal Growth* (ed. 2nd, 2015).

31. Q. Li, D. E. Kharzeev, C. Zhang, Y. Huang, I. Pletikosić, A. v. Fedorov, R. D. Zhong, J. A. Schneeloch, G. D. Gu, T. Valla, Chiral magnetic effect in ZrTe 5. *Nature Physics*. **12**, 550–554 (2016).

32. P. Schmidt, M. Binnewies, R. Glaum, M. Schmidt, *Chemical vapor transport reactions* (De Gruyter, 2012).

33. Y. Y. Lv, F. Zhang, B. bin Zhang, B. Pang, S. H. Yao, Y. B. Chen, L. Ye, J. Zhou, S. T. Zhang, Y. F. Chen, Microstructure, growth mechanism and anisotropic resistivity of quasi-one-dimensional ZrTe5 crystal. *Journal of Crystal Growth*. **457**, 250–254 (2017).

34. C. W. Hicks, M. E. Barber, S. D. Edkins, D. O. Brodsky, A. P. Mackenzie, Piezoelectric-based apparatus for strain tuning (2014) (available at https://arxiv.org/pdf/1403.4368.pdf).

35. C. W. Hicks, M. E. Barber, S. D. Edkins, D. O. Brodsky, A. P. Mackenzie, Piezoelectric-based apparatus for strain tuning. *Review of Scientific Instruments*. **85** (2014), doi:10.1063/1.4881611.

36. J. Mutch, W. C. Chen, P. Went, T. Qian, I. Z. Wilson, A. Andreev, C. C. Chen, J. H. Chu, Evidence for a strain-tuned topological phase transition in ZrTe5. *Science Advances*. **5** (2019), doi:10.1126/sciadv.aav9771.

37. P. Zhang, R. Noguchi, K. Kuroda, C. Lin, K. Kawaguchi, K. Yaji, A. Harasawa, M. Lippmaa, S. Nie, H. Weng, V. Kandyba, A. Giampietri, A. Barinov, Q. Li, G. D. Gu, S. Shin, T. Kondo, Observation and control of the weak topological insulator state in ZrTe5. *Nature Communications*. **12**, 6–12 (2021).

38. S. Murakami, S. I. Kuga, Universal phase diagrams for the quantum spin Hall systems. *Physical Review B - Condensed Matter and Materials Physics*. **78**, 1–10 (2008).

39. S. Murakami, Phase transition between the quantum spin Hall and insulator phases in 3D: Emergence of a topological gapless phase. *New Journal of Physics*. **9** (2007), doi:10.1088/1367-2630/9/9/356.

40. X. L. Qi, S. C. Zhang, Topological insulators and superconductors. *Reviews of Modern Physics*. **83** (2011), doi:10.1103/RevModPhys.83.1057.

41. B. Yan, C. Felser, Topological Materials : Weyl Semimetals, 1–19 (2017).

42. N. P. Armitage, E. J. Mele, A. Vishwanath, Weyl and Dirac semimetals in three-dimensional solids. *Reviews of Modern Physics*. **90** (2018), doi:10.1103/RevModPhys.90.015001.

43. T. O. Wehling, A. M. Black-Schaffer, A. v. Balatsky, Dirac materials. *Advances in Physics*. **63**, 1–76 (2014).

44. O. Vafek, A. Vishwanath, Dirac fermions in solids: From high-Tc cuprates and graphene to Topological insulators and Weyl semimetals. *Annual Review of Condensed Matter Physics*. **5**, 83–112 (2014).

45. S. Y. Xu, Y. Xia, L. A. Wray, S. Jia, F. Meier, J. H. Dil, J. Osterwalder, B. Slomski, A. Bansil, H. Lin, R. J. Cava, M. Z. Hasan, Topological phase transition and texture inversion in a tunable topological insulator. *Science*. **332**, 560–564 (2011).

46. P. Dziawa, B. J. Kowalski, K. Dybko, R. Buczko, A. Szczerbakow, M. Szot, E. Łusakowska, T. Balasubramanian, B. M. Wojek, M. H. Berntsen, O. Tjernberg, T. Story, Topological crystalline insulator states in Pb1-xSn xSe. *Nature Materials*. **11**, 1023–1027 (2012).

47. Z. Fan, Q. F. Liang, Y. B. Chen, S. H. Yao, J. Zhou, Transition between strong and weak topological insulator in ZrTe 5 and HfTe 5. *Scientific Reports*. **7**, 1–7 (2017).

48. G. Manzoni, L. Gragnaniello, G. Autès, T. Kuhn, A. Sterzi, F. Cilento, M. Zacchigna, V. Enenkel, I. Vobornik, L. Barba, F. Bisti, P. Bugnon, A. Magrez, V. N. Strocov, H. Berger, O. v. Yazyev, M. Fonin, F. Parmigiani, A. Crepaldi, Evidence for a Strong Topological Insulator Phase in ZrTe5. *Physical Review Letters*. **117**, 1–5 (2016).

49. R. Y. Chen, S. J. Zhang, J. A. Schneeloch, C. Zhang, Q. Li, G. D. Gu, N. L. Wang, Optical spectroscopy study of the three-dimensional Dirac semimetal ZrTe5. *Physical Review B - Condensed Matter and Materials Physics*. **92** (2015), doi:10.1103/PhysRevB.92.075107.

50. Y. Liu, X. Yuan, C. Zhang, Z. Jin, A. Narayan, C. Luo, Z. Chen, L. Yang, J. Zou, X. Wu, S. Sanvito, Z. Xia, L. Li, Z. Wang, F. Xiu, DO NOT CITE Zeeman splitting and dynamical mass generation in Dirac semimetal ZrTe5. *Nature Communications*. **7**, 1–9 (2016).

51. N. L. Nair, P. T. Dumitrescu, S. Channa, S. M. Griffin, J. B. Neaton, A. C. Potter, J. G. Analytis, Thermodynamic signatures for the existence of Dirac electrons in ZrTe5. *arXiv* (2017), doi:10.1103/PhysRevB.97.041111.

52. X. B. Li, W. K. Huang, Y. Y. Lv, K. W. Zhang, C. L. Yang, B. bin Zhang, Y. B. Chen, S. H. Yao, J. Zhou, M. H. Lu, L. Sheng, S. C. Li, J. F. Jia, Q. K. Xue, Y. F. Chen, D. Y. Xing, Experimental Observation of Topological Edge States at the Surface Step Edge of the Topological Insulator ZrTe5. *Physical Review Letters*. **116**, 1–5 (2016).

53. Z. G. Chen, R. Y. Chen, R. D. Zhong, J. Schneeloch, C. Zhang, Y. Huang, F. Qu, R. Yu, Q. Li, G. D. Gu, N. L. Wang, Spectroscopic evidence for bulk-band inversion and three-dimensional massive Dirac fermions in ZrTe5. *Proceedings of the National Academy of Sciences of the United States of America*. **114**, 816–821 (2017).

54. Y. Jiang, Z. L. Dun, H. D. Zhou, Z. Lu, K. W. Chen, S. Moon, T. Besara, T. M. Siegrist, R. E. Baumbach, D. Smirnov, Z. Jiang, Landau-level spectroscopy of massive Dirac fermions in single-crystalline ZrTe5 thin flakes. *Physical Review B*. **96** (2017), doi:10.1103/PhysRevB.96.041101.

55. H. Xiong, J. A. Sobota, S. L. Yang, H. Soifer, A. Gauthier, M. H. Lu, Y. Y. Lv, S. H. Yao, D. Lu, M. Hashimoto, P. S. Kirchmann, Y. F. Chen, Z. X. Shen, Three-dimensional nature

of the band structure of ZrTe5 measured by high-momentum-resolution photoemission spectroscopy. *Physical Review B*. **95** (2017), doi:10.1103/PhysRevB.95.195119.

56. P. Shahi, D. J. Singh, J. P. Sun, L. X. Zhao, G. F. Chen, Y. Y. Lv, J. Li, J. Q. Yan, D. G. Mandrus, J. G. Cheng, Bipolar Conduction as the Possible Origin of the Electronic Transition in Pentatellurides: Metallic vs Semiconducting Behavior. *Physical Review X*. **8**, 1–13 (2018).

57. T. Liang, J. Lin, Q. Gibson, S. Kushwaha, M. Liu, W. Wang, H. Xiong, J. A. Sobota, M. Hashimoto, P. S. Kirchmann, Z. X. Shen, R. J. Cava, N. P. Ong, Anomalous Hall effect in ZrTe5. *Nature Physics*. **14**, 451–455 (2018).

58. C. W. Hicks, D. O. Brodsky, E. a Yelland, A. S. Gibbs, J. a N. Bruin, M. E. Barber, S. D. Edkins, K. Nishimura, S. Yonezawa, Y. Maeno, A. P. Mackenzie, Strong Increase of TC of SrRuO4 Under Both Tensile and Compressive Strain. *Science (New York, N.Y.)*. **344**, 283–285 (2014).

59. R. Y. Chen, Z. G. Chen, X. Y. Song, J. A. Schneeloch, G. D. Gu, F. Wang, N. L. Wang, Magnetoinfrared Spectroscopy of Landau Levels and Zeeman Splitting of Three-Dimensional Massless Dirac Fermions in ZrTe5. *Physical Review Letters*. **115** (2015), doi:10.1103/PhysRevLett.115.176404.

60. C. Herring, E. Vogt, Transport and deformation-potential theory for many-valley semiconductors with anisotropic scattering. *Physical Review*. **101**, 944–961 (1956).

61. D. T. Son, B. Z. Spivak, Chiral anomaly and classical negative magnetoresistance of Weyl metals. **104412**, 1–4 (2013).

62. J. Xiong, S. K. Kushwaha, T. Liang, J. W. Krizan, M. Hirschberger, W. Wang, R. J. Cava, N. P. Ong, Evidence for the chiral anomaly in the Dirac semimetal Na3Bi. *Science*. **350**, 413–416 (2015).

63. A. v. Andreev, B. Z. Spivak, Longitudinal Negative Magnetoresistance and Magnetotransport Phenomena in Conventional and Topological Conductors. *Physical Review Letters*. **120** (2018), doi:10.1103/PhysRevLett.120.026601.

64. Y. Chen, H. Z. Lu, X. C. Xie, Forbidden Backscattering and Resistance Dip in the Quantum Limit as a Signature for Topological Insulators. *Physical Review Letters*. **121**, 36602 (2018).

65. D. Xiao, M.-C. Chang, Q. Niu, Berry Phase Effects on Electronic Properties (2009) (available at https://arxiv.org/pdf/0907.2021.pdf).

66. R. Karplus, J. M. Luttinger, Hall effect in ferromagnetics. *Physical Review*. **95**, 1154–1160 (1954).

67. Y. Yao, L. Kleinman, A. H. MacDonald, J. Sinova, T. Jungwirth, D. sheng Wang, E. Wang, Q. Niu, First Principles Calculation of Anomalous Hall Conductivity in Ferromagnetic bcc Fe. *Physical Review Letters*. **92**, 4 (2004).

68. X. Wang, J. R. Yates, I. Souza, D. Vanderbilt, Ab initio calculation of the anomalous Hall conductivity by Wannier interpolation. *Physical Review B - Condensed Matter and Materials Physics*. **74**, 1–15 (2006).

69. N. Nagaosa, J. Sinova, S. Onoda, A. H. MacDonald, N. P. Ong, Anomalous Hall effect. **82**, 1539–1592 (2010).

70. X. Wang, D. Vanderbilt, J. R. Yates, I. Souza, Fermi-surface calculation of the anomalous Hall conductivity. *Physical Review B - Condensed Matter and Materials Physics*. **76**, 1–11 (2007).

71. D. R. Hofstadter, Energy levels and wave functions of Bloch electrons in rational and irrational magnetic fields. *Physical Review B*. **14**, 2239–2249 (1976).

72. J. Mutch, X. Ma, C. Wang, P. Malinowski, J. Ayres-Sims, Q. Jiang, Z. Liu, D. Xiao, M. Yankowitz, J.-H. Chu, Abrupt switching of the anomalous Hall effect by field-rotation in nonmagnetic $ZrTe_5$. *arXiv:2101.02681* (2021).

73. Y. Liu, X. Yuan, C. Zhang, Z. Jin, A. Narayan, C. Luo, Z. Chen, L. Yang, J. Zou, X. Wu, S. Sanvito, Z. Xia, L. Li, Z. Wang, F. Xiu, Zeeman splitting and dynamical mass generation in Dirac semimetal ZrTe5. *Nature Communications*. **7**, 1–9 (2016).

74. Q. Li, D. E. Kharzeev, C. Zhang, Y. Huang, I. Pletikosić, A. v Fedorov, R. D. Zhong, J. A. Schneeloch, G. D. Gu, T. Valla, Chiral magnetic effect in ZrTe5, doi:10.1038/NPHYS3648.

75. B. Xu, L. X. Zhao, P. Marsik, E. Sheveleva, F. Lyzwa, Y. M. Dai, G. F. Chen, X. G. Qiu, C. Bernhard, Temperature-Driven Topological Phase Transition and Intermediate Dirac Semimetal Phase in ZrTe5. *Physical Review Letters*. **121**, 1–6 (2018).

76. H. Wang, H. Liu, Y. Li, Y. Liu, J. Wang, J. Liu, J. Y. Dai, Y. Wang, L. Li, J. Yan, D. Mandrus, X. C. Xie, J. Wang, Discovery of log-periodic oscillations in ultraquantum topological materials. *Science Advances*. **4** (2018), doi:10.1126/sciadv.aau5096.

77. Z. Sun, Z. Cao, J. Cui, C. Zhu, D. Ma, H. Wang, W. Zhuo, Z. Cheng, Z. Wang, X. Wan, X. Chen, Large Zeeman splitting induced anomalous Hall effect in ZrTe 5. *npj Quantum Materials*, 1–7 (2020).

78. N. P. Armitage, Weyl and Dirac semimetals in three-dimensional solids. *Reviews of Modern Physics*. **90**, 15001 (2018).

79. Y. Choi, J. W. Villanova, K. Park, Zeeman-splitting-induced Topological Nodal Structure and Anomalous Hall Conductivity in ZrTe$_5$. **035105**, 1–14 (2019).

80. A. B. Pippard, *Magnetoresistance in metals* (Cambridge University Press, 1989).

81. X. Huang, L. Zhao, Y. Long, P. Wang, D. Chen, Z. Yang, H. Liang, M. Xue, H. Weng, Z. Fang, X. Dai, G. Chen, Observation of the Chiral-Anomaly-Induced Negative Magnetoresistance in 3D Weyl Semimetal TaAs. **031023**, 1–9 (2015).

82. J. Niu, J. Wang, Z. He, C. Zhang, X. Li, T. Cai, X. Ma, S. Jia, D. Yu, X. Wu, Electrical transport in nanothick ZrTe5 sheets: From three to two dimensions. *Physical Review B*. **95**, 1–7 (2017).

83. W. Kang, Lebed's Magic Angle Effects in (TMTSF) 2PF6 '. **69**, 2827–2830 (1992).

84. M. J. Naughton, O. H. Chung, M. Chaparala, X. Bu, P. Coppens, Commensurate Fine Structure in Angular-Dependent Studies of (TMTSF) 2Cl04. **67**, 3712–3715 (1991).

85. T. Osada, A. Kawasumi, S. Kagoshima, N. Miura, G. Saito, Commensurability effect of magnetoresistance anisotropy in the quasi-one-dimensional conductor tetramethyltetraselenafulvalenium perchlorate, (TMTSF)2ClO4. *Physical Review Letters*. **66**, 1525–1528 (1991).

86. M. v Kartsovnik, High Magnetic Fields : A Tool for Studying Electronic Properties of Layered Organic Metals (2004), doi:10.1021/cr0306891.

87. a. G. Lebed', Anisotropy of an instability for a spin density wave induced bye a magnetic field in a Q1D conductor. *JETP Lett.(Engl. Transl.);(United States)*. **43** (1985), p. 174.

88. T. Osada, S. Kagoshima, N. Miura, Resonance effect in magnetotransport anisotropy of quasi-one-dimensional conductors. *Physical Review B*. **46**, 1812–1815 (1992).

89. Chaikin, "Hot Spots", Magic Angles, and Magnetoresistance in Quasi-1D Metals. *Physical Review Letters*. **69**, 2831–2835 (1992).

90. M. Aidelsburger, M. Atala, M. Lohse, J. T. Barreiro, B. Paredes, I. Bloch, Realization of the hofstadter hamiltonian with ultracold atoms in optical lattices. *Physical Review Letters*. **111**, 1–5 (2013).

91. X. Ni, K. Chen, M. Weiner, D. J. Apigo, C. Prodan, A. Alù, E. Prodan, A. B. Khanikaev, Observation of Hofstadter butterfly and topological edge states in reconfigurable quasi-periodic acoustic crystals. *Communications Physics*. **2** (2019), doi:10.1038/s42005-019-0151-7.

92. R. K. Kumar, X. Chen, G. H. Auton, A. Mishchenko, D. A. Bandurin, S. v Morozov, Y. Cao, E. Khestanova, M. ben Shalom, A. v Kretinin, K. S. Novoselov, L. Eaves, I. v Grigorieva, L. A. Ponomarenko, High-temperature quantum oscillations caused by recurring Bloch states in graphene superlattices. **184**, 181–184 (2017).

93. M. Koshino, H. Aoki, K. Kuroki, S. Kagoshima, T. Osada, Hofstadter butterfly and integer quantum Hall effect in three dimensions. *Physical Review Letters*. **86**, 1062–1065 (2001).

94. S. Blundell, J. Singleton, Semiclassical description of angle-dependent magnetoresistance oscillations in quasi-one-dimensional metals. *Physical Review B - Condensed Matter and Materials Physics*. **53**, 5609–5619 (1996).

95. K. Kobayashi, H. Satsukawa, J. Yamada, T. Terashima, S. Uji, Observation of orbital resonance hall effect in (TMTSF)2ClO4. *Physical Review Letters*. **112**, 1–5 (2014).

96. E. Brown, Bloch Electrons in a Uniforrm Magnetic Field. **763** (1964).

97. S. Wu, A. G. Lebed, Unification theory of angular magnetoresistance oscillations in quasi-one-dimensional conductors. *Physical Review B - Condensed Matter and Materials Physics*. **82**, 1–6 (2010).

98. B. K. Cooper, V. M. Yakovenko, Interlayer aharonov-bohm interference in tilted magnetic fields in quasi-one-dimensional organic conductors. *Physical Review Letters*. **96**, 2–5 (2006).

99. J. Wang, J. Niu, B. Yan, X. Li, R. Bi, Y. Yao, D. Yu, X. Wu, Vanishing quantum oscillations in Dirac semimetal ZrTe $_5$. *Proceedings of the National Academy of Sciences*. **115**, 201804958 (2018).

100. G. Zheng, J. Lu, X. Zhu, W. Ning, Y. Han, H. Zhang, J. Zhang, C. Xi, J. Yang, H. Du, K. Yang, Y. Zhang, M. Tian, Transport evidence for the three-dimensional Dirac semimetal phase in ZrT e5. *Physical Review B*. **93**, 1–7 (2016).

101. M. Koshino, H. Aoki, T. Osada, K. Kuroki, S. Kagoshima, Phase diagram for the Hofstadter butterfly and integer quantum Hall effect in three dimensions. *Physical Review B - Condensed Matter and Materials Physics*. **65**, 1–9 (2002).

102. A. A. Abrikosov, Quantum linear magnetoresistance; solution of an old mystery. *Journal of Physics A: Mathematical and General*. **36**, 9119–9131 (2003).

103. K. Behnia, K. Behnia, *Fundamentals of Thermoelectricity* (Oxford University Press, 2019), vol. 0.

104. B. Skinner, L. Fu, Large, nonsaturating thermopower in a quantizing magnetic field. *arXiv*, 1–7 (2017).

105. W. Zhang, P. Wang, B. Skinner, R. Bi, V. Kozii, C. W. Cho, R. Zhong, J. Schneeloch, D. Yu, G. Gu, L. Fu, X. Wu, L. Zhang, Observation of a thermoelectric Hall plateau in the extreme quantum limit. *Nature Communications*. **11**, 8–12 (2020).

106. T. Konoike, M. Sato, K. Uchida, T. Osada, Anomalous thermoelectric transport and giant nernst effect in multilayered massless dirac fermion system. *Journal of the Physical Society of Japan*. **82**, 1–4 (2013).

107. K. G. Rana, F. K. Dejene, N. Kumar, C. R. Rajamathi, K. Sklarek, C. Felser, S. S. P. Parkin, Thermopower and Unconventional Nernst Effect in the Predicted Type-II Weyl Semimetal WTe2. *Nano Letters*. **18**, 6591–6596 (2018).

108. R. Daou, J. Chang, D. Leboeuf, O. Cyr-Choinière, F. Laliberté, N. Doiron-Leyraud, B. J. Ramshaw, R. Liang, D. A. Bonn, W. N. Hardy, L. Taillefer, Broken rotational symmetry in the pseudogap phase of a high-Tc superconductor. *Nature*. **463**, 519–522 (2010).

109. S. Jiang, H. S. Jeevan, J. Dong, P. Gegenwart, Thermopower as a sensitive probe of electronic nematicity in iron pnictides. *Physical Review Letters*. **110**, 1–5 (2013).

110. X. Shi, L. Chen, C. Uher, Recent advances in high-performance bulk thermoelectric materials. *International Materials Reviews*. **61**, 379–415 (2016).

111. C. Gayner, K. K. Kar, Recent advances in thermoelectric materials. *Progress in Materials Science*. **83**, 330–382 (2016).

112. G. Tan, L. D. Zhao, M. G. Kanatzidis, Rationally Designing High-Performance Bulk Thermoelectric Materials. *Chemical Reviews*. **116**, 12123–12149 (2016).

113. A. Stern, M. Dzero, V. M. Galitski, Z. Fisk, J. Xia, Surface-dominated conduction up to 240 K in the Kondo insulator SmB 6 under strain. *Nature Materials*. **16**, 708–711 (2017).

114. S. E. E. L. Page, Divergent Nematic Susceptibility in an Iron Arsenide Superconductor. **337** (2012).

115. J. Park, H. Sakai, O. Erten, A. P. Mackenzie, C. W. Hicks, Effect of applied orthorhombic lattice distortion on the antiferromagnetic phase of CeAuSb2. *Physical Review B*. **97** (2018), doi:10.1103/PhysRevB.97.024411.

116. M. Matusiak, M. Babij, T. Wolf, Anisotropy of the Seebeck and Nernst coefficients in parent compounds of the iron-based superconductors. *Physical Review B*. **97**, 1–6 (2018).

117. E. Mun, S. L. Bud'ko, M. S. Torikachvili, Experimental setup for the measurement of the thermoelectric power in zero and applied magnetic field. *Measurement Science and Technology* (2010), doi:10.1088/0957-0233/21/5/055104.

118. M. Matusiak, Z. Bukowski, J. Karpinski, Doping dependence of the Nernst effect in Eu (Fe 1 − x Co x) 2 As 2 : Departure from Dirac-fermion physics. **224505**, 1–5 (2011).

119. T. Nomura, Y. Inoue, S. Matsuishi, M. Hirano, J. E. Kim, K. Kato, M. Takata, H. Hosono, Comparison of crystal structures and the effects of Co substitution in a new member of the Fe-1111 superconductor family AeFeAsF (Ae = Ca and Sr): A possible candidate for a higher-Tc superconductor. *Superconductor Science and Technology*. **22** (2009), doi:10.1088/0953-2048/22/5/055016.

120. M. S. Ikeda, T. Worasaran, J. C. Palmstrom, J. A. W. Straquadine, P. Walmsley, I. R. Fisher, Symmetric and antisymmetric strain as continuous tuning parameters for electronic nematic order. *Physical Review B*. **98** (2018), doi:10.1103/PhysRevB.98.245133.

121. M. He, L. Wang, F. Ahn, F. Hardy, T. Wolf, P. Adelmann, J. Schmalian, I. Eremin, C. Meingast, Dichotomy between in-plane magnetic susceptibility and resistivity anisotropies in extremely strained BaFe2As2. *Nature Communications*. **8**, 4–9 (2017).

122. F. Caglieris, C. Wuttke, X. Hong, S. Sykora, R. Kappenberger, S. Aswartham, S. Wurmehl, B. Büchner, C. Hess, Strain-derivative of thermoelectric properties: a sensitive

probe for nematicity. (arXiv:1905.11660v2 [cond-mat.supr-con] UPDATED). *arXiv Superconductivity*, 1–19.

123. C. Fujii, S. Simayi, K. Sakano, C. Sasaki, M. Nakamura, Y. Nakanishi, K. Kihou, M. Nakajima, C. H. Lee, A. Iyo, H. Eisaki, S. I. Uchida, M. Yoshizawa, Diverse fluctuations and anisotropic Grüneisen parameter behavior in iron-based superconductor Ba(Fe1-xCox)2As2and their correlation with superconductivity. *arXiv*. **074710**, 1–8 (2018).

124. Y. Tang, B. Cui, C. Zhou, M. Grayson, p × n-Type Transverse Thermoelectrics: A Novel Type of Thermal Management Material. *Journal of Electronic Materials*. **44**, 2095–2104 (2015).

125. C. Zhou, S. Birner, Y. Tang, K. Heinselman, M. Grayson, Driving perpendicular heat flow: (p×n)-type transverse thermoelectrics for microscale and cryogenic peltier cooling. *Physical Review Letters*. **110**, 1–5 (2013).

126. C. Zhou, Y. Tang, M. Grayson, p × n-type transverse thermoelectrics: an alternative Peltier refrigerator with cryogenic promise. *Laser Refrigeration of Solids VII*. **9000**, 900006 (2014).

127. S. Sarikurt, T. Kocabaş, C. Sevik, High-Throughput computational screening of 2D materials for thermoelectrics. *Journal of Materials Chemistry A*. **8**, 19674–19683 (2020).

128. Y. Wang, K. G. Koster, A. M. Ochs, M. R. Scudder, J. P. Heremans, W. Windl, J. E. Goldberger, The Chemical Design Principles for Axis-Dependent Conduction Polarity. *Journal of the American Chemical Society*. **142**, 2812–2822 (2020).

129. J. J. Gu, M. W. Oh, H. Inui, D. Zhang, Anisotropy of mobility ratio between electron and hole along different orientations in ReGe xSi 1.75-x thermoelectric single crystals. *Physical Review B - Condensed Matter and Materials Physics*. **71**, 4–7 (2005).

130. D. Y. Chung, S. D. Mahanti, W. Chen, C. Uher, M. G. Kanatzidis, Anisotropy in thermoelectric properties of CsBi4Te6. *Materials Research Society Symposium - Proceedings*. **793**, 141–148 (2003).

131. B. He, Y. Wang, M. Q. Arguilla, N. D. Cultrara, M. R. Scudder, J. E. Goldberger, W. Windl, J. P. Heremans, The Fermi surface geometrical origin of axis-dependent conduction polarity in layered materials. *Nature Materials*. **18**, 568–572 (2019).

132. J. Dolinšek, M. Komelj, P. Jeglič, S. Vrtnik, D. Stanić, P. Popčević, J. Ivkov, A. Smontara, Z. Jagličić, P. Gille, Y. Grin, Anisotropic magnetic and transport properties of orthorhombic Al13 Co4. *Physical Review B - Condensed Matter and Materials Physics*. **79**, 1–12 (2009).

133. Y. Kawasugi, K. Seki, Y. Edagawa, Y. Sato, J. Pu, T. Takenobu, S. Yunoki, H. M. Yamamoto, R. Kato, Simultaneous enhancement of conductivity and Seebeck coefficient in an organic Mott transistor. *Applied Physics Letters*. **109**, 4–8 (2016).

134. R. C. Yu, J. M. Williams, H. H. Wang, J. E. Thompson, A. M. Kini, K. D. Carlson, J. Ren, M. H. Whangbo, P. M. Chaikin, Anisotropic thermopower of the organic superconductor κ-(BEDT-TTF) 2Cu[N(CN)2]Br. *Physical Review B*. **44**, 6932–6936 (1991).

135. K. Koepernik, D. Kasinathan, D. v. Efremov, S. Khim, S. Borisenko, B. Büchner, J. van den Brink, TaIrTe4: A ternary type-II Weyl semimetal. *Physical Review B*. **93**, 1–5 (2016).

136. W. Zhou, B. Li, C. Q. Xu, M. R. van Delft, Y. G. Chen, X. C. Fan, B. Qian, N. E. Hussey, X. Xu, Nonsaturating Magnetoresistance and Nontrivial Band Topology of Type-II Weyl Semimetal NbIrTe4. *Advanced Electronic Materials*. **5**, 1–8 (2019).

137. R. Schönemann, Y. C. Chiu, W. Zheng, V. L. Quito, S. Sur, G. T. McCandless, J. Y. Chan, L. Balicas, Bulk Fermi surface of the Weyl type-II semimetallic candidate NbIrTe4. *Physical Review B*. **99**, 1–7 (2019).

138. S. Khim, K. Koepernik, D. v. Efremov, J. Klotz, T. Förster, J. Wosnitza, M. I. Sturza, S. Wurmehl, C. Hess, J. van den Brink, B. Büchner, Magnetotransport and de Haas-van Alphen measurements in the type-II Weyl semimetal TaIrTe4. *Physical Review B*. **94**, 1–8 (2016).

139. A. Sakai, S. Minami, T. Koretsune, T. Chen, T. Higo, Y. Wang, T. Nomoto, M. Hirayama, S. Miwa, D. Nishio-Hamane, F. Ishii, R. Arita, S. Nakatsuji, Iron-based binary ferromagnets for transverse thermoelectric conversion. *Nature*. **581** (2020), doi:10.1038/s41586-020-2230-z.

140. Y. Liu, Q. Gu, Y. Peng, S. Qi, N. Zhang, Y. Zhang, X. Ma, R. Zhu, L. Tong, J. Feng, Z. Liu, J. H. Chen, Raman Signatures of Broken Inversion Symmetry and In-Plane Anisotropy in Type-II Weyl Semimetal Candidate TaIrTe4. *Advanced Materials*. **30**, 1–9 (2018).

141. H. Shi, D. Parker, M. H. Du, D. J. Singh, Connecting thermoelectric performance and topological-insulator behavior: Bi2Te3 and Bi2Te2Se from first principles. *Physical Review Applied*. **3**, 1–10 (2015).

VITA

Josh Mutch was born in San Diego, California. He earned his bachelor’s degree in physics from Oregon State University, graduating summa cum laude in 2015. In the fall of 2015, he joined the University of Washington Department of Physics, and in 2016 joined Dr. Jiun-Haw Chu’s Quantum Materials Laboratory.